DIPLOMARBEIT

Grid-Based Terahertz Metamaterials

ausgeführt am
Institut für Photonik
der Technischen Universität Wien

unter der Anleitung von
Univ.Ass. Dipl.-Ing. Dr.techn. Juraj Darmo
und
Univ.Prof. Mag.rer.nat. Dr.rer.nat. Karl Unterrainer

durch
Jakob Kristoferitsch, Bakk. rer. soc. oec.

Wien, im März 2012

We extend our heartfelt thanks to DI Veronika Doblhoff-Dier, who compensated for our utter ignorance of the rules that concern the placement of punctuation marks in the English language. She also contributed many valuable stylistic remarks. Without her, this thesis would lack almost 200 commas.

We also wish to thank Dipl.-Phys. Daniel Dietze. During the three months that Dr. Darmo was visiting Japan, he took over his duties. He also contributed valuable FDTD simulation results.

We gratefully acknowledge the funding by the Austrian taxpayer.

Dedicated to my parents, for their enduring support.

Abstract

Metamaterials allow complete control over the propagation of electromagnetic waves. They consist of resonant circuits that are smaller than the wavelength of the respective radiation.

In order to describe the transmission of a metamaterial composed of wires on a grid, we apply a resonating dipole model [Petschulat et al., 2010], which was introduced in the optical range, to the terahertz range. We use a terahertz time-domain spectroscopy setup to experimentally verify that the model is applicable in the frequency range between 0.1 THz and 2.5 THz. We fit the model to the measured data by using a combination of automatic routines and manual fitting. The gold on gallium arsenide samples were manufactured using e-beam evaporation and standard semiconductor lithography techniques.

We deduce the scaling behavior of the model's parameters by manufacturing and measuring differently scaled structures. This is a first step towards a tool that is able to predict the transmission spectrum of a structure, given only its shape and physical dimensions.

The perpendicular coupling between the dipoles is described by a coupling constant σ. Experimentally, we demonstrate that the coupling is primarily conductive and that capacitive coupling is much weaker. To allow for coupling along an axis, we introduce the longitudinal coupling constant τ and derive its value.

The good results from our first set of samples encourage us to apply the model to more complex structures. We devise an algorithm that allows us to calculate the response of arbitrary grid-based structures. We demonstrate this algorithm on a rectangular and a hexagonal grid.

To produce new kinds of structures, we integrate the algorithm on a rectangular grid into the fitness function of a genetic algorithm. We present a result that was produced by this method and compare its measured spectrum to our simulations.

From the results of our measurements, we conclude that the model is very well suited to the description of small structures, while its potential to predict the behavior of larger, hence more complex, structures is limited. Given the model's simplicity, it provides remarkable results.

Kurzfassung

Metamaterialien erlauben es, die Ausbreitung von elektromagnetischen Wellen beliebig zu steuern. Sie bestehen aus Schwingkreisen, welche kleiner als die Wellenlänge des verwendeten Lichtes sind.

Das in [Petschulat et al., 2010] vorgestellte Model beschreibt das Transmissionsspektrum eines aus dünnen Stäben aufgebauten Metameterials bei optischen Frequenzen mithilfe von schwingenden Dipolen. Durch Messungen mit einem THz-TDS Aufbau beweisen wir experimentell, dass dieses Modell auch im Bereich zwischen 0.1 THz und 2.5 THz anwendbar ist. Wir verwenden eine Kombination aus automatischen und manuellen Verfahren um das Modell an die gemessenen Daten anzupassen. Die Proben bestehen aus Gold, welches in einem Elektronenstrahlverdampfer auf Gallium Arsenid aufgebracht wurde. Zur Strukturierung wurde ein übliches lithographisches Verfahren benutzt.

Weiters stellen wir unterschiedlich große Strukturen her und untersuchen die Abhängigkeit der Parameter des Modelles von den physikalischen Längen. Dies ist ein erster Schritt zu einer Theorie, die es, ausgehend von Form und Größe einer Struktur, erlaubt ihr Transmissionsverhalten vorherzusagen.

Im Modell wird die Kopplung zwischen zwei Dipolen durch die Kopplungskonstante σ beschrieben. Anhand von modifizierten Strukturen untersuchen wir ihr Verhalten und zeigen, dass diese Kopplung vorwiegend auf elektrischer Leitung basiert. Die kapazitive Kopplung ist viel schwächer und spielt daher nur eine untergeordnete Rolle.

Aufgrund der guten Ergebnisse, die das Modell bei einfachen Strukturen erzielt, haben wir es auf kompliziertere Strukturen verallgemeinert. Wir zeigen eine Methode die es erlaubt das Transmissionsverhalten einer beliebigen rechteckigen oder hexagonalen Struktur zu simulieren.

Um neue Arten von Strukturen herzustellen, haben wir das Modell mit einem genetischen Algorithmus kombiniert. Wir zeigen ein Ergebnis dieses Optimierungsverfahrens und vergleichen das gemessene Spektrum mit den Vorhersagen unseres Modelles.

Wie durch unsere Messungen belegt wird, ist das Model dazu geeignet das Verhalten einfacher Strukturen zu beschreiben. Je größer die Strukturen sind und je komplizierter ihr Aufbau ist, desto mehr zeigen sich Abweichungen, die in der Natur der elektromagnetischen Strahlung begründet sind. Wenn man berücksichtigt, wie weitgehend die Vereinfachungen sind auf denen sich das Modell gründet, liefert es erstaunlich gute Resultate.

Contents

1 Introduction **1**
- 1.1 Motivation . . . 1
- 1.2 Methodology . . . 1
- 1.3 Structure of the Thesis . . . 2
- 1.4 The Terahertz Frequency Range . . . 2
- 1.5 Metamaterials . . . 12
- 1.6 Mathematical Methods . . . 19

2 Analytical Model **25**
- 2.1 Introduction . . . 25
- 2.2 Basic Model . . . 27
- 2.3 Parameter Dependence of Transmission . . . 31
- 2.4 Longitudinal Coupling . . . 34
- 2.5 Transmission of Arbitrary Structures . . . 35
- 2.6 Metamaterial Design Using a Genetic Algorithm . . . 39
- 2.7 Hexagonal Structures . . . 41

3 Measurements **45**
- 3.1 Experimental Setup . . . 45
- 3.2 CLS Measurements . . . 49
- 3.3 Structures Containing Gaps . . . 55
- 3.4 Summary of Results . . . 57
- 3.5 Plots . . . 58
- 3.6 Software . . . 62

4 Conclusion **65**
- 4.1 Strengths and Weaknesses of the Coupled Dipole Model . . . 65
- 4.2 Behavior of Grid Based Metamaterials . . . 66
- 4.3 Further Work . . . 66

Bibliography **67**

A Additional Equations **73**
- A.1 Fourier Transform of Differential Equations . . . 73
- A.2 Electric Permittivity . . . 74

A.3 Tailor Expansion of the Dipole Interaction 75
A.4 Coupling Matrices for Petschulat Shapes 76
A.5 Longitudinally Coupled Dipoles 78
A.6 Permittivity of Basic Hexagonal Shapes 79

B Selected Code Fragments **87**
B.1 Calculating Transmission 87
B.2 Fit Calculation 93

C Further Measurements **99**
C.1 Measured Data 99
C.2 Images 105

Chapter 1

Introduction

1.1 Motivation

This thesis combines two relatively young areas of interest: The terahertz frequency range and metamaterials. Together, they promise exciting new applications in science, imaging and telecommunication.

Both areas saw an increase of academic interest in the 1990s and 2000s, due to various innovations, including the invention of the quantum cascade laser (QCL) [Faist et al., 1994] and the invention [Pendry et al., 1999] and fabrication [Shelby et al., 2001] of negative refractive index metamaterials. Obviously, these innovations would not have been possible without earlier inventions (e.g. superlattices) and advances in manufacturing (e.g. molecular beam epitaxy) as well as computing (e.g. electromagnetic simulations).

Research Goal

Our goal was to understand the behavior of arbitrary grid-based metamaterials in the terahertz range. The work is based on a coupled oscillator model [Petschulat et al., 2010]. We wanted to apply this model to the terahertz frequency range and examine different structures. Furthermore, we wanted to create new types of meta-atoms by using the model inside the fitness function of a genetic algorithm.

1.2 Methodology

Before the the start of this thesis, Juraj Darmo [2010] conducted numerical simulations to verify the model proposed by Petschulat et al.. Since the simulations showed promising results we manufactured various metamaterials. We measured their transmission and compared the results to the predictions of our model, proving experimentally that it is applicable in the terahertz range. By fitting the model's parameters and comparing the analytical equations to

the experimental data, we analyzed how the fundamental parameters scale and demonstrated the differences that arise between model and reality.

1.3 Structure of the Thesis

In the first chapter, we present the background of the basic ideas and technologies which this thesis is built upon. At the beginning of the second chapter, we will present a short review of the model as given in the original paper [Petschulat et al., 2010]. We will then elaborate on the extensions we added to accommodate arbitrary structures on rectangular and hexagonal grids. The focus of chapter three is the measurements we conducted to validate the model. We will present the good consistency we found for simple structures as well as the disagreements we discovered for more complex ones. The last chapter will summarize our findings and give an outlook on future development paths. The appendices contain additional information for the interested reader.

1.4 The Terahertz Frequency Range

Terahertz refers to a range of electromagnetic radiation. It is usually defined to contain frequencies between 100 GHz and 10 THz. There is, however, no official definition or even one that is universally agreed upon: the lower boundary is the gigahertz range; the upper boundary is – depending on the definition – in the far or mid infrared range.

Frequency	$1\,\mathrm{THz} = {}^{1}/_{\mathrm{ps}}$
Wavelength (λ)	$\approx 300\,\mu\mathrm{m}$
Energy ($h\nu$)	$\approx 6.62 \times 10^{-22}\,\mathrm{J} \approx 4.14\,\mathrm{meV}$
Temperature ($E = k_b T \Rightarrow T = {}^{h\nu}/_{k_b}$)	$\approx 48\,\mathrm{K}$

Table 1.1: 1 THz corresponds to approximately ...

The highest named frequency band, defined by the International Telecommunication Union (ITU), is EHF, band 11,[1] which goes up to 300 GHz [ITU, 2008]. Frequencies up to 100 GHz are routinely achieved with HF circuits, e.g. in the ISM[2] band at 60 GHz. An additional band 12, between 300 GHz and 3 THz, is defined in the 2008 edition of the ITU radio regulations, but has no associated symbol. This shows a lack of interest in frequencies above 300 GHz

[1] The ITU bands are numbered according to the frequencies they define. A band with number N extends from $0.3 \times 10^{\mathrm{N}}$ Hz to $3 \times 10^{\mathrm{N}}$ Hz. They were historically referenced by wavelength. Since the speed of light in vacuum is $c \approx 3 \times 10^{8}\,\mathrm{m\,s^{-1}}$ and $\lambda = {}^{c}/_{f}$, band 11 (30 GHz to 300 GHz) corresponds to wavelengths between 10 mm and 1 mm.

[2] Industrial, Scientific, Medical. These bands can be used without applying for a license and devices operating in them must tolerate interference. The most famous ISM band is the one around 2.45 GHz. It is used for wireless LAN according to IEEE 802.11 as well as for many other applications, such as Bluetooth devices and baby phones.

and is mostly due to the fact that water vapor absorbs well in this range, so that such signals cannot be transmitted over long distances in the earth's atmosphere. Consequently, this frequency range was of limited interest to the ITU.

In addition to the limited reach of terahertz radiation in the atmosphere, there was a lack of sources and detectors for this region. This rendered it inaccessible in practice and led to the term *terahertz gap*.

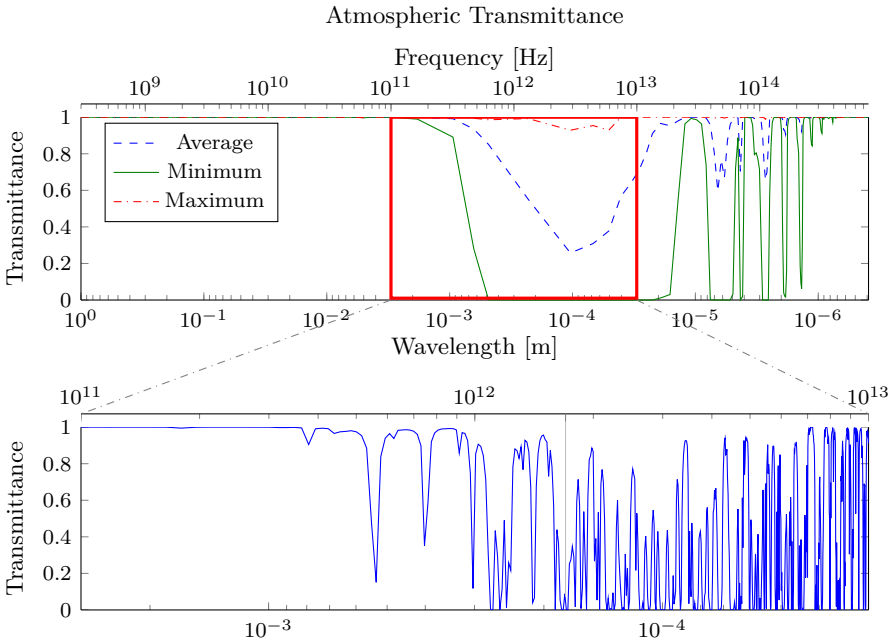

Figure 1.1: Transmittance through 1 m of air at sea level. Transmission in the terahertz range is strongly attenuated, while there is high transmittance in the optical and radio frequency ranges. The plot was generated from HITRAN data.[3]The data points in the overview (above) were bunched. It shows the smoothed average, minimal and maximal values in these bunches. The thin grey line in the detail plot (below) indicates the position of a group of water absorption lines at 1.7 THz, which are sometimes visible in the measured data.

[3]The HITRAN 2008 [Rothman et al., 2009] data was obtained through the calculator at `http://hitran.iao.ru/gasmixture`, using the default settings: Gas mixture: USA model, mean latitude, summer, H=0; Optical path: 1 m; WN_{min} 0 cm^{-1}; WN_{max} 25 500 cm^{-1}; T296 K; P 1.013 25 bar $I_{cut}1 \times 10^{-28}$ cm mol^{-1}; Shape: Voigt; WN_{step}0.01 cm^{-1} Wing, HW: 50; Optical path: 1 m, App.Function (AF): Dirac; App.Resolution 0.01 cm^{-1}; AF wing, AR: 50.

Closing the Terahertz Gap

The first scientists interested in the detection of terahertz radiation were radio astronomers, as a large amount of extraterrestrial photons in this energy range: it is estimated that "98% of the photons emitted since the big bang fall into the submillimeter and far-IR" ([Leisawitz et al., 2000], quoted in [Siegel, 2002]). Consequently, the first detectors were developed to meet their requirements.

In addition to astronomical applications, the terahertz spectral region is interesting for spectroscopy. The energies of terahertz waves correspond to rotational transitions in molecules as well as to phonon excitation energies. The energy of the longitudinal optical phonon in GaAs, for example, is 35 meV [Sze, 1981, p.39 and appendix H], which corresponds to a frequency of ≈ 8.5 THz.

Yun-Shik Lee [Lee, 2008, ch.2.2, p.28] summarizes the different areas of interest:[4]

> Interactions of THz waves with matter involve low-energy excitations corresponding to THz frequencies. Some elementary excitations of cardinal interest include Rydberg transitions in atoms, transitions among impurity states in semiconductors, intraband transitions in semiconductor nanostructures, many-body interactions in strongly correlated electron systems, phonon modes in organic and inorganic crystals, rotation-vibration transitions in molecules, and collective large-amplitude motions in biological molecules.

Starting from the beginnings in astronomy, efforts to close the terahertz gap were undertaken from both sides of it. Electrical engineers tried to generate higher and higher frequencies from their HF sources, while physicists were reaching toward lower energies using their optical sources.

Both sides soon reached fundamental limits. Engineering oscillating circuits for terahertz frequencies is impossible due to the small time constants, which are in the picosecond range. Solid state sources could not offer the low transition energies required for terahertz emission.

Sources in the optical and infrared frequency ranges are usually based on electronic transitions[5], with energies in the eV range. Energies of meV were smaller than those used in optics, and were out of the reach of semiconductors. Band gaps of semiconductors at room temperature are in the range of eV, between 0.17 eV (InSb, 41 THz)[6] and 6.12 eV (AlN, [Li et al., 2003], 1.48 PHz). Silicon, the most widely used semiconductor material, has a band gap of 1.11 eV, gallium arsenide has one of 1.43 eV. These band gaps correspond to frequencies in the IR to UV range.

Even microwave engineering, with a broad body of experience and today's computational tools, is still more or less a black art. The sub-millimeter range, where an even steeper learning curve is still ahead of us, amounts to alchemy.

[4] The original text includes references to primary sources, which are omitted here.

[5] Another important source is black body radiation.

[6] Unless noted otherwise, band gap energies are taken from the table "properties of semiconductor materials", in [Streetman and Banerjee, 2000, p.439]

From photonic and electronic roots, the field of photonics was born. It is an area where optics and electronics struggle to meet.

An effect of the interdisciplinary nature of the field of photonics is the mixture of preferred units. While frequencies are most often used as the unit of choice in electrical engineering, wavelengths are preferred in optics. Few people would say that their 2.45 GHz WLAN uses a wavelength of 12 cm. At the same time almost nobody thinks of a red laser with a wavelength of 750 nm as emitting light at a frequency of 400 THz, or that the wavelength of 1550 nm that is popular in fiber optic telecommunications corresponds to a frequency of 193 THz.

Sources of Terahertz Radiation

Electromagnetic radiation can be generated from two fundamental principles: State transitions and accelerated charges.[7] The different ways to accelerate or excite charge carriers give rise to a wide range of sources for terahertz radiation. They vary in output power (mW to kW, peak powers up to MW [Carr et al., 2002]), spectral width, beam shape, coherence and many other characteristics.

Depending on the method of generation they are based on, the sources can be sub-classed into groups:

- Electronic transition (quantum cascade laser)
- Short laser pulses (photoconductive antenna, crystals, plasmas, optical rectification)
- Acceleration of free electrons (free electron laser, backward wave oscillator)
- Thermal radiation (thermal background, glow bar)

In addition to these primary sources, there are also secondary sources. They consist of a primary beam which is manipulated in such a manner that it creates a secondary terahertz beam. These techniques are based on nonlinear[8] optical effects. Examples are optical rectification or sum- and difference-frequency generation.

An exhaustive description of all the generation methods listed above can be found in [Lee, 2008]. We will, for the sake of brevity, focus on a selection of four sources:

[7] Daniel Dietze reminded me that even electronic state changes can be interpreted as the movement of carriers. In a dipole transition, the center of mass of the wave function shifts. Transitions where the center of mass stays in the same place are forbidden by selection rules, since their dipole moment is zero.

[8] Nonlinear refers to the fact that these effects are proportional to a higher order susceptibility $\chi^{(n)}$. Most effects are second ($n = 2$) or third order ($n = 3$) effects. These effects only occur at large field strengths, since the higher order susceptibilities are much weaker than the linear susceptibility.

- Thermal radiation, which is the dominating source of terahertz radiation at room temperature.
- Photoconductive antennas, which allow for coherent detection and are a building block of many time-domain spectroscopy setups, including the one we used in our experiments.
- Quantum cascade lasers, which are a very promising candidate for a solid state terahertz laser source.
- Free electron lasers, which produce the highest intensities and, hence, are important sources for the examination of nonlinear effects.

Thermal Radiation

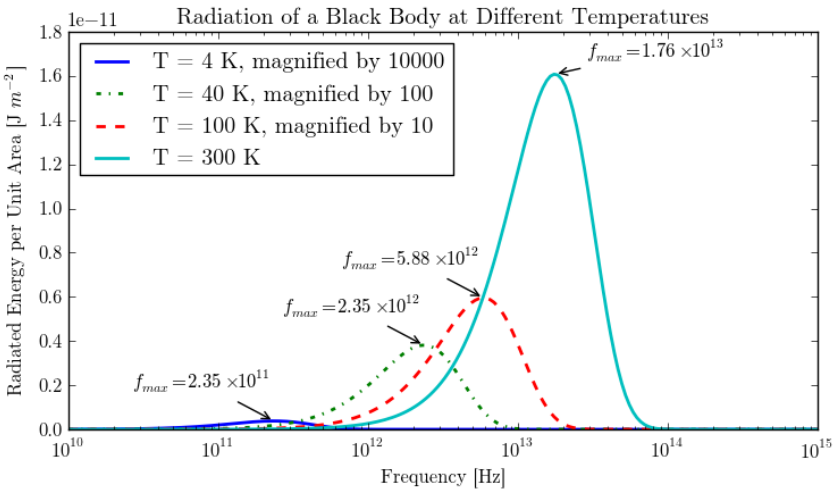

Figure 1.2: Spectrum of emitted radiation for black bodies at different temperatures (Planck's law). The curves for lower temperatures had to be magnified, since the total radiated power scales with T^4 (Stephan-Boltzmann law).

Planck's law [1901] gives the amount of radiation emitted by a black body of temperature θ at a frequency ν as

$$u = \frac{8\pi h\nu^3}{c^3} \frac{1}{e^{\frac{h\nu}{k\theta}} - 1}, \tag{1.4.1}$$

where $k = k_b$ is Boltzmann's constant.

A black body at room temperature emits a wide spectrum of radiation up to $\approx 80\,\mathrm{THz}$, with a maximum at $f = 17.6\,\mathrm{THz}$ (for $T = 300\,\mathrm{K}$, see figure 1.2). The whole terahertz range is therefore flooded with *thermal radiation*.

In order to conduct measurements in the terahertz range, this background radiation has to be avoided. This is primarily done in two ways:

- Cooling to cryogenic temperatures
- Gated detection and/or phase sensitive amplification of the detector signal (e.g. lock-in)

Apart from generating these unwanted thermal radiations, however, black body radiation can also be used as a source in so called *glow bars*. A common type of setup uses a chopper in combination with a lock-in amplifier to distinguish the emitted terahertz radiation from the background.

Photoconductive Antenna

A brief description of the working principle of *photoconductive antennas* (PCA) can be found in [Sherwin, 2002]:

> An electric field of about $10^6\,\mathrm{V\,cm^{-1}}$ is generated in a high-resistance semiconductor by applying a d.c. voltage between a pair of electrodes bonded to its surface. An ultrafast laser pulse illuminates the semiconductor between the electrodes, creating a large density of mobile charge carriers (electrons and 'holes') through an effect that is closely related to the photoelectric effect used in solar cells. These charge carriers, sensing the large electric field, accelerate at roughly $10^{17}\,\mathrm{ms^{-2}}$ [...]. All accelerating charges emit electromagnetic radiation. These charge carriers, reaching their maximum velocity in less than $10^{-12}\,\mathrm{s}$, emit a single electric-field pulse shorter than $10^{-12}\,\mathrm{s}$ that contains a broad range of frequencies, up to a few terahertz. Typically, the average power generated by this method is less than $10^{-6}\,\mathrm{W}$. But as this power is in a stable, coherent beam with well-known temporal characteristics, it can be used for spectroscopy with high spectral resolution and excellent signal-to-noise ratio, and even for imaging.

In order to increase the output power of a PCA, an interdigitated electrode design is used. The phase of the emitted beam depends on the polarity of the applied electric field. Adjacent fields have opposite polarity; therefore, every other field is covered by a metal mask to prevent a cancellation of the sub-beams that each field emits.

Quantum Cascade Laser

The *Quantum Cascade Laser*, invented at Bell Laboratories in 1994 [Faist et al., 1994], is a fascinating piece of physics and technology. It consists of a series of potential wells separated by tunneling barriers.

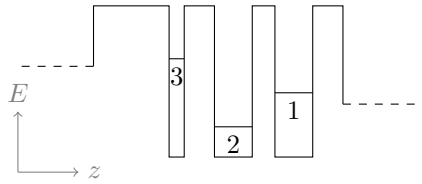

(a) Band structure of a single period QCL. Only levels contributing to the laser emission are shown.

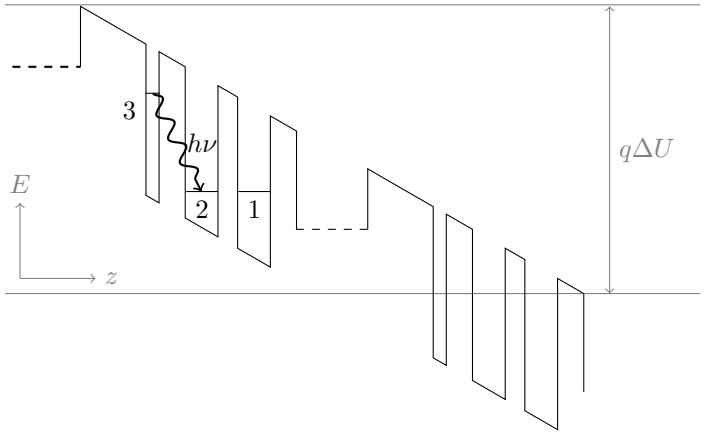

(b) Band structure of a two period QCL with applied external bias voltage (after [Faist et al., 1994]).

Figure 1.3: The band scheme of a single period of a quantum cascade laser (above) consists of a series of potential wells separated by barriers. The confinement is only one-dimensional in the direction of growth (z). The whole QCL is made up of several periods. Applying an external voltage ΔU tilts the bands (below). From the ground state of the dashed injector area, electrons can tunnel into the excited state 3 and relax into level 2, emitting a photon. They then tunnel resonantly into level 1 and are extracted into the dashed area. From this area, they are again injected into level 3 of the next period and the process continues. This way, a single electron can produce multiple photons.

Two materials (M_1 and M_2)[9] with different valence band energies ($E_1 < E_2$) are epitaxially grown on a substrate in alternating layers, creating a heterostructure. This causes a one-dimensional confinement of the electrons in the direction of growth: the layers of M_1 (the material with the lower valence band energy) serve as wells, the other layers as barriers. Inside these wells, the

[9]The first QCL used GaInAs–AlInAs, other commonly used systems are GaAs–AlGaAs, GaAs–InGaAs, GaN–InGaN. GaAs is frequently used as a base material in epitaxial growth, since there are many variations of it which have similar lattice constants.

states are quantized, their energy depending on the width of the well. This width corresponds to the thickness of the grown layer, allowing the grower to determine the energies of the states.

The idea behind the QCL is to design the energies of the states in such a way that tunneling causes population inversion (see figure 1.3). An external voltage ΔU is applied to the structure, tilting the bands. This shifts the levels inside the wells, aligning levels 2 and 1 and enabling resonant tunneling between them. Electrons are injected into level 3 and relax into level 2, emitting a photon.[10] They then tunnel into level 1 and are extracted from there. Since resonant tunneling is a very efficient process, a population inversion between the lower and upper laser level is created. In the next period, they are again injected into level 3, repeating the process. This way, a single electron can produce multiple photons. The original QCL design [Faist et al., 1994] consisted of 500 layers forming a cascade with 25 periods.

Synchrotron Radiation

When electrons are guided on a circular path at relativistic energies, they emit *synchrotron radiation*. At relativistic velocities, the emission pattern of moving charges is transformed from a standard dipole pattern to a small beam focused in the direction of movement. A derivation of this is given in most textbooks on electrodynamics.

We will use the variables β and γ in their usual relativistic definition

$$\beta = \frac{v}{c}, \gamma = \frac{E}{mc^2} = \frac{1}{\sqrt{1-\beta}}. \tag{1.4.2}$$

In [Jackson, 1998, formula (14.21)], the angular distribution of the radiated power of moving charges at low velocities is given as[11]

$$\frac{\partial P}{\partial \Omega} = \frac{e^2}{4\pi c^3}\dot{v}^2 \sin^2\Theta, \tag{1.4.3}$$

with the acceleration $\dot{v} = {}^{\partial v}/_{\partial t}$ and the angle of observation Θ.

For a linear movement at relativistic energies, this radiation pattern transforms into [ibid, (14.39)]

$$\frac{\partial P(t')}{\partial \Omega} = \frac{e^2\dot{v}^2}{4\pi c^3}\frac{\sin^2\Theta}{(1-\beta\cos\Theta)^5}, \tag{1.4.4}$$

leading to the familiar slanted beam cones.

[10] In reality, scattering of the electron on an acoustical phonon is approximately ten times more efficient than phonon emission [Bastard, 2012; Ferreira and Bastard, 1989; Bockelmann and Bastard, 1990]. Therefore, the relaxation happens most often without the emission of a photon. The even more efficient scattering on a longitudinal optical (LO) phonon is avoided by designing the energy difference of the lasing transition to be below the energy of a LO phonon.

[11] Please note that the following formulas are in Gaussian units. Those are deemed so useful by theoretical physicists that they steadfastly refuse to let them die.

Fourier transformation, followed by a lengthy derivation, leads to the spectral distribution of radiation of a particle moving at a relativistic speed along a circular path of radius ρ [ibid, (14.91)]

$$\frac{\partial I}{\partial \omega} = \sqrt{3}\frac{e^2}{c}\gamma\frac{\omega}{\omega_c}\int_{\omega/\omega_c}^{\infty} K_{5/3}(x)dx, \tag{1.4.5}$$

with the modified Bessel function $K_{5/3}$, $x = {}^{\omega}/_{\omega_c}$ and the critical frequency ω_c

$$\omega_c = \frac{3}{2}\gamma^3\frac{c}{\rho}. \tag{1.4.6}$$

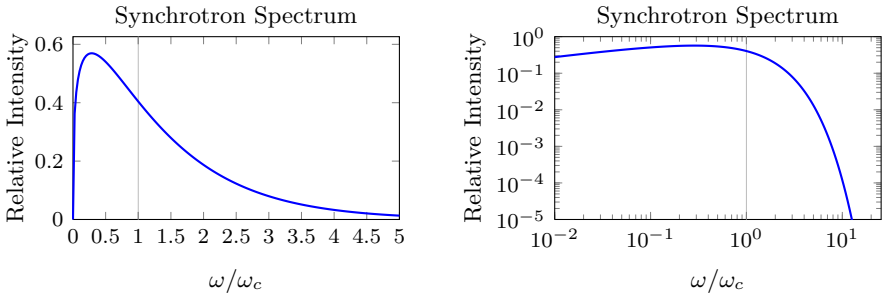

Figure 1.4: Normal and doubly logarithmic plot of the relative intensity of emitted synchrotron radiation. The critical intensity ω_c splits the spectrum into two halves of equal weight. For $\omega < 0.02 \times \omega_c$ and $\omega > 1.86 \times \omega_c$, the intensity is below $< {}^1/_e$ of the maximum Intensity.

Centering the bandwidth (see figure 1.4) around a frequency of 1 THz implies an upper frequency limit of $\omega_c = 2\pi \times 10^{12}/1.86 = 3.38 \times 10^{12}$. From the definition of ω_c, we get

$$\gamma = \sqrt[3]{\frac{2\rho\omega_c}{3c}}. \tag{1.4.7}$$

Given a medium sized accelerator of radius $\rho = 100\,\text{m}$, we need a Lorentz factor $\gamma = \sqrt[3]{1.24e5} \approx 107$ to reach ω_c. This corresponds to a very low accelerator energy of $\approx 55\,\text{MeV}$. If we confine the electron on a much smaller path of radius $\rho = 1\,\text{m}$, the result is even more favorable, namely $\gamma \approx 23$ ($E \approx 10\,\text{MeV}$). Even if a critical frequency of 1 THz is required ($\omega_c = 6.28e12$), with 50% of synchrotron radiation emitted above this frequency, the values of γ are quite small: $\gamma \approx 11$. This shows that the generation terahertz synchrotron radiation starts at low minimal energies.

To study nonlinear effects, very high output powers are required. The total output power scales with $a^2\gamma^4$. Higher values of γ than these minimal ones are therefore desirable in practice to increase the intensity of the source. Since

the speed of the electron is already very close to c, the acceleration $a = {}^{v}/_{\rho}$ is determined mostly by the radius. Sharp bends and large energies are thus desirable.

In regular accelerators, synchrotron radiation is mostly an unwanted energy loss mechanism. After the realization that this radiation offers an intense and brilliant[12] source of radiation, different methods were devised to harness this radiation for experimental purposes.

The crudest way to access synchrotron radiation is to provide a hole in the shielding around an accelerator and build an experimental setup around the provided beam line. In order to increase the radiation at such a spot, the electrons need to be accelerated further. The easiest way to do this is to introduce an artificial bend.

The next evolutionary step from a single artificial bend is the undulator (or wiggler), a series of magnetic fields with alternating polarity, bending the path in opposite directions. The synchrotron radiation emitted at the different bends interferes, and at a certain resonance frequency, constructive interference occurs. This provides a very intense, narrow-band and coherent source of radiation: the free electron laser (FEL). By changing either the magnetic field strength of the wiggler or the acceleration of the electrons the FEL can be tuned.

While conventional accelerator based sources of synchrotron radiation guide the electrons in a mostly circular path, this is not necessary for FELs. Undulators are usually integrated into straight parts of the electron path.

Most free electron lasers are parts of huge facilities, such as the Linac Coherent Light Source (LCLS) at the Stanford Linear Accelerator (SLAC) or the European X-Ray Free Electron Laser (XFEL) currently under construction in Germany. Construction costs of these devices are in the range of $10^8 - 10^9$ Euro. Facilities of this type operate with peak powers of MeV, reaching average cw[13] powers of 20 W [Carr et al., 2002].

These facilities are top-of-the-line, but due to their extremely expensive construction and high operational costs, they are difficult to access, and therefore out of reach for most researchers. As a light-weight alternative, offering some of the benefits of these huge facilities, tabletop ($1\,\mathrm{m} \times 2\,\mathrm{m}$) FELs [Jeong et al., 2009] have been developed.

Detecting Terahertz Radiation

Most generation methods can also be used to detect radiation. It is, for instance, possible to measure the photocurrent caused by a beam of terahertz radiation hitting a photoconductive antenna.[14]

[12] Brilliance is the spectral radiance inside 10^{-3} of the total bandwidth. A high brilliance corresponds to a large number of photons per second in a tightly focused beam of small bandwidth.

[13] Continuous wave, in contrast to pulsed. Continuous sources typically reach higher average but lower peak powers than pulsed ones.

[14] These currents, however, are very weak and require amplification.

In addition to these dual-use methods, there are some methods unique to detection. These include the big category of thermal detectors. For detailed information on these, the interested reader is again referenced to [Lee, 2008, ch.4.9].

We will only present electro-optic detection, the detection method used in our measurement setup.

Electro-Optic Detection

Electro-optic detection is based on the Pockels effect. A static electromagnetic field inside a birefringent crystal influences the strength of the birefringence, changing the effective refractive index and rotating the polarization.

In the terahertz electro-optic detection scheme, an optical and a terahertz beam co-propagate inside a birefringent crystal. The optical beam's frequency is three orders of magnitude higher than that of the terahertz beam. From its perspective, the terahertz electromagnetic field is therefore almost static. The field strength and polarity of the terahertz beam cause a rotation of the phase of the optical beam.

If one would try to measure the changes in the polarization of a continuous optical beam directly, one would only measure an average polarization, since the detectors are too slow to measure in real time. Therefore, both beams have to be pulsed with pulse durations shorter than $1\,\mathrm{THz}^{-1} = 1\,\mathrm{ps}$. The shorter the pulse, the higher the temporal resolution.[15] Delaying one of the beams, it is possible to measure the other beam and sample its transient by varying the delay time.

Further information is given in [Lee, 2008].

1.5 Metamaterials

The basic idea of a metamaterial is best explained by looking at an older incarnation of the same principle, the artificial dielectric [Collin et al., 1991, ch.12 "Artificial Dielectrics", p.749]:

> An artificial dielectric is a large-scale model of an actual dielectric, obtained by arranging a large number of identical conducting obstacles in a regular three-dimensional pattern. [...] Under the action of an external applied electric field, the charges on each conducting obstacle are displaced so as to set up an induced field [...]. Each obstacle thus simulates the behavior of a molecule (or group of molecules) in an ordinary dielectric [...].

Like the artificial dielectric, an artificial material (metamaterial) is a much larger model of an actual material.

[15] The temporal resolution limits the frequency resolution (see page 46).

A fundamental description of the interaction of electromagnetic radiation with matter is the Lorentz model. The bound electrons of the atoms that compose the crystal lattice of a solid are modeled as classical harmonic oscillators. These oscillators are excited by an incident plane electromagnetic wave and radiate energy.

The key idea behind the metamaterial is to replace the oscillating atoms by resonant elements, acting like small antennas. This is possible because the nature of the oscillator is irrelevant, so long as its size is small compared to the wavelength of the incident radiation. In this case, the wave is too "myopic" to resolve the details of the oscillator. Instead of atoms the beam excites a resonant circuit; the metamaterial becomes a much larger model of a material.

A normal solid is made up of atoms, in most cases aligned in a grid.[16] A metamaterial, analogously, is made up of resonant circuits, called meta-atoms. A regular grid of these meta-atoms forms a meta-surface and a stack of meta-surfaces becomes a metamaterial.[17]

Unlike a normal solid, the single oscillators can be designed and manipulated at one's whim. By choosing the resonant frequency of the meta-atoms it is possible to create materials with an arbitrary refractive index.[18] In addition, it is also possible to stack layers with different refractive indices, creating a gradual change of the refractive index. The theory of transformation optics allows the construction of a material that guides the light around an object – the famous metamaterial cloak [Schurig et al., 2006].

More information on the theory and design of metamaterials can be found in the standard works by Marqués et al. [2011] and Capolino [2009].

The reaction of a material to an incident electromagnetic wave is described using the electric permittivity ε_r and the magnetic permeability μ_r. They are effective parameters, describing average properties of the material. In the general case, they take the form of tensors, but they can be simplified to scalars for isotropic materials. Assigning these parameters to the layers of artificial resonators justifies using the term meta*material*.

History of the Field[19]

The earliest ancestor of metamaterials are artificial dielectrics, invented in the 1940s[20] and used as microwave antenna lenses in the 1950s and 1960s. The

[16] Exceptions include amorphous materials and quasi-periodic crystals.

[17] Strictly speaking, the designs presented in this thesis are meta-surfaces. We will, however, follow the example of many other authors and omit this fine distinction, using the more familiar term (planar) metamaterial instead.

[18] In [Choi et al., 2011], a refractive index of $n = 38.6$ in the terahertz range is reported.

[19] This overview is structured according to Ziolkowski [2005].

[20] The term "artificial dielectric" was introduced by Kock [1948]. He also uses the analogy of a natural material to describe his invention:

> The artificial dielectric material [...] was arrived at by reproducing, on a much larger scale, those processes occurring in the molecules of a true dielectric [...].

The same author already expressed this idea in an earlier paper [1946] without using the term.

wavelength in the microwave region is in the range of 10 cm and lenses need to be large compared to the wavelength in order to avoid diffraction. This leads to large and heavy lenses. As a light-weight alternative, artificial dielectrics were created.

An introduction into the theory of artificial dielectrics can be found in [Collin et al., 1991, ch.12 "Artificial Dielectrics"]. Most of it can also be applied to metamaterials.

Another ancestor are artificial chiral materials, built in the 1980s and 1990s for microwave radar absorption.[21] Radar absorption was also one of the starting points for John B. Pendry's work. A colloquial description of the history of his research in this area can be found in [Beech, 2012, p.139]:

> As part of their research into minimizing the radar signature of naval warships the Marconi [Materials Technology] engineers had developed a new carbon material [...]. The problem was, however, that they had no clear idea as to why it worked. It was at this point, then in the mid-1990s, that Pendry, as a renowned researcher in solid state physics and electromagnetic theory, was called in. Could he find out how the material functioned [...]?
>
> The answer [...] lay within the fuzzy fiber strands out of which the radar absorbing carbon material was made. These strands, it transpired, were just the right length and shape to interact with the electrical component of a wave with wavelength in the radar region of the electromagnetic spectrum. The various strands in the fiber essentially acted as small receiving antennas, and when the radar beam fell upon them they were able to absorb part of its energy [...].

The results of this work [Pendry et al., 1996, 1998] on the unusual interaction of certain materials with the electrical field spawned related research into the manipulation of the magnetic field. The combination of these ideas led to the split ring resonator [Pendry et al., 1999]. This design was subsequently adapted to the microwave range and manufactured [Smith et al., 2000].

Applications

In the same year, Pendry [2000] proved that a slab of a medium with a negative index of refraction ($n < 0$) would work like a perfect lens. As we will explain later (see page 19), this is possible if $\varepsilon_r < 0$ and $\mu_r < 0$.[22]

The invention of transformation optics ([Leonhardt, 2003, 2006; Pendry et al., 2006]) allowed complete control of the propagation of electromagnetic

[21] The interested reader will find further references on this topic in [Ziolkowski, 2005].

[22] The best choice is $\varepsilon_r = -1$ and $\mu_r = -1$, since this material would be perfectly matched to vacuum (and very well matched to air), suppressing reflections on the surface. This choice has the drawback that it leads to $n = -1$. Such a lens will just refocus the image without magnifying it. It can therefore only be used in near field optics.

Year	Publication	Theme
1948	[Kock, 1948]	Artificial Dielectric
1968	[Veselago, 1968]	Negative Index of Refraction
1996	[Pendry et al., 1996]	Studies on plasmons
1998	[Pendry et al., 1998]	in metal rods. $\varepsilon_r < 0$
1999	[Pendry et al., 1999]	SLR Design
2000	[Smith et al., 2000]	SLR Manufactured
	[Pendry, 2000]	Perfect Lens Theory
2001	[Shelby et al., 2001]	$n < 0$ shown directly
2003	[Leonhardt, 2003]	Transformation optics
2006	[Leonhardt, 2006]; [Pendry et al., 2006]	Controlling the propagation of EM Radiation
	[Schurig et al., 2006]	2D Microwave Cloak

Table 1.2: Time line of influential metamaterial papers.

radiation.[23] In this theory, wave propagation in a medium is described by wave propagation in a warped vacuum space. The medium is replaced by a transformed virtual space, the geometry of which is determined by ε_r and μ_r [Leonhardt, 2003] " Electromagnetic waves in a 2-D dielectric experience the medium as effective space-time curvature."

The concept of transformation optics is a generalization of the optical path length, in which the delay that a beam of light experiences due to the lower speed of light in a medium with a larger refractive index is explained by a longer path length (a thicker virtual medium). The equivalent transformation is a stretching in all directions.

This idea was later refined and led to the development of cloaks.[24] They were first demonstrated for hiding 2D objects in the microwave range [Schurig et al., 2006], where the macroscopic wavelength makes manufacturing metamaterials easier. The idea has since been extended to the infrared ("optical frequencies") [Gabrielli et al., 2009]. A 628 nm design was also proposed [Cai et al., 2007]). Another manufactured cloak [Ergin et al., 2010] hides a 3D object (a 1 µm high bump in a gold surface) at a wavelength of $\approx 1.5\,\mu\text{m} - 2.6\,\mu\text{m}$.

As noted above, transformation optics allows full control over the path of electromagnetic radiation. Cloaks connect current metamaterial research

[23] [Chen et al., 2010] is an accessible introduction into this topic.

[24] There are two ways to make an object invisible: Either by matching the refractive index to that of the surrounding medium, thus preventing refraction, reflection and absorption, (index matching) or by redirecting all radiation around the object (transformation optics). In his lecture, Ulf Leonhardt [2011] likened them to two fictional characters: the protagonist of "The Invisible Man" (H.G. Wells) swallows a chemical substance that changes his body structure, so that his refractive index is the same as that of air. The "Invisible Woman" (Stan Lee, Marvel Comics) is able to bend light, redirecting the rays around her.

with its roots in stealth technology. They are, however, only one of the many fascinating potential applications [Chen et al., 2010]:[25]

> With the aid of metamaterials, the appeal of transformation optics goes beyond invisibility: it can create fascinating effects such as electromagnetic wormholes, hidden gateways and 'optical black holes'. Light-guiding and light-bending capabilities can give rise to conceptual devices such as field concentrators (hyperlenses), field rotators, field shifters, bending wave guides, as well as all types of lens and advanced devices.

Frequency selective surfaces are another method to control wave propagation. The structure of the manufactured surface leads to resonant absorption or reflection. The position and width of the resonance can be tailored, allowing very narrow-band mirrors, band-pass filters and almost perfect absorbers.

In principle, the conductive elements that metamaterials are made of are antennas. Like any other antenna, they can be used to concentrate the field at a certain point. This field enhancement can then be used to generate the high field strengths necessary to study nonlinear effects.

The Lorentz Model of Solids

Metamaterial research is the physical realization of the oscillator model of a solid. We will now give a quick introduction in order to explain its basic features.

An electron is modeled as point particle of charge q and mass m, attached to its equilibrium position with a spring. The stiffness of this spring influences the resonance frequency ω_0. The oscillation is dampened by the factor γ. An electromagnetic wave, represented by the time dependent electric field $E(t)$, excites the system and causes the electron to move. This dampened driven harmonic oscillator is described by the following differential equation[26]

$$\frac{\partial^2 x}{\partial t^2} + \gamma \frac{\partial x}{\partial t} + \omega_0^2 x = \frac{q}{m} E(t). \tag{1.5.1}$$

The incoming radiation is assumed to be a plane wave

$$E(t) = E_0 e^{-i\omega t} \tag{1.5.2}$$

that causes the electron to oscillate in phase

$$x(t) = x_0(\omega) e^{-i\omega t}. \tag{1.5.3}$$

The amplitude of the oscillation is described by x_0. It is determined by the field strength of the incoming wave E_0 and the detuning between the frequency

[25] The original text includes references to primary sources that are omitted here.

[26] For the derivations in this section see [Jackson, 1998, ch.7.5 (p.309 – 313)] and [Lee, 2008, ch.2.1.4 (p.19 – 21)].

ω of the incoming wave and the resonance frequency ω_0 of the oscillator. The amplitude function has a Lorentzian-like shape:

$$x_0(\omega) = \frac{qE_0}{m} \frac{1}{\omega_0^2 - \omega^2 - i\omega\gamma}. \tag{1.5.4}$$

Electric Susceptibility

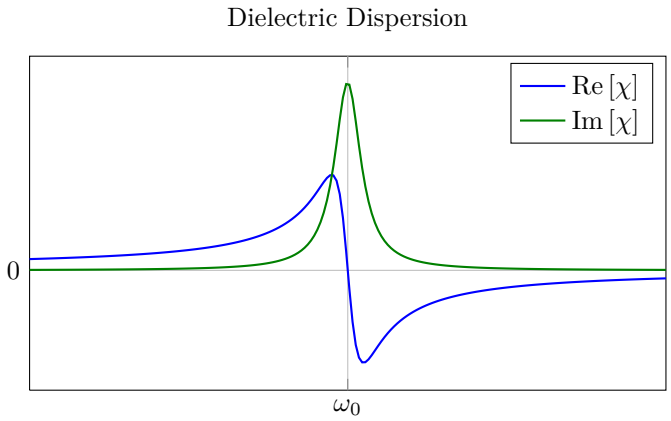

Figure 1.5: Real and imaginary part of the susceptibility around ω_0 in the Lorentz model. The amplitude of the peak depends on ω_p^2, while the dampening γ determines its width. The relation between susceptibility and permittivity $\varepsilon_r = 1 + \chi$ also connects their real and imaginary parts: $\mathrm{Re}\,[\chi] = \mathrm{Re}\,[\varepsilon_r] - 1$, $\mathrm{Im}\,[\chi] = \mathrm{Im}\,[\varepsilon_r]$.

If a material with a density of N oscillators is hit by an incoming plane wave, it will become polarized:

$$P(t) = Nqx(t) = \frac{Nq^2}{m} \frac{1}{\omega_0^2 - \omega^2 - i\gamma\omega} E_0 e^{-i\omega t}. \tag{1.5.5}$$

As explained in appendix A.2, the polarization is linked to the electrical field by $P(t) = \varepsilon_0 \chi E(t)$. Comparing this to the above formula, we get the electric susceptibility χ [Lee, 2008, eq.(2.51)]

$$\chi = \frac{Nq^2}{m\varepsilon_0} \frac{1}{\omega_0^2 - \omega^2 - i\gamma\omega}. \tag{1.5.6}$$

After extending the fraction with $\left(\omega_0^2 - \omega^2 + i\gamma\omega\right)$, we can separate the real

and imaginary part:

$$\mathrm{Re}\left[\chi\right] = \frac{Nq^2}{m\varepsilon_0} \frac{\omega_0^2 - \omega^2}{\left(\omega_0^2 - \omega^2\right)^2 + \omega^2\gamma^2}, \tag{1.5.7}$$

$$\mathrm{Im}\left[\chi\right] = \frac{Nq^2}{m\varepsilon_0} \frac{\omega\gamma}{\left(\omega_0^2 - \omega^2\right)^2 + \omega^2\gamma^2}. \tag{1.5.8}$$

Since $\varepsilon_r = 1 + \chi$, this result is also valid for the relative electric susceptibility.

The sign of the real part $\mathrm{Re}\left[\chi\right]$ is determined by $\omega_0^2 - \omega^2$, becoming negative for $\omega > \omega_0$. If $\chi < -1$, $\varepsilon_r = 1 + \chi$ will also be negative.

Ideal Conductors

For metals, the situation is slightly different. They can be approximated as ideal conductors, described by the equation of motion

$$m\ddot{x} = qE(t). \tag{1.5.9}$$

This is equivalent to setting $\gamma = 0$ and $\omega_0 = 0$ in the original equation of motion (1.5.4). Instead of repeating the same steps for this new equation, we directly insert $\gamma = 0$, $\omega_0 = 0$ into the equation for the electric susceptibility χ (1.5.6). We arrive at:

$$\chi = -\frac{Nq^2}{m\varepsilon_0} \frac{1}{\omega^2} = -\frac{\omega_p^2}{\omega^2}. \tag{1.5.10}$$

In this equation, we introduced the plasma frequency ω_p:

$$\omega_p = \sqrt{\frac{Nq^2}{m\varepsilon_0}}. \tag{1.5.11}$$

For frequencies below the plasma frequency ($\omega < \omega_p$), $\varepsilon_r < 0$. Since the plasma frequency is linked to an electronic resonance, the magnetic permeability μ_r is still positive ($\mu_r > 0$). The refractive index $n = \sqrt{\varepsilon_r \mu_r}$ will therefore become imaginary, prohibiting propagation. This is the reason for the high reflectivity of most metals. The permeability ε_r has large negative values (< -2000), causing them to be practically opaque [Gao et al., 2012]:

> When it comes to the negative permittivity, generally, the real permittivity of metals is negative below the plasma frequency, which is usually in the visible or near ultraviolet band. However, this negative permittivity is meaningful only in the vicinity region of plasma frequency because of the giant dissipation at much lower frequencies.

Negative Index of Refraction

In the previous section, we looked at the case of negative electric permittivity $\varepsilon_r < 0$ and positive magnetic permeability $\mu_r > 0$. We showed that the refractive index n becomes imaginary and the oscillations are attenuated.

But what happens if μ_r is negative at the same time? The well known relation $n^2 = (\varepsilon_r \mu_r)^2$ would invite one to assume that n is, in this case, a positive real number. But Veselago [1968] showed that this would violate causality. If $\varepsilon_r < 0$ and $\mu_r < 0$ we need to take the negative root of

$$n = \pm\sqrt{\varepsilon_r \mu_r} \tag{1.5.12}$$

instead.

A medium with $n < 0$ has various interesting properties. Refraction will obviously reverse its direction, an incident beam being refracted to the other side of a perpendicular line. In addition to this, the Poynting vector $\vec{S}$ and the wave vector $\vec{k}$ become anti-parallel. This leads to the counterintuitive effect that the direction of propagation is opposite to that of energy transfer. In this case, the Poynting vector $\vec{S}$, the electric field $\vec{E}$ and the magnetic field $\vec{B}$ follow a left-hand rule instead of the usual right-hand rule. A very good visualization of the effects this causes can be found in the online materials that accompany the paper by Ziolkowski [2003].

There are various names for materials with a negative refractive index. Depending on the author, they are called "negative index materials" (NIM), "doubly negative materials" (since $\varepsilon_r < 0$ and $\mu_r < 0$), "left-handed materials" (due to the left-hand rule explained above) or "Veselago media".

1.6 Mathematical Methods

Finite-Difference Time-Domain (FDTD)

The *Finite-Difference Time-Domain* method (FDTD), first described by Yee [1966], is the most popular algorithm for solving Maxwell's equations. [27]

A (finite) volume is divided into a grid of many small, discretized volume elements. On this grid, the differential Maxwell equations are approximated by equations containing only finite differences between neighboring grid points.[28] In each volume element, the components of the $\vec{H}$ and $\vec{E}$ field are stacked in the manner shown in figure 1.6 and figure 1.7, constructing the so called Yee lattice.

Every time step is split in two halves and the time evolution of the system is calculated in a leap-frog manner: In the first sub-step, the $\vec{E}$ field is calculated

[27] A detailed text on FDTD is [Taflove and Hagness, 2000]. An overview of many different methods for solving the Maxwell equations, including sample implementations, can be found in [Bondeson et al., 2005].

[28] This is based on a Taylor expansion that can be found in [Bondeson et al., 2005, ch.3 eq.(3.1) – (3.4)]. The gory details of three dimensions are explained in [Taflove and Hagness, 2000, ch.3.6.3]

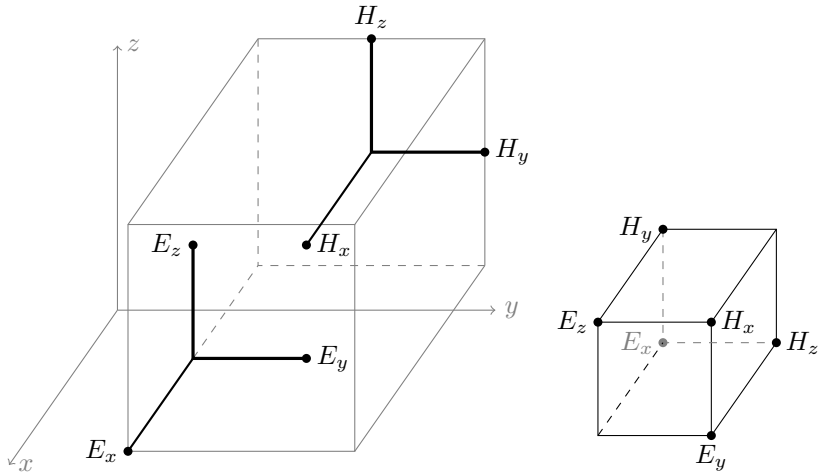

Figure 1.6: The reduced unit cell of the Yee lattice (right) is constructed by stacking the components of the $\vec{E}$ and $\vec{B}$ field (left). The origins of the two right-hand systems are offset by half a lattice length in each direction $(1/2, 1/2, 1/2)$.

using the stored values of the $\vec{E}$ and $\vec{H}$ field. The second sub-step uses the fresh values of $\vec{E}$ and the stored values of $\vec{H}$ to calculate new values for $\vec{H}$.

Compared to other Maxwell solvers, FDTD is computationally inexpensive.[29] The increase in computing power and available memory made it the default method for the simulation of electromagnetic components.

Solving Systems of Linear Equations

The dipoles and their couplings are described by a large system of linear equations. It is convenient to write such a system as a matrix equation.

A general system of linear equations

$$\begin{aligned} a_{11}x_1 + a_{12}x_2 + \cdots + a_{1n}x_n &= y_1 \\ a_{21}x_1 + a_{22}x_2 + \cdots + a_{2n}x_n &= y_2 \\ &\vdots \\ a_{n1}x_1 + a_{n2}x_2 + \cdots + a_{nn}x_n &= y_n \end{aligned} \tag{1.6.1}$$

[29] For a comparison of the asymptotic behavior ($\mathcal{O}$) of different algorithms see [Davidson, 2005, ch.1.3–1.5].

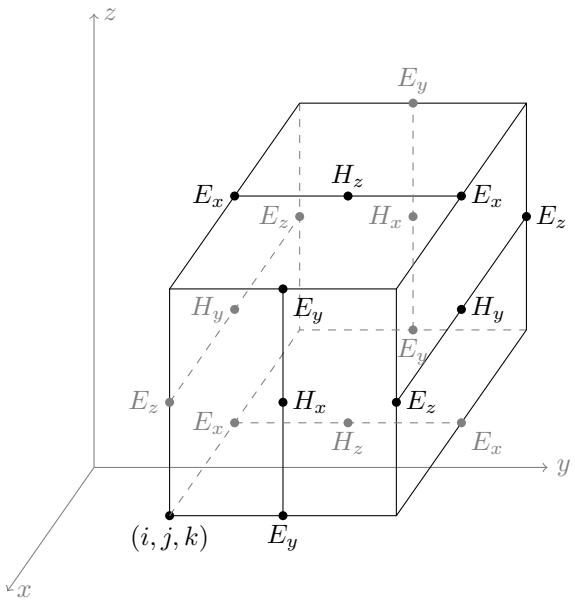

Figure 1.7: The Yee lattice as presented in [Yee, 1966].

can be written as a single matrix equation

$$\underbrace{\begin{pmatrix} a_{11} & a_{12} & \cdots & a_{1n} \\ a_{21} & a_{22} & \cdots & a_{2n} \\ \vdots & \vdots & \ddots & \vdots \\ a_{n1} & a_{n2} & \cdots & a_{nn} \end{pmatrix}}_{M} \underbrace{\begin{pmatrix} x_1 \\ x_2 \\ \vdots \\ x_n \end{pmatrix}}_{X} = \underbrace{\begin{pmatrix} y_1 \\ y_2 \\ \vdots \\ y_n \end{pmatrix}}_{Y} \tag{1.6.2}$$

$$M \cdot X = Y. \tag{1.6.3}$$

If the system of equations can be solved, M^{-1} (the inverse of M) exists, so that

$$\underbrace{M^{-1}M}_{\mathbb{1}} X = M^{-1}Y \tag{1.6.4}$$

$$X = M^{-1}Y. \tag{1.6.5}$$

LU Decomposition

A more efficient way of solving matrix equations is LU Decomposition. It avoids the calculation of the inverse matrix M^{-1} and instead decomposes M into a lower (L) and an upper (U) triangular matrix, so that $M = L \cdot U$. The original equation then becomes $L \cdot U \cdot X = Y$. After introducing $U \cdot X = y$, the equation

becomes $L \cdot y = Y$. These last two equations are then solved independently, using back substitution and forward substitution. This process is explained in [Press, 1992, ch.2.3], which also contains algorithms for LU decomposition.

Genetic Algorithms

Genetic algorithms are part of the wider field of *heuristic* optimization. These algorithms try to solve a problem by taking only a limited subset of all possible solutions into account. This is necessary, because there is a large class of problems in which the search space increases exponentially with the number of variables. For a large number of variables, these problems can no longer be solved by conventional algorithms.

Heuristic algorithms avoid the – sometimes impossible – search in the complete solution space and focus on regions that promise to contain good solutions. The exact balance between taking into account as many solutions as possible and focusing on promising ones is called the exploration-exploitation trade-off.

Blind spots are a part of their working principle; therefore, there are always cases in which they cannot find the optimal solution. While this sounds like a big drawback, in practice the *best* solution is not necessary and a sufficiently *good* one can be used instead.

Heuristic algorithms can be divided in two classes, *deterministic* and *non-deterministic*. The former produce the same result on every run, while the latter contain an element of randomness so that the result can vary between runs.

A *genetic algorithm* (GA) keeps track of a set of solutions and varies them according to a number of fixed rules that can contain a random[30] element. The GA terminology is chosen in analogy to natural selection: The set of solutions is called a *population*, consisting of *individuals*. The space of possible solutions consists of all possible values of all variables. A variable of a solution is called a *gene* and each solution is characterized by a chain of genes called the *genome*.

The first step of a GA is to create an initial population. Starting from this, the next generation is generated until a termination condition (convergence of solution, maximum number of generations, ...) is reached. The next generation is calculated using the following steps:

1. Select
2. Combine
3. Mutate

The steps are, again, an analogy to the process of natural selection. The individuals in a population compete against each other to *select* mating partners. The selected partners then exchange parts of their genome, creating a new individual from the *combined* parts. *Mutations* are added to randomly change small parts of the genome and new individuals replace some of the old ones.

[30] Some authors prefer the term "aleatoric".

An important concept is the *fitness* of an individual. It is linked to the quality of a solution so that individuals with a higher fitness represent better solutions. The genetic algorithm tries to find the individual with the maximal fitness.

There are different methods for each of the components of genetic algorithms (encoding of the parameters, initialization, selection, combination, mutation) resulting in many different implementations and an overwhelming mass of publications that cover their theory and applications. A much more detailed overview than the one we could give can be found in [Michalewicz, 1996].

Electromagnetic Applications

Genetic algorithms have been widely applied in the design of electromagnetic elements [Weile and Michielssen, 1997] and have yielded a number of interesting new antenna designs. Several groups have already combined them with electromagnetic solvers to simulate metamaterials for various frequency ranges [Bossard et al., 2009; Chen et al., 2008; Gingrich and Werner, 2005]. The main disadvantage of this approach lies in the computational requirements. The simulation of a single design takes several hours. Current computational power makes this approach feasible, but a single run of the optimization still takes days of processor time.[31]

Since the fitness function needs to be evaluated for every individual, it is the bottleneck of the whole algorithm. The simple model presented in the next chapter looked like a very promising candidate for this application. Section 2.6 explains how we used our model inside a fitness function and presents the results.

[31] In [Bossard et al., 2009], the authors use a cluster with a total of 32 cores. They simulate a population of 32 individuals (one per core) for 100-200 generations, a complete run taking 5 hours.

Chapter 2

Analytical Model

2.1 Introduction

We want to describe the reaction of a metamaterial in which the single meta-atoms are composed of thin wires to electromagnetic radiation.

A thin wire is a conducting element whose width is small compared to its length. Charges are confined to the inside, and are only allowed to move along its axis.

An external electric field $\vec{E}$ causes charges inside each wire to move. One way of simplifying the material's response is to model the movement of the charges within the wire by the movement of the center of charges. As a first order approximation, we assume that it each wire is a dipole. The interactions between the wires are thus replaced by the interactions between electrically coupled dipoles.

Previous Work by Petschulat et al.

Figure 2.1: C, S and L – the three structures described in [Petschulat et al., 2010]

.

This work is based on a model introduced by Petschulat et al. [2010], which approximates a planar metamaterial by a system of conductively coupled dipoles.

In their paper, Petschulat et al. describe the response of materials made up of three simple meta-atoms. These structures, which they call C, S and L are shown in figure 2.1.

We will present their derivation and carry the idea further by taking into account more complex grid-based structures.

Assumptions

The model as proposed by Petschulat et al. requires the following assumptions:

- The conductive elements are thin wires, i.e. their length l is much larger than their width w ($l \gg w$). This allows us to assume that their charges only move in longitudinal direction, leading to a single resonance.
- Only nearest neighbors couple.

For our extensions of the original model, we had to introduce additional assumptions:

- We will only consider wires on a grid, i.e. only certain placements and orientations are permitted.
- We assume a relative permeability close to 1 ($\mu_r \approx 1$).

No assumptions are made about the nature of the coupling. In our measurements, we proved that conductive coupling dominates.

Parameters

The model has several parameters:

- $f_{0[x|y]}$, the resonance frequency of a dipole in x or y direction,
- $q_{[x|y]}$, the charge of a dipole in x or y direction,
- $\gamma_{[x|y]}$, the damping factor of a dipole in x or y direction,
- A, the amplitude of the whole curve,
- d, the thickness of the surface layer,
- σ, the perpendicular coupling constant, and
- τ, the longitudinal coupling constant.

In this chapter we will describe these parameters more closely. Furthermore, we will compare their expected behavior with observations from our measurements. In the structures that we manufactured, we varied the lengths of the wires in x (L_x) direction (see 3.4 page 49). The length in y direction (L_y) was kept constant.

Applying the Model to the Terahertz Range

Petschulat et al. only validated their model for the optical range by comparing its results to FDTD calculations.

The first step before using this model in the terahertz range was to check if the model's assumptions still hold for those frequencies. In order to do so, the C, S and L structures from the paper were rescaled to show resonances around 0.5 THz. A finite element analysis (using the commercial software COMSOL Multiphysics) was employed to get an idea of the electrodynamic behavior.

The rescaled structures were then fabricated. We measured the structures using our terahertz TDS (time-domain spectroscopy) setup and determined the model's parameters by fitting the model to the experimental data.

2.2 Basic Model

Forces on a Dipole

Starting from the equation $\vec{F} = m\vec{a} = m\ddot{\vec{x}}$ in a single dimension, we take into account the following forces:

$$F = F_{el} - F_r - F_d - F_f \tag{2.2.1}$$

with

$$F_{el} = F_{\text{electric field}} = qE, \tag{2.2.2}$$

$$F_r = F_{\text{restore}} = kx = m\omega_0^2 x, \tag{2.2.3}$$

$$F_f = F_{\text{friction}} = m\gamma\dot{x}, \tag{2.2.4}$$

$$F_d = F_{\text{dipole}} = \frac{q_1 q_2}{4\pi\varepsilon_0\varepsilon_r}\frac{1}{r^2}. \tag{2.2.5}$$

Equation of Motion

Expressing the balance of forces (2.2.1) as a function of the external electrical field $\vec{E}$, we obtain

$$F + F_r + F_d + F_f = F_{el}. \tag{2.2.6}$$

Single Dipole

As a first step, we only examine a single dipole, setting $F_d = 0$. Collecting all the terms for this dipole and dividing by m we obtain

$$\ddot{x}_1 + \omega_{01}^2 x_1 + \gamma_1 \dot{x_1} = \frac{q_1}{m_1} E_1. \tag{2.2.7}$$

In this equation, E_1 represents the strength of the electric Field $\vec{E}$ in the direction of dipole 1:

$$E_1 = \vec{E}\hat{x}_1 \text{ with } \hat{x}_1 = \frac{\vec{x}_1}{|x_1|}. \tag{2.2.8}$$

Since we are interested in the resonant frequencies of our system, we perform a Fourier transform to change from real space into frequency space. Transforming the equation of motion (2.2.7), we obtain (see appendix A.1)

$$\left(\omega_{01}^2 - \omega^2 - i\omega\gamma_1\right) x_1 = \frac{q_1}{m_1} E_1 \tag{2.2.9}$$

Introducing the abbreviation

$$A_k = \omega_{0k}^2 - \omega^2 - i\omega\gamma_k \tag{2.2.10}$$

and dropping all indices allows us to write the equation in a very compact form:

$$Ax = \frac{q}{m} E. \tag{2.2.11}$$

Perpendicular Coupled Dipoles

Estimating F_{dipole}

We now want to introduce a second dipole. The coupling between two dipoles is described by F_d. Unfortunately, it contains a quadratic term; in order to keep our model linear, we have to approximate it.

Consider two dipoles, d_1 at position x_1 and d_2 at x_2, separated by the distance r. If no external electric field is present ($E = 0$) we assume that the dipoles are unpolarized, i.e. the centers of charge are in the middle of the dipoles. In this case, the dipoles are separated by the equilibrium distance r_0. For dipoles on a square grid, $r_0 = \sqrt{L_x^2 + L_y^2}/2$.

Using the approximation $F_d = -\sigma(x_1 - x_2)$ that is derived using a Taylor series (see appendix A.3), we will now try to estimate σ. We manufactured the structures on top of gallium arsenide (GaAs) and they were therefore surrounded by air and GaAs. We assume an effective $\varepsilon_r = 1/2\,(\varepsilon_{\text{air}} + \varepsilon_{\text{GaAs}}) \approx 13/2 \approx 7$.[1] This allows us to calculate an approximate value of the dipole coupling constant σ from basic values. For typical dipole lengths of $L_x = L_y = 80\,\mu\text{m}$:

$$\sigma = \frac{q_1 q_2}{4\pi\varepsilon_0\varepsilon_r} \frac{8}{r_0^3} \approx 8.2 \times 10^{22} \times q_1 q_2. \tag{2.2.13}$$

This value is within an order of magnitude from the one used in the fit: $\sigma_{fit} = 3.6 \times 10^{23} \times q_1 q_2$, $\sigma/\sigma_{fit} \approx 1/5$.

Since $\sigma \propto r^{-3}$, we would expect σ to increase if r_0 decreases, i.e. if L_x or L_y decrease (see table 2.1). The relation for the relative coupling constant $\sigma_{rel} = \sigma/f_{0x} f_{0y}$ is slightly more complicated and will be examined in section 2.3.

[1] This averaging assumes that the field is distributed uniformly in both media. In practice, the field is concentrated in the medium with the higher permittivity. While the exact field distribution may be complicate a simple model assumes the weighted average:

$$\varepsilon_r = \frac{\varepsilon_1}{\varepsilon_1 + \varepsilon_2}\varepsilon_1 + \frac{\varepsilon_2}{\varepsilon_1 + \varepsilon_2}\varepsilon_2 = \frac{\varepsilon_1^2 + \varepsilon_2^2}{\varepsilon_1 + \varepsilon_2} \tag{2.2.12}$$

resulting in $\varepsilon_r \approx 9.4$.

L_x [µm]	L_y [µm]	r_0 [µm]	σ [(rad/s)^2]
60	80	≈ 50	$\approx 8.2 \times 10^{22}$
70	80	≈ 53	$\approx 6.8 \times 10^{22}$
80	80	≈ 57	$\approx 5.7 \times 10^{22}$

Table 2.1: Calculated coupling constant σ as a function of the equilibrium distance r_0 for different y wire lengths L_y.

.

Calculating Transmission

The model presented so far only calculates the permittivity χ. Since our setup measured the transmission of a structure, we needed a way to calculate the transmission from the permittivity.

Fortunately, this is straightforward. We start by calculating n from χ (remembering that we assumed $\mu_r \approx 1$):

$$n = \sqrt{\varepsilon_r \mu_r} \approx \sqrt{\varepsilon_r}, \tag{2.2.14}$$

$$\varepsilon_r = 1 + \chi. \tag{2.2.15}$$

We then calculate the transmission t through a slab of material of thickness d with refractive index n using the Fresnel-Airy formulas (see [Born and Wolf, 1999, ch.1.6.4, eqs.(55), (56) and (58) on p.65-66]). The formulas assume a slab with refractive index n_2 between two media of refractive index n_1 and n_3. The beam incides on the surface of the material at angle ϑ_1. It is then refracted twice, first at an angle of ϑ_2 on the interface between 1 and 2, then at an angle of ϑ_3 between 2 and 3.

$$t = \frac{t_{12} t_{23} e^{i\beta}}{1 + r_{12} r_{23} e^{2i\beta}} \tag{2.2.16}$$

with

$$\beta = 2\pi f d n_2 = 2\pi f d \sqrt{\varepsilon_r}, \tag{2.2.17}$$

$$t_{12} = \frac{2 n_1 \cos\vartheta_1}{n_1 \cos\vartheta_1 + n_2 \cos\vartheta_2}, \qquad t_{23} = \frac{2 n_2 \cos\vartheta_2}{n_2 \cos\vartheta_2 + n_3 \cos\vartheta_3}, \tag{2.2.18}$$

$$r_{12} = \frac{n_1 \cos\vartheta_1 - n_2 \cos\vartheta_2}{n_1 \cos\vartheta_1 + n_2 \cos\vartheta_1}, \qquad r_{23} = \frac{n_2 \cos\vartheta_2 - n_3 \cos\vartheta_3}{n_2 \cos\vartheta_2 + n_3 \cos\vartheta_3}. \tag{2.2.19}$$

Note that we had to introduce the new parameter d, the thickness of the slab. Since we only have a single layer of our metamaterial, this parameter is not connected to a physical property and can be chosen at will. To arrive at a value that we could use, we performed a fit for d and used its rounded result in our calculations.

In our experiment, the sample was manufactured on top of GaAs, leading to a stack of layers $l_1 =$ Air, $l_2 =$ Structure, $l_4 =$ GaAs and $l_3 =$ Air. To exclude the effect of the substrate, we used a piece of GaAs without any resonator structures as a reference. We therefore had $n_1 = n_3 = n_{Air} \approx 1$. The incidence of the beam was perpendicular to the surface ($\vartheta_i = 0$, $\cos\vartheta_i = 1$). Inserting these conditions, we get a slightly simpler formula:

$$t = \frac{\frac{2}{1+n_2}\frac{2n_2}{n_2+1}e^{i\beta}}{1+\frac{1-n_2}{1+n_2}\frac{n_2-1}{n_2+1}e^{2i\beta}}. \tag{2.2.20}$$

Alternative Method

The Nicholson-Ross-Weir method [Nicolson and Ross, 1970; Weir, 1974] offers a different way of extracting the material parameters ε_r and μ_r. It is based on a transmission matrix formalism. A relation between the transmission and reflection coefficients, refractive index n and impedance Z is used [Smith et al., 2002]. The material parameters are then given by $\varepsilon_r = {}^{n}/_{Z}$ and $\mu_r = nZ$.

To apply this method, we would have to modify our setup to measure reflection spectra. Since we were only dealing with electric dipoles and therefore only concerned with the relative electric permittivity ε_r, it offered no advantage to us that would have justified this additional effort.

System of Two Coupled Dipoles

We now examine a system of two coupled dipoles, with $F_d \neq 0$. Starting once again from the balance of forces, we obtain two coupled equations:

$$\ddot{x}_1 + \omega_{01}^2 x_1 + \gamma\dot{x}_1 - \sigma(x_1 - x_2) = \frac{q_1}{m_1}E_1, \tag{2.2.21}$$

$$\ddot{x}_2 + \omega_{02}^2 x_2 + \gamma\dot{x}_2 - \sigma(x_2 - x_1) = \frac{q_2}{m_2}E_2. \tag{2.2.22}$$

f_0 [THz]	ω_0^2 [(rad/s)^2]	ω_0^2/σ
0.5	$\approx 9.9 \times 10^{24}$	≈ 20
1.0	$\approx 4.0 \times 10^{25}$	≈ 80

Table 2.2: Comparison of ω_0^2 and σ for a typical value of $\sigma = 0.5 \times 10^{24}\,\mathrm{s}^{-2}$.

A quick estimate (see table 2.2) shows that $\omega_0^2 \gg \sigma$. We can therefore neglect the term σx_1 in the first equation and the term σx_2 in the second equation. After Fourier transform, we finally obtain the familiar equations of two coupled dipoles

$$\left(\omega_{01}^2 - \omega^2 - i\omega\gamma_1\right)x_1 + \sigma x_2 = \frac{q_1}{m_1}E_1, \tag{2.2.23}$$

$$\left(\omega_{02}^2 - \omega^2 - i\omega\gamma_2\right)x_2 + \sigma x_1 = \frac{q_2}{m_2}E_2. \tag{2.2.24}$$

Using the variable A_k defined in equation (2.2.10), we get a very compact form:

$$A_1 x_1 + \sigma x_2 = \frac{q_1}{m_1} E_1, \tag{2.2.25}$$

$$A_2 x_2 + \sigma x_1 = \frac{q_2}{m_2} E_2. \tag{2.2.26}$$

This can be generalized to the equation of a dipole x_k

$$A_k x_k + \text{couplings} = \frac{q_k}{m_k} E_k. \tag{2.2.27}$$

A method for constructing this system of equations for arbitrary grid-based shapes will be shown in sections 2.5.

The above system of equations can be rewritten in matrix form as:

$$\underbrace{\begin{pmatrix} A_1 & \sigma \\ \sigma & A_2 \end{pmatrix}}_{M} \underbrace{\begin{pmatrix} x_1 \\ x_2 \end{pmatrix}}_{X} = \underbrace{\begin{pmatrix} \frac{q_1}{m_1} E_1 \\ \frac{q_2}{m_2} E_2 \end{pmatrix}}_{E}. \tag{2.2.28}$$

And be solved for X by calculating the inverse of M: $X = M^{-1} \cdot E$.

For numerical purposes, it is actually easier to solve the system of equations using LU decomposition instead of the matrix inversion. In MATLAB, this is done using the `MRDIVIDE` Operator (\): $X = M \backslash E$.

2.3 Parameter Dependence of Transmission

To improve our understanding of the behavior of our model, we simulated the transmission as a function of the model's parameters.

Resonance Frequency

The plot in figure 2.2a shows the result of varying f_{0y} while fixing the *relative* value of γ_y and σ_{rel}. The frequency of the peak approaches $f = 0$ on a linear tangent.

Fixing their *absolute* values would cause the relative values to increase for lower frequencies, resulting in a higher relative damping. This would cause the resonance in y direction to gradually disappear, vanishing below a cutoff frequency.

It is clearly visible that the minima approach the tangents (dashed lines, horizontal at $f = 1\,\text{THz}$ for f_{0x} and diagonal $f = f_{0y}$ for f_{0y}).

If no coupling is present ($\sigma = 0$, as in figure 2.2b), the transmission minima perfectly follow the tangents, crossing at $f_{0y} = f_{0x}$. For $\sigma \neq 0$, however, the minima deviate more and more from their respective tangents the closer they get to this crossing point. This behavior is a consequence of the coupling and is called *avoided crossing*.[2]

[2] In quantum physical measurements an avoided crossing is often used to prove the presence of a coupling.

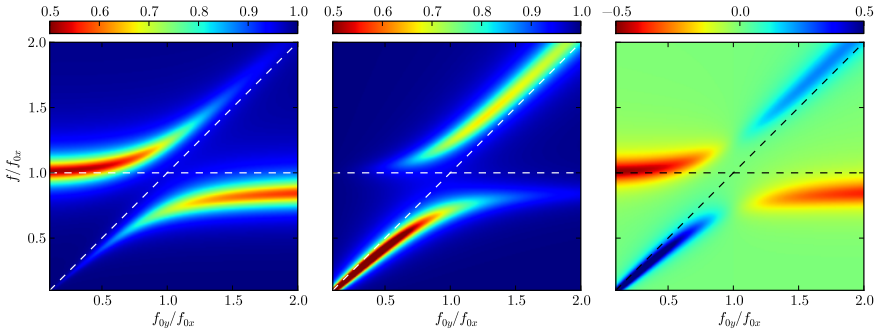

(a) Coupled dipoles, $\sigma_{rel} = 0.5 \neq 0$

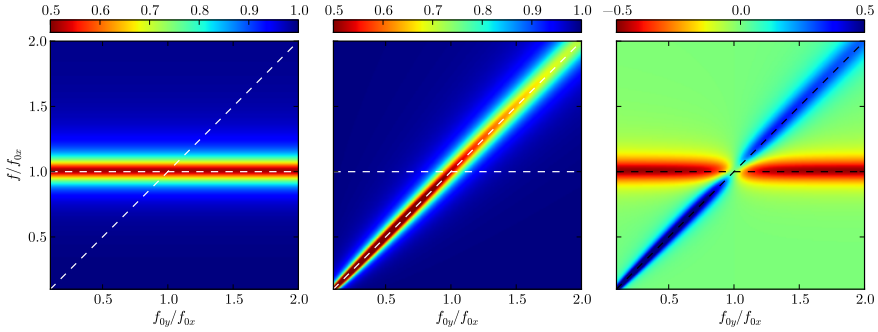

(b) Independent dipoles, $\sigma = 0$

Figure 2.2: Frequency dependent transmission of *coupled* ($\sigma \neq 0$, above) and *separated* dipoles ($\sigma = 0$, below) in X polarization (t_x, left), Y polarization (t_y, middle) and the difference between them ($t_x - t_y$, right) as a function of the resonance frequency of the y dipole (f_{0y}). All other parameters are kept constant. The axes are scaled relative to $f_{0x} = 1\,\mathrm{THz}$. An avoided crossing is visible in the graphs depicting the coupled dipoles.

The situation shown in figure 2.2a can be applied to the situation in the L structures, which we will present in the next chapter (see section 3.2, especially tables 3.3 and 3.2b). The $L_x = L_y = 80\,\mu\mathrm{m}$ structure corresponds to the transmission at $x = {}^{f_{0y}}/_{f_{0x}} = 1$. $L_x = 70\,\mu\mathrm{m}$ and $L_x = 60\,\mu\mathrm{m}$ are at slightly higher values of x, 1.13 and 1.27, respectively.

Thickness d

Reviewing the formula for the transmission 2.2.20 we discover that the thickness d only enters in the terms $e^{i\beta}$ and $e^{2i\beta}$, with $\beta = 2\pi f d n$

Since we divide the transmission data by a GaAs reference without structures, we examine ${}^{t_{sample}}/_{t_{ref}}$. This division results in a subtraction in the exponents. Therefore, we can not separate between d and ε_r. Instead, we al-

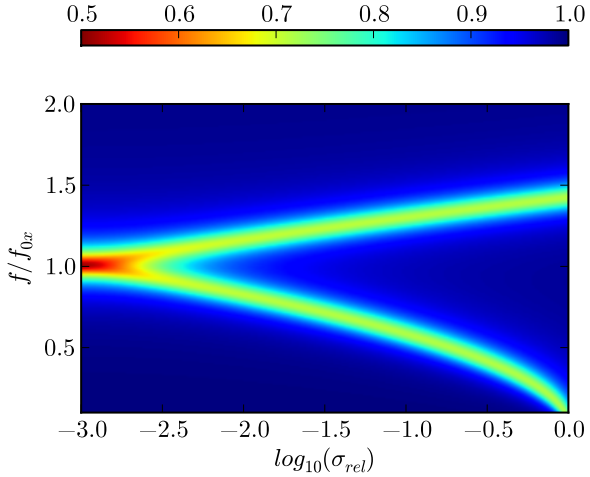

Figure 2.3: Transmission for $f_{0x} = f_{0y} = 1\,\mathrm{THz}$ and varying values of $\sigma_{rel} = {}^{\sigma}/_{(f_{0x} f_{0y})}$. The split increases linearly with σ. For $\sigma_{rel} \to 1$ the frequency of the lower peak goes to $\to 0$, vanishing for $\sigma_{rel} = 1$. This process slightly distorts the linear relationship.

ways see a mixed parameter $dn_{sample} - dn_{ref} = d\Delta n$. If we had chosen lower values for q_x and q_y, resulting in a larger dielectric constant ε_r and thus a larger refractive index n, we could have chosen a bigger d.

Perpendicular coupling σ

Comparing the transmission with and without coupling (figure 2.2) shows the influence of the perpendicular coupling constant σ. It causes a split between the resonance frequencies. The strength of the coupling influences the distance of the split. In figure 2.3 we explore this process in more detail. The relationship between the separation between the peaks and the value of σ_{rel} is practically linear.

As demonstrated by our experimental results (see 3.2), we could directly estimate σ from our measurements. We could also determine σ more closely by fitting measured transmission data for simple shapes with calculations from the analytical model.

Charge density q and dampening γ

The shape and depth of the dips in transmission are influenced by the damping parameter γ and the charge density q. Higher values of ${}^{q}/_{\gamma}$ result in sharper (thinner) and deeper dips.

2.4 Longitudinal Coupling

Two dipoles on a rectangular grid can either be collinear (they form a straight line) or perpendicular (they meet at a right angle). The model discussed so far only allowed for perpendicular coupling, described by the (perpendicular) coupling constant σ. It does not contain any statement about longitudinal coupling and is, therefore, only applicable to structures composed solely of rectangular bends. Since these shapes are a very limited subset of all possible structures on a grid, we extended this model to account for longitudinal coupling (coupling along the axis of the dipole) as well. To this end, we introduced the longitudinal coupling constant τ.

We call a system of N perpendicular coupled dipoles a long dipole of length N. It is described by the equation $M \cdot X = \tilde{E}$. In x direction M, X and $\tilde{E}$ are given by

$$X = \begin{pmatrix} x_0 \\ x_1 \\ \vdots \\ x_{n-1} \\ x_n \end{pmatrix}, \; \tilde{E} = \frac{q_x}{m_x} E = \frac{q_x}{m_x} \begin{pmatrix} E_x \\ E_x \\ \vdots \\ E_x \\ E_x \end{pmatrix},$$

$$M = \begin{pmatrix} A_x & \tau & 0 & \cdots & 0 \\ \tau & A_x & \tau & \ddots & \vdots \\ 0 & \ddots & \ddots & \ddots & 0 \\ \vdots & \ddots & \tau & A_x & \tau \\ 0 & \cdots & 0 & \tau & A_x \end{pmatrix}. \tag{2.4.1}$$

The results for y are analogous.

Calculating τ

In order to determine τ, we examine the permittivity in x-direction

$$\chi_{xx} = \frac{\eta q_x^2}{\epsilon_0 m} \chi \tag{2.4.2}$$

of a varying number of dipoles coupled along the axis.

In appendix A.5, we derive the eigenfrequencies of chains of one and two dipoles. In the lossless case ($\gamma = 0$), they are:

$$\omega_1 = \omega_0, \tag{2.4.3}$$

$$\omega_{2,1/3} = \sqrt{\omega_0^2 \pm \tau}. \tag{2.4.4}$$

Two dipoles of length L coupled in a straight line should behave like a single dipole of length $2L$. Since the eigenfrequency ω_0 of a dipole is given by

$\omega_0 = \frac{c\pi}{L}$, the resulting ω should be $\frac{\omega_0}{2}$.

$$\omega_{2,3} = \sqrt{\omega_0^2 - \tau} = \frac{\omega_0}{2} \tag{2.4.5}$$

$$\omega_0^2 - \tau = \frac{\omega_0^2}{4} \tag{2.4.6}$$

$$\tau = -\frac{3\omega_0^2}{4} \tag{2.4.7}$$

Inserting this into $\omega_{2,1}$ and $\omega_{2,3}$ yields

$$\omega_{2,a} = \frac{\omega_0}{2}, \tag{2.4.8}$$

$$\omega_{2,b} = \frac{\sqrt{7}\omega_0}{2}. \tag{2.4.9}$$

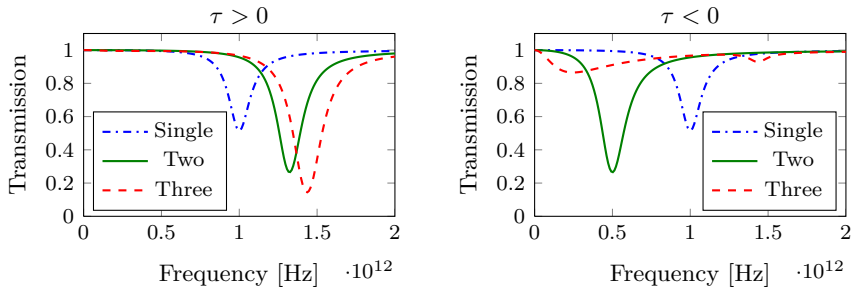

Figure 2.4: Comparison of the transmission for $\tau > 0$ (left) and $\tau < 0$ (right). The curves represent different numbers of longitudinally coupled dipoles. The resonance frequency $f_0 x$ was set to 1 THz.

Solving the above set of equations for $\omega_{2,1}$ leads to a different sign, namely $\tau = \frac{3\omega_0^2}{4}$. To decide between these two different values for τ, we inserted them into our model. From figure 2.4 we see that the negative sign leads to the expected behavior.

2.5 Transmission of Arbitrary Structures

Algorithm

The algorithm to calculate the transmission of an arbitrary structure has the following steps:

1. Generate the coupling matrix M, the vector of carrier displacements inside the dipoles X and the electric field applied to each dipole E.

2. Remove empty rows and columns

3. Solve the matrix equation $M \cdot X = E$ for X.

4. Calculate χ

$$\begin{aligned}\chi &= \begin{pmatrix} \chi_{xx} & \chi_{xy} \\ \chi_{yx} & \chi_{yy} \end{pmatrix} \\ &= \eta \begin{pmatrix} \sum_i q_x x_i|_{E_x=1,E_y=0} & \sum_i q_y x_i|_{E_x=0,E_y=1} \\ \sum_i q_x y_i|_{E_x=1,E_y=0} & \sum_i q_y y_i|_{E_x=0,E_y=1} \end{pmatrix}. \end{aligned} \tag{2.5.1}$$

5. Calculate the transmission (as explained in 2.2).

How to calculate the coupling matrix for structures placed on a rectangular grid is explained in the next section. An implementation in MATLAB can be found in appendix B.1.

Dipoles on a Rectangular Grid

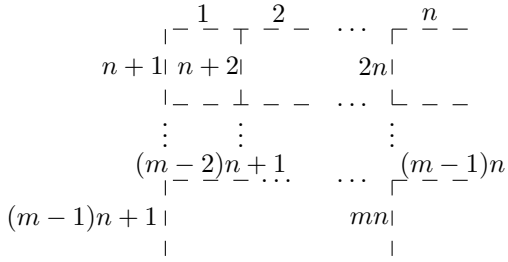

Figure 2.5: Enumerating grid positions.

After introducing the perpendicular and the longitudinal coupling, we will now place the dipoles on a grid. We only allow two kinds of dipoles, in x and y direction, and require all dipoles in one direction to have the same parameters (f_0, γ, q). Furthermore, they can only occupy discrete positions, creating a grid.

The first step of the algorithm we presented in the previous section requires calculating the coupling matrix. In order to apply it to arbitrary structures, we need a systematic way to calculate this matrix.

We start by enumerating the grid left to right, top to bottom, beginning in the top left corner. We choose to start with a row of x dipoles and enumerate x and y rows alternately (see figure 2.5, an example is shown in 2.6). This enumeration scheme maps grid positions to the positions inside a vector. If there is a dipole at the k^{th} position on the grid, there will be a 1 at position k of the vector encoding the grid. Otherwise, the entry at position k will be 0.

For an example of the enumeration scheme see figure 2.6 where the vector $(0, 1, 0, 0, 1, 0, 1, 0, 0)$ encodes an S shape.

If the number of rows m and the number of columns n are different ($m \neq n$) the values for m and n are written at the end of the vector, separated by

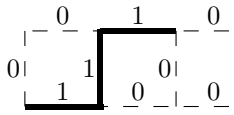

Figure 2.6: The vector $(0,1,0,0,1,0,1,0,0)$ encodes the S structure on a 3×3 grid. The same structure could also be encoded as $(0,0,1,0,0,1,0,1,0)$. On a 4×4 grid, the same structure is encoded by $(0,0,1,0,0,0,1,0,0,1,0,0,0,0,0,0)$, but can also be encoded in many equivalent vectors.

semicolons.[3] Example: $(1,0,0,1,1,1;3;2)$ (note that the dipoles do not have to be connected). In the case of a square grid ($m = n$) the values are inferred from the length of the vector and can be omitted.

Nearest neighbor couplings

The next step is to map this placement vector to a coupling matrix. One of the basic assumptions of our model (see section 2.1) is nearest neighbor coupling. This greatly simplifies the task of creating the coupling matrix.

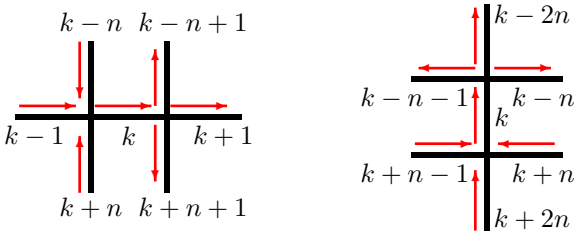

Figure 2.7: The six possible nearest neighbors for a dipole on a grid in x and y direction and their relative indices. The arrows indicate the direction of carrier movement caused by an electric field in positive x and y direction, respectively.

A dipole on a grid has six nearest neighbors (see figure 2.7). If the dipole is placed in x direction, four of them are y dipoles (top left, top right, bottom left, bottom right) and two of them are x dipoles (left, right). Similarly, a dipole in y direction has four x dipole neighbors (top left, top right, bottom left, bottom right) and two y dipole neighbors (top, bottom).

The excitation of one dipole leads to carrier movements which in turn cause the excitation of the neighboring dipoles. The sign of the coupling constant can easily be understood from the movement of the carriers. The directions indicated in figure 2.7 led to the couplings shown in table 2.3.

[3] When implementing this algorithm, the developer needs to decide how this information is stored. For this text, we merely chose a compact notation.

Index	M	C
k	$+x$	
$k-n$	$-y$	$-\sigma$
$k-n+1$	$+y$	$+\sigma$
$k+n$	$+y$	$+\sigma$
$k+n+1$	$-y$	$-\sigma$
$k-1$	$+x$	$+\tau$
$k+1$	$+x$	$+\tau$

Index	M	C
k	$+y$	
$k-n-1$	$-x$	$-\sigma$
$k-n$	$+x$	$+\sigma$
$k+n-1$	$+x$	$+\sigma$
$k+n$	$-x$	$-\sigma$
$k+2n$	$+y$	$+\tau$
$k-2n$	$+y$	$+\tau$

Table 2.3: Induced carrier movements M for a central dipole in x (left) and y (right) direction are modeled by the coupling C.

These couplings are described by the equations (in matrix form)

$$\begin{pmatrix} A_y & 0 & \sigma & -\sigma & 0 & \tau & 0 \\ 0 & A_y & 0 & \sigma & -\sigma & 0 & \tau \\ \sigma & 0 & A_x & \tau & 0 & \sigma & 0 \\ -\sigma & \sigma & \tau & A_x & \tau & \sigma & -\sigma \\ 0 & -\sigma & 0 & \tau & A_x & 0 & \sigma \\ \tau & 0 & -\sigma & \sigma & 0 & A_y & 0 \\ 0 & \tau & 0 & -\sigma & \sigma & 0 & A_y \end{pmatrix} \begin{pmatrix} y_1 \\ y_2 \\ x_5 \\ x_0 \\ x_6 \\ y_3 \\ y_4 \end{pmatrix} = \frac{1}{m} \begin{pmatrix} q_y E_y \\ q_y E_y \\ q_x E_x \\ q_x E_x \\ q_x E_x \\ q_y E_y \\ q_y E_y \end{pmatrix}, \tag{2.5.2}$$

$$\begin{pmatrix} A_y & \sigma & -\sigma & \tau & 0 & 0 & 0 \\ \sigma & A_x & \tau & -\sigma & 0 & 0 & 0 \\ -\sigma & \tau & A_x & \sigma & 0 & 0 & 0 \\ \tau & -\sigma & \sigma & A_y & \sigma & -\sigma & \tau \\ 0 & 0 & 0 & \sigma & A_x & \tau & -\sigma \\ 0 & 0 & 0 & -\sigma & \tau & A_x & \sigma \\ 0 & 0 & 0 & \tau & -\sigma & \sigma & A_y \end{pmatrix} \begin{pmatrix} y_5 \\ x_1 \\ x_2 \\ y_0 \\ x_3 \\ x_4 \\ y_6 \end{pmatrix} = \frac{1}{m} \begin{pmatrix} q_y E_y \\ q_x E_x \\ q_x E_x \\ q_y E_y \\ q_x E_x \\ q_x E_x \\ q_y E_y \end{pmatrix}. \tag{2.5.3}$$

The system of coupled differential equations for dipoles on a grid of the size $m \times n$ can be written as a matrix with $nm \times nm$ entries. The matrix is a band matrix – the non-zero entries are limited to diagonal bands – and its structure is very similar to an adjacency matrix. The equation for x and y Dipoles are of the form

$$\underbrace{-\sigma\sigma\ldots\tau}_{-m} A_x \underbrace{\tau\ldots\sigma}_{m} -\sigma, \tag{2.5.4}$$

$$\overbrace{\tau\ldots-\sigma\underbrace{\sigma\ldots}_{-m}}^{-2m} A_y \overbrace{\underbrace{\ldots\sigma-\sigma}_{m}\ldots\tau}^{2m}. \tag{2.5.5}$$

As an example of this procedure, the coupling matrices for the C and L shapes are derived in appendix A.4.

2.6 Metamaterial Design Using a Genetic Algorithm

The core of a genetic algorithm is the fitness function, providing a measure of the quality of a solution. We devised a simple fitness function that allowed us to tune metamaterials towards predefined transmission values t_i for predefined frequencies f_i. We then used this fitness function in combination with MATLAB's Genetic Algorithm Toolbox (GAT)[4] to develop new structures.

In analogy to natural processes, the convention in the genetic algorithm community is to maximize the fitness function. The GAT defies this convention and *minimizes* the fitness instead. A suitable candidate was therefore

$$\sum_i |t(f_i) - t_i| \,, \tag{2.6.1}$$

i.e. the sum of absolute distances[5] between the transmission value of the structure at frequency f_i and the target transmission value t_i at this frequency. The transmission function $t(f)$ returns the absolute value of the complex transmission. For an implementation that maximizes the fitness, one would multiply this function by -1.

Results

As an early test, we conducted several runs of the genetic algorithm. We looked for a structure with $t = 1$ at $f = 1\,\mathrm{THz}$ in x polarization, for a x dipole resonance frequency $f_{0x} = 1\,\mathrm{THz}$. While some runs produced only trivial solutions (see figure 2.9), others produced interesting structures such as the one shown in figure 2.8.

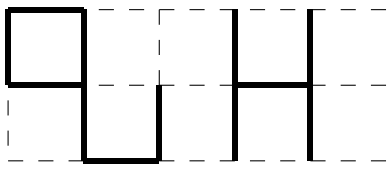

Figure 2.8: The solution (1, 0, 0, 0, 0, 1, 1, 0, 1, 1, 1, 0, 0, 1, 0, 0, 1, 1, 1, 1, 0, 1, 0, 0, 0) was produced by a run of the genetic algorithm.

To validate our result, we compared the predicted transmission spectrum with a numerical simulation. The simulation was done by Daniel Dietze using his custom FDTD solver [Dietze, 2010] (see figure 2.10).

The numerical calculation did not fully agree with the results of our model, showing only the first, lower frequency, minimum but not the second, higher

[4] In recent versions of MATLAB, the GAT has been superseded by the Global Optimization Toolbox, which contains a genetic algorithm solver.

[5] We chose the absolute values instead of the squared ones in order to create a linear fitness function.

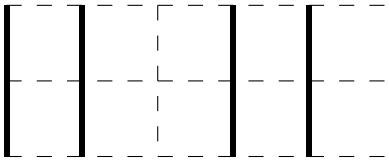

Figure 2.9: A different run on the same day produced this trivial solution (0, 0, 0, 0, 0, 1, 1, 0, 1, 1, 0, 0, 0, 0, 0, 1, 1, 0, 1, 1, 0, 0, 0, 0, 0).

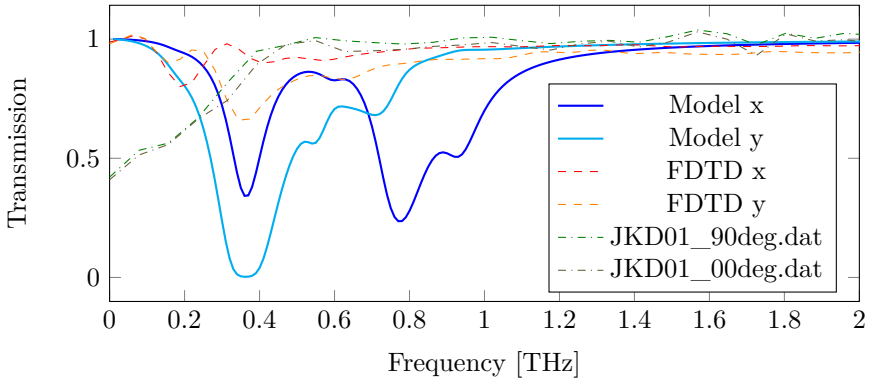

Figure 2.10: Analysis of the solution shown in figure 2.8. FDTD refers to the results from [Dietze, 2010]. The design was rescaled to $f_0 x = 0.5\,\mathrm{THz}$ on a $80\,\mu\mathrm{m} \times 80\,\mu\mathrm{m}$ grid, manufactured as JKD01 and measured.

frequency, one. We therefore decided to manufacture the structure and compare the results with measured data.

Contrary to all our expectations, the structure showed no response, lacking even the hint of a transmission minimum. We would have at least anticipated a resonance corresponding to the single dipole mode.

Since terahertz fields do not penetrate deep into the structure, they are very sensitive to surface roughness. This striking result could, therefore, be due to a problem that arose during manufacturing. Another possible reason could be that we did not properly space the single meta-atoms. Spacing was found to greatly influence the response of a metamaterial [Gay-Balmaz and Martin, 2002; Feth et al., 2010; Singh et al., 2010].

Other possible causes are related to the size of the structure. Because it is so large, different parts could be excited by the beam with different relative phases, causing the resulting currents to attenuate one another. The parts could also oscillate out of phase relative to one another, canceling each other in the far field. Our model only couples the oscillations of dipoles on a local scale, without considering the total dipole moment. Some of the modes that it takes into account lack a total dipole moment. These modes are “dark”, since they can neither be excited by plane waves nor radiate in the far field. These “dark”

modes could also help explain the differences between the FDTD calculation and the model (see figure 2.10).

Regardless of the true cause, we strongly suspected that our model completely fails to predict large structures. This led us to the conclusion that the model in its current form is not applicable to these kinds of problems.

It was out of the scope of this thesis to study the exact dynamics of the model's breakdown. Further research on this frontier, perhaps in combination with an expansion of the model by a theory that takes global phase relations into account, promises to produce exciting results.

2.7 Hexagonal Structures

In order to extend the range of structures we could model, we introduced a hexagonal grid. This allows for more complex shapes, while keeping the mathematical complexity simple.

In a hexagonal grid, each node connects three edges. The angle between two edges is always $^2/_3\pi = 120°$.

We started constructing the grid by placing an edge parallel to the x-axis at π $(-180°)$. This determines the placement of the other two axes at angles of $^1/_3\pi = 60°$ and $^{-1}/_3\pi = -60°$. The three edges, placed as in figure 2.11 in a star like fashion, will be parallel to the vectors $\begin{pmatrix}-1\\0\end{pmatrix}$, $\begin{pmatrix}^1/_2\\\sqrt{3}/_2\end{pmatrix}$ and $\begin{pmatrix}^1/_2\\-\sqrt{3}/_2\end{pmatrix}$ respectively.

The symmetry of the hexagonal grid and the vectors introduced above suggest using the base vectors[6] x, ξ and ζ:

$$x = \begin{pmatrix}1\\0\end{pmatrix} \qquad \xi = \begin{pmatrix}^1/_2\\\sqrt{3}/_2\end{pmatrix} \qquad \zeta = \begin{pmatrix}^1/_2\\-\sqrt{3}/_2\end{pmatrix} \tag{2.7.1}$$

The same base vectors are used to describe the electric field:

$$E_x = \begin{pmatrix}E_x\\0\end{pmatrix} \qquad E_\xi = \begin{pmatrix}^1/_2E_x\\\sqrt{3}/_2E_y\end{pmatrix} \qquad E_\zeta = \begin{pmatrix}^1/_2E_x\\-\sqrt{3}/_2E_y\end{pmatrix} \tag{2.7.2}$$

Basic Forms

In this section, we will devise a model for the transmission of four basic elements – the single dipole, two dipoles, three dipoles and a hexagonal ring.

The equations of motion in the hexagonal grid are derived in the same way as those for the rectangular coordinates; see appendix A.6.

To validate our approach, we manufactured these basic shapes and measured their transmission spectra. Unfortunately the measurement was inconclusive (see figure C.5).

[6] These vectors are linearly dependent and, therefore, not base vectors in the strict mathematical sense. For lack of a better term, we will nevertheless refer to them as base vectors. Note also that, instead of using $-x$ like we did during the grid construction, we define x in the usual sense. We thus avoide introducing an error prone $x \to -x$ step.

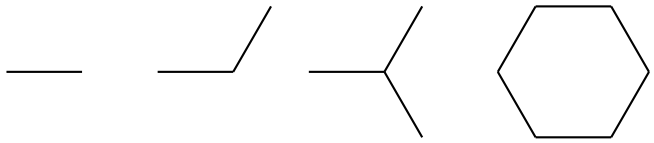

Figure 2.11: Basic forms of dipoles on a hexagonal grid.

Enumerating a Hexagonal Grid

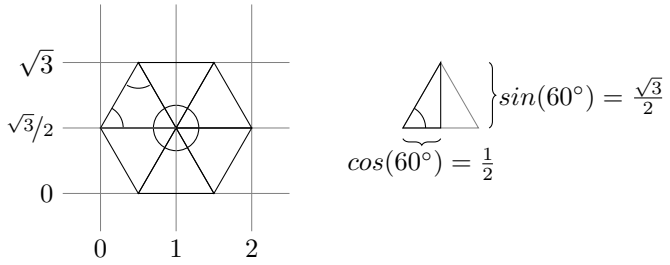

Figure 2.12: Hexagonal Geometry. All angles shown are $\pi/3 = 60°$.

A hexagon can be composed from six equilateral triangles, as shown in figure 2.12. In an equilateral triangle, all sides have the same length l and all angles equal $\frac{\pi}{3} = 60°$. Its height is $h = \sin(60°)l = \frac{\sqrt{3}}{2}l$ and the height of the hexagon is $2h = \sqrt{3}l$. The width of a hexagon is $2l$.

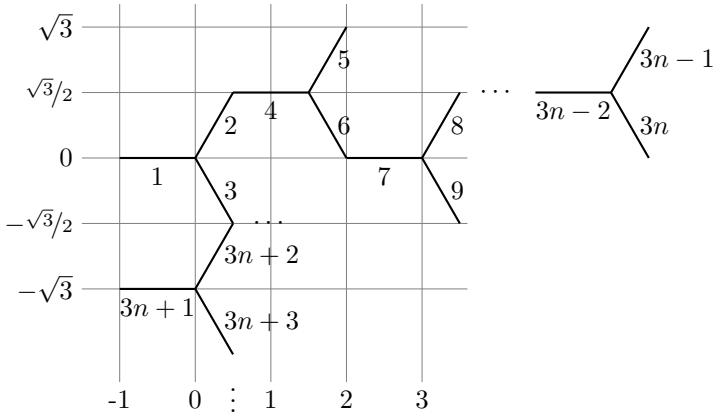

Figure 2.13: A hexagonal grid with n grid cells ($3n$ dipoles) per row.

As a unit cell for our grid, we choose a star (c.f. the numbers in figure 2.13). We enumerate its edges clockwise, starting from the left ($180° = 1$; $60° = 2$; $-60° = 3$). We place the first star at $(0, 0)$. The next star of the same row

is placed at $(1+\cos(60°), \sin(60°)) = (1.5, \frac{\sqrt{3}}{2})$ (nos. 4,5 and 6), followed by $(2, 0)$ (nos. 7,8 and 9), $(3+\cos(60°), \frac{\sqrt{3}}{2})$, and so on until the end of the row.

The next row is constructed in the same way, starting from $-2\frac{\sqrt{3}}{2} = -\sqrt{3}$ (nos. $3n+1$,$3n+2$,$3n+3$).

Nearest neighbors

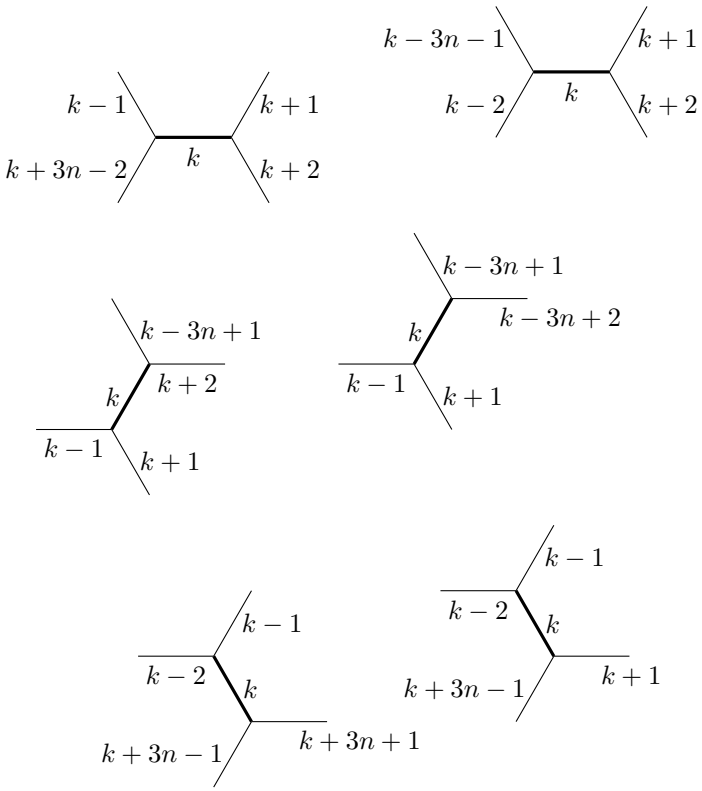

Figure 2.14: Nearest neighbors for the different elements in a hexagonal grid. The relative indices differ for odd (star in lower position, left) and even (star in upper position, right) cases. Each row of the grid consists of n stars and $3n$ dipoles. Therefore, the dipole in the same orientation one row above (below) is at $k-3n$ ($k+3n$).

Every dipole in a hexagonal grid has four nearest neighbors. Analogously to section 2.5, we look at the movements of carriers. We now have to differentiate between three types of dipoles: horizontal (180°; —), slanted upwards (60°;/) and slanted downwards (−60°;\). Furthermore, there are now two possible positions for a horizontal dipole, "upper" (in even columns) and "lower" (in odd columns), in which the indices of its neighbors differ. The relative indices

Index (odd, if different)	M –
$k+3n-2$ $(k-2)$	$+x$ $-y$
$k-1$ $(k-3n-1)$	$+x$ $+y$
$k+1$	$+x$ $+y$
$k+2$	$+x$ $-y$

Index (odd, if different)	M /
$k-3n-1$	$+x$ $-y$
$k+2$ $(k-3n+2)$	$+x$
$k+1$	$+x$ $-y$
$k-1$	$+x$

Index (odd, if different)	M \
$k-1$	$+x$ $+y$
$k+1$ $(k+3n+1)$	$+x$
$k+3n-1$	$-x$ $-y$
$k-2$	$+x$

Table 2.4: Induced carrier movements for the hexagonal grid. The carrier movements M for a central dipole k in horizontal ($-$, top), upwards (/, bottom left) and downwards (\, bottom right) direction are shown.

of the neighbors are shown in figure 2.14. The induced movements of charges are listed in tab. 2.4.

Chapter 3

Measurements

3.1 Experimental Setup

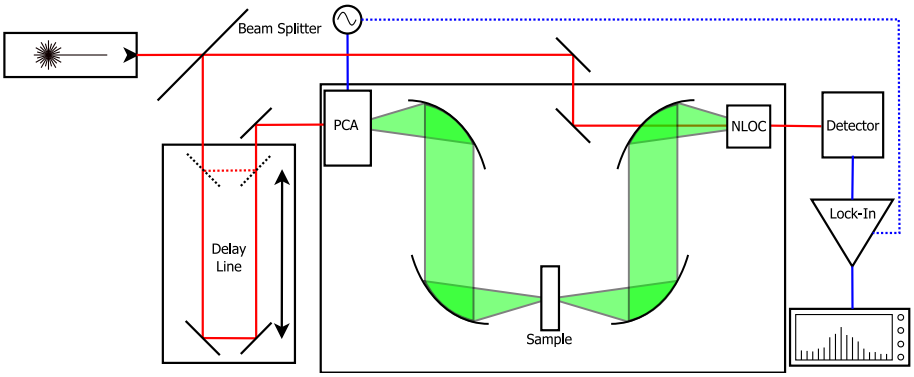

Figure 3.1: The THz-TDS setup used for our measurements.

A standard *terahertz time-domain spectroscopy* (THz-TDS) setup was used to measure the transmission of THz Radiation through the samples. The basic layout of the experiment is outlined in figure 3.1.

A commercial femtosecond laser was used to produce laser pulses with a duration of $\approx 100\,\text{fs}$ at a wavelength of 800 nm. The femtosecond laser uses a mode locked laser (Ti:sapphire) that is pumped by a Nd:YAG laser which in turn is pumped by a solid state laser diode. The Ti:sapphire laser produces femtosecond pulses with a repetition rate of $\approx 80\,\text{MHz}$.

The primary beam is split into two parts; one of them is used as a reference beam, the other passes through a delay line and is guided through the experiment. The length of the delay line is varied by moving two mirrors that are mounted on a motorized stage. After passing through the delay line, the beam incides on a photoconductive antenna (PCA) that is biased with a modulated voltage (18 kHz), producing amplitude modulated terahertz radiation.

Because this radiation is very well absorbed by water vapor, the terahertz part of the setup is purged with dry air. This reduces the humidity and leads to a lower absorption of the terahertz beam.

The divergent terahertz beam is collimated into a broad beam by a spherical mirror and focused by another mirror. The sample is mounted in the focus. After the beam crosses the sample, it is, once more, collected and focused onto a lithium niobate non-linear optical crystal (NLOC). The reference beam is also directed onto the NLOC and the slowly varying terahertz beam causes a rotation of polarization due to the Pockels effect. The details of this measurement principle are described in the section on electro-optic detection, p. 12.

After crossing the NLOC, the beam is split into two orthogonally polarized beams. The amplitude of these two beams is detected, its difference serving as detector signal.

To distinguish the signal from the infrared and terahertz background present at room temperature, the detector is connected to a lock-in amplifier (tuned to the same modulation frequency of approximately 18 kHz) which is read out using a standard PC running LabView.

Advantages and Disadvantages of TDS

The room temperature operation mentioned above is arguably the biggest advantage of the TDS setup. Furthermore, it consists of relatively few parts, making it easy to build and align. Whereas many other detectors are only power sensitive, TDS detects phase and field strength.

In order to scan the terahertz pulse, the delay length needs to be varied. In the standard TDS setup, this is done by physically moving the mirrors on an optical stage. The speed of this movement limits the scanning time. In our setup, a single scan takes approximately ten minutes. The main reason for this is the time spent moving the mirrors. This includes a delay that is inserted after each move, so that the vibrations in the moved mirrors subside.

Detailed information on the properties and applications of THz-TDS can be found in [Sakai, 2005, ch.4, p.203ff].

Resolution and bandwidth

The theoretical bandwidth limit of our setup is governed by the minimum and maximum frequency it can resolve. The theoretical maximum frequency is limited by the timestep $\Delta t = 50\,\text{fs}$. This is equivalent to a sampling frequency $f_s = {}^1/_{\Delta t} = 20\,\text{THz}$. According to the Shannon sampling theorem, this leads to a theoretical maximum frequency $f_{max} = {}^{f_s}/_2 = 10\,\text{THz}$.

Using very short pulses (15 fs), photoconductive antennas can generate radiation up to 60 THz [Sakai, 2005, p.6] while electro-optic detection is sensitive up to 70 THz [Sakai, 2005, p.34]. Since we used longer pulses (100 fs) the highest frequencies in our setup are likely around 5 THz to 7 THz.

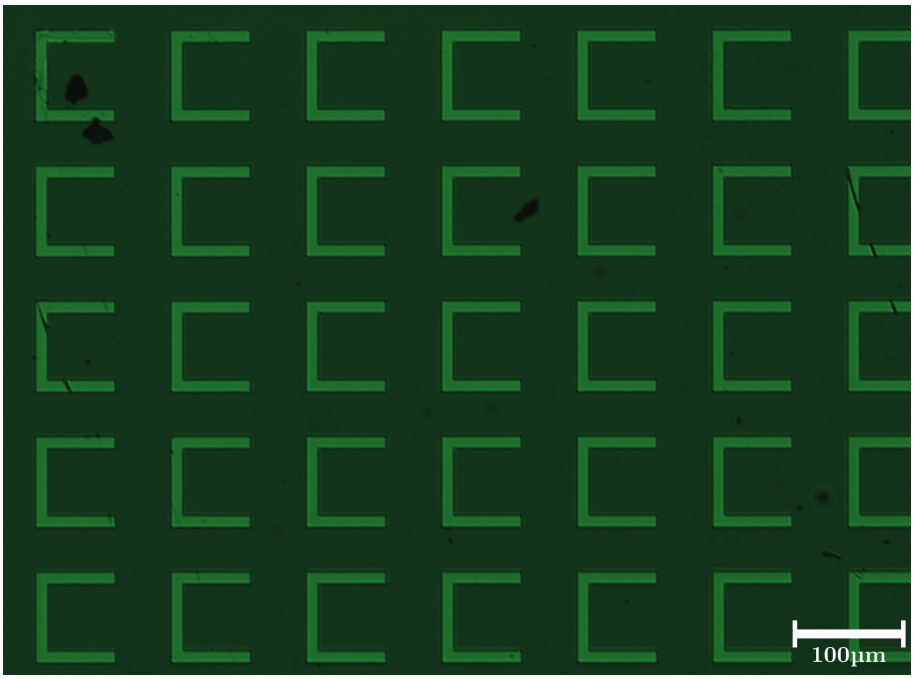

Figure 3.2: Detail of one field of a manufactured sample (CSL7080, C structure). The name 7080 stands for the lengths L_x and L_y, as indicated in figure 3.4, which are 70 µm and 80 µm, respectively. Examples for the other two shapes and structures are included in the appendix (figures C.6 and C.7). The color is due to the green light used in the microscope to illuminate the sample. Under natural light, the structured areas are golden.

The practical limit is governed by the signal to noise ratio of our detection system. While the noise floor is very constant, showing practically no change, the detector signal changes significantly. It depends on the power of the beam, which in turn depends on the quality of the purge, the output power of the primary laser and the current alignment. Depending on these factors, our setup can resolve a minimum frequency between 0.1 THz and 0.2 THz. The maximum frequency is between 2.5 THz and 3 THz, leading to an approximate bandwidth of 2.5 THz.

In our measurements, we usually evaluated 512 data points, resulting in a time window length of 25 600 fs and a frequency resolution of $\approx$ 0.04 THz (40 GHz).

Sample Manufacturing

The samples were made by depositing a layer of titanium and gold on gallium arsenide (GaAs) using standard semiconductor processes.

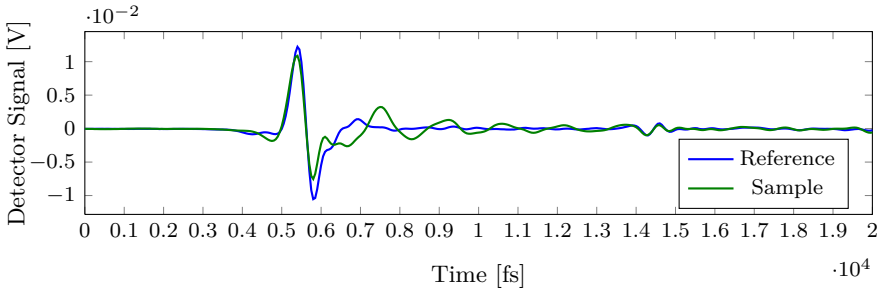

(a) Measured data

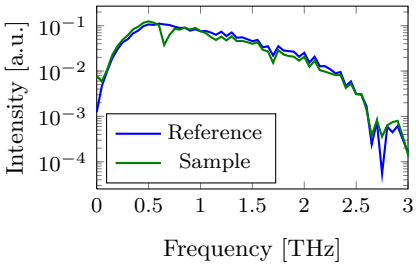

(b) Fourier Transform (logarithmic scale)

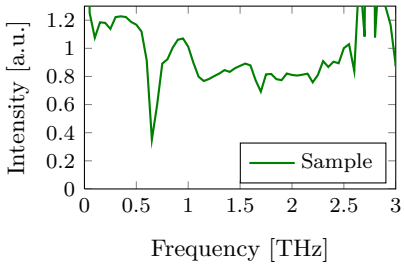

(c) Weighted

Figure 3.3: Processing of measurement data. The data shown is the SLC8060 C shape and reference field and was recorded on 20100929. Note the different depth of the water line at 2.7 THz that is visible in the fft data (below, left), indicating different water content during the two measurements.

The GaAs pieces were bought from a commercial supplier. After cleaning in acetone and isopropyl alcohol, the photo resist (AZ 5214 untinned) was deposited by spin coating at 9000 RPM for 35 s and soft baked at 100 °C for 60 s. To transfer the structures onto the sample, a laser writer (Heidelberg Instruments DWL 66fs, 2 µm write head) exposed the resist. For the development, MIF726 was used.

A 10 nm layer of titanium, followed by a 150 nm layer of gold, were deposited using an e-beam evaporation system. The titanium served as an adhesion layer, since it is hard to directly attach gold to GaAs.

The last step was the lift off procedure: the sample was immersed in Acetone for 15 min to dissolve the undeveloped resist. The deposited layers were then removed from the undeveloped parts of the sample in an ultrasonic bath. After rinsing in isopropyl, alcohol the sample was dried using N_2.

Using this process, we manufactured several samples of varying shapes and sizes. As an example, a detail of a C shape is shown in figure 3.2.

Data processing

The transient through a sample and a reference is measured (figure 3.3a). This data is then Fourier transformed (figure 3.3b). To remove the influence of the bulk substrate the FT data of the sample is weighted by that of the reference (figure 3.3c).

If the Fourier transformed data is very noisy, it is smoothed by convolution with a Hanning window. This is done for both the data and the reference before weighting. The (smoothed) data is then weighted with the (smoothed) reference.

3.2 CLS Measurements

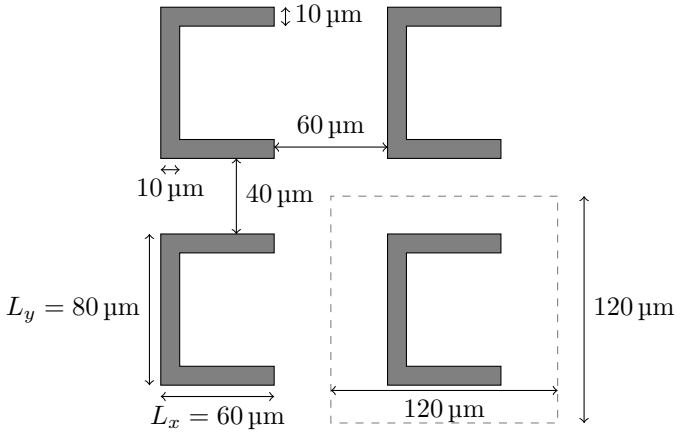

Figure 3.4: Dimensions of the structure 8060C, showing the dimensions of the structure, including the lengths L_x and L_y. L_x was varied between 60 µm (shown here) and 160 µm.

To apply the model introduced in [Petschulat et al., 2010] to the THz range, we manufactured rescaled versions of the C, S and L structures presented in the paper and measured their frequency response using THz time domain spectroscopy (TDS). We designed three versions with varying sizes in order to study the behavior of the different parameters. Each sample consisted of four fields, containing the C, L and S structure as well as an empty reference field.

Peak Positions

While the shape and depth of the dips in transmission varied between measurements of the same structure and showed poor reproducibility (see figure C.1), the position of the peaks was stable. From the absolute position of the peaks,

we can obtain information about the resonant frequencies of the oscillators, while the split between the peaks informs us about the coupling strength.

Shape	Peak	8060	8070	8080
C X	1	0.70	0.65	0.60
S X	1	0.35	0.30	0.30
	2	0.90	0.80	0.75
	split	0.55	0.50	0.45
L X	1	0.45	0.45	0.40
	2	0.75	0.70	0.65
	split	0.30	0.25	0.25
C Y	1	0.35	0.30	0.25
	2	0.75	0.70	0.65
	split	0.40	0.40	0.40
S Y	1	0.35	0.30	0.30
L Y	1	0.45	0.45	0.40
	2	0.75	0.70	0.65
	split	0.30	0.25	0.25

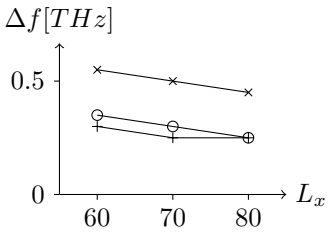

(b) ×=S X, += L X = L Y, ∘= C Y

Table 3.1: Peak frequencies and splits between peaks. All frequencies in THz. The plot on the right visualizes the split between peaks.

Fit parameters

To get a rough estimate of the parameters (see section 2.1, page 26), we used the simplex hill climbing algorithm implemented in MATLAB's `fminsearch` command. As starting parameters, we rescaled the values given in [Petschulat et al., 2010, tab. 1]. We then iterated several times, using the results from a previous run as start values for the next one.

Since A is only a scaling parameter, it was set to 1. The thickness parameter d was set to a fixed value (7.22×10^{-10} m) that was also found using `fminsearch`.

For a fixed value of d, the position of the transmission minima only depends on f_{0x}, f_{0y} and σ. The depth of the minima is mainly influenced by $q_{[x|y]}$ and $\gamma_{[x|y]}$, although the relationship between f_{0x}, f_{0y} and σ also plays a role.

L_x[µm]	f_{0x}[THz]
60	0.80 ($\approx {}^{80}/_{60}$)
70	0.70 ($\approx {}^{80}/_{70}$)
80	0.60
100	0.50 ($\approx {}^{80}/_{100}$)
120	0.40 ($\approx {}^{80}/_{120}$)
160	0.30 ($\approx {}^{80}/_{160}$)

(a) Expected

L_y[µm]	L_x[µm]	f_{0x}[THz]	Δf_{0x}[THz]
80	60	0.70	0.05
80	70	0.65	0.05
80	80	0.60	
80	100	0.50	2×0.05
80	120	0.45	2×0.025
80	160	0.35	4×0.025

(b) Measured

Table 3.2: Expected (left) and measured f_{0x} for C structures of different sizes, under the assumption that $f_{0x} = 0.6\,\text{THz}$ for $L_x = 80\,\mu\text{m}$. Note that the increase in L_x is not equidistant. Between the penultimate and the last sample it is 40 µm.

X Dipole Resonance Frequency f_{0x}

According to Petschulat's model, the effective susceptibility χ for the C structure in X polarization [Petschulat et al., 2010, eq. (7)] is given by

$$\chi_{xx}(\omega) = \frac{q_x^2 \eta}{m\varepsilon_0} \frac{2}{\omega_{0x}^2 - \omega^2 - i\omega\gamma_x}. \tag{3.2.1}$$

This only depends on f_{0x} (with $\omega_{0x} = 2\pi f_{0x}$). Since the transmission is determined by χ, the frequency of the transmission minimum in a measurement of a C structure in X polarization (C X) equals f_{0x}.

From the model of an oscillating dipole we would expect that the wavelength λ, at which a resonance occurs, has to be a multiple of the electrical length of the dipole. The first order resonance would be expected at $\left(l_{electrical} = \frac{\lambda}{4}\right)$.

Starting from $f_{0x} = 0.60\,\text{THz}$ for $L_x = 80\,\mu\text{m}$, we expect a linear scaling (see table 3.2a). Comparing the measured values of f_{0x} for the three samples SLC8060, SLC8070 and SLC8080 (see table 3.2b), we observe a decrease by $\approx 0.05\,\text{THz}$ if the length of the arm in X direction increases by 10 µm. This is a linear decrease, but the slope is only half of the expected value (table 3.2a). The shift can be observed most clearly by looking at the 8060 sample and comparing fits for $f_{0x} = 0.6\,\text{THz}$ and $f_{0x} = 0.7\,\text{THz}$ (see figure 3.7a and 3.7b). In the 8070 sample they are less pronounced, but still visible.

In order to study this more closely, structures with longer L_x lengths of 100 µm, 120 µm and 160 µm were manufactured (see table 3.2b and figure C.4a). For the first length the change in f_{0x} continues at the same rate. For the longest two lengths, this process slows down. We assume that this happens because the length becomes comparable to the wavelength. The most distant parts of the structure are therefore exposed to a different phase of the electric field, effectively shortening the structure.

To further study the onset of this slowdown, we manufacturing structures with L_x lengths of 130 µm, 140 µm and 150 µm. Unfortunately we could not measure them due to a long lasting breakdown of our setup.

Y Dipole Resonance Frequency f_{0y} and Coupling σ

For a dipole in Y direction the resonance frequency cannot be measured directly. Instead, it has to be inferred from the split between two transmission minima, which is influenced by both f_{0y} and σ.

An exception to this rule are the 8080 structures. There, f_{0y} is known, since it is identical to f_{0x}. In this case, $\sigma_{rel} = {}^{\sigma}/_{f_{0x}f_{0y}}$ can be determined directly to be ≈ 0.5. The effect of f_{0y} and σ are hard to separate.

Within the frequency resolution of our setup, we could not determine a clear change in σ_{rel}. Even for the shortest length $L_x = 60\,\mu m$, a smaller $\sigma_{rel} = 0.45$ does not lead to a better fit. We therefore concluded that σ_{rel} is constant across the range of frequencies that we examined.

L_x[µm]	f_{0y}[THz]
60	0.55
70	0.55
80	0.60

Table 3.3: Since L_y is constant, the model would predict a constant f_{0y}. The values that lead to the best fit (right), however, change with L_x.

Since the length L_y does not change, we would expect a constant f_{0y}. In our measurements, however, we found that f_{0y} shifts to lower frequencies for longer lengths of the x dipole L_x. This introduces a cross dependency between f_{0x} and f_{0y} and represents a deviation from the model.

The fact that f_{0y} shifts to lower frequencies for larger values of L_x is easily visible when comparing the fits created for $f_{0y} = 0.6\,\mathrm{THz}$ (the value found in the 8080 structure, figure 3.8a and C.3a) with those where f_{0y} has the values indicated in table 3.3 (figures 3.8b and C.3b).

Although this shift can not be explained by the model, it can easily be deduced from the equivalent LC resonator circuit, the resonance frequency ω_0 of which is given by

$$\omega_0 = \frac{1}{\sqrt{LC}}. \tag{3.2.2}$$

Thus, an increase of either L or C leads to a decrease of the resonant frequency.

In the case of a measurement in Y polarization, the arm in x direction does not contribute to the inductance, since it is perpendicular to the polarization of the electromagnetic field. The decrease of f_{0y} is therefore caused only by the increase in capacitance.

Size dependence of the fit parameters

Combining the results that we obtained so far, we can estimate the values of all parameters as a linear function of the dipole length L_x. Relative to the reference resonance frequency $f_0^{(80)} = 0.6\,\mathrm{THz}$ for $L_x = 80\,\mu\mathrm{m}$, the parameters change as

$$\begin{aligned}
f_{0x} &= f_0^{(80)} + (80\,\mu\mathrm{m} - L_x) \times 5 \times 10^{15}\,\mathrm{Hz\,m^{-1}},\\
f_{0y} &= f_0^{(80)} - (80\,\mu\mathrm{m} - L_x) \times 2.5 \times 10^{15}\,\mathrm{Hz\,m^{-1}},\\
\sigma &= f_{0x} \cdot f_{0y} \cdot \sigma_{rel},\\
\gamma_x &= f_{0x} \cdot \gamma_{x,rel},\\
\gamma_y &= f_{0y} \cdot \gamma_{y,rel},\\
q_x &= \mathrm{const},\\
q_y &= \mathrm{const},\\
d &= \mathrm{const}. \qquad (3.2.3)\\
& \qquad (3.2.4)
\end{aligned}$$

In this very simple model, the deviation that we found for long L_x lengths was not taken into account. The frequency shift of the y resonance frequency f_{0y} was distributed homogeneously between 60 µm and 70 µm.

Using this formula we can predict the model's parameters as a function of L_x. The actual position of the transmission minima can then be found from our model by numerical calculation.

We assumed the simplest possible, linear relationship. Since the effects we found are in the range of the frequency resolution of our experimental setup, the explanatory and predictive power of this parameter model is limited. To validate it, one could manufacture structures with intermediate L_x lengths. To see their, smaller, frequency changes, one would have to measure these samples with a better frequency resolution, perhaps even in a different experimental setup.

It would also be interesting to simultaneously vary L_x and L_y in order to explore the cross dependencies that this could introduce.

Further Results

We found good agreement between theory and experiment for all measurements. As predicted by the theory, C and S shape show the same behavior in Y polarization.

Examining the results for the S structure, deviations become apparent. In Y polarization, the model predicts a second transmission minimum that is missing in the experimental data. This dip is absent in all the differently scaled S structures that we manufactured.

Examining the difference between the two dips for L and S shape in the other polarization (X), a slight shift in the center frequency of the splits for the two

different structures is visible (compare the dashed to the solid green and the red lines in figure 3.7b). The exact magnitude of this shift is below our resolution. From the measured peak positions we can infer that it is $\approx 0.02\,\mathrm{THz}$. It seems that the optimal fit would have the resonance frequencies for the S shape shifted to slightly higher frequencies as compared to those of the L shape ($f_{0x}^{(S)} > f_{0x}^{(L)}$ and $f_{0y}^{(S)} > f_{0y}^{(L)}$). Of course, this would mean that the dipole resonance frequencies are no longer independent of the structure, which would violate a basic assumption of our model.

In the other polarization (X) of the same (S) structure, the model predicts a second transmission minimum that is missing in the experimental data. Both of these results occur for all structures.

Since the resonance frequencies were determined from the C structure, the fit agrees well to the data.

3.3 Structures Containing Gaps

Figure 3.5: C, S and L with gaps

In order to study the influence of capacitive coupling on the behavior of the structure, we manufactured variations of the design with gaps between the dipoles (see figure 3.5). We varied the length of the gaps between 2 µm and 10 µm. The minimal size of the gap was limited by the smallest structures we could write with our laser writer.

Increased Coupling

Figure 3.6: Normal vs. interdigitated gap design

To increase the capacitance of the gap and observe capacitive coupling, we devised a variation of the original structure with an interdigitated design of the conductors surrounding the gaps (similar to a key and slot joint, see figure 3.6). The larger surface inside the gap leads to a higher coupling capacitance. The area of the gap is effectively tripled: it is increased from 10 µm to 30 µm for a length of the "fingers" of 10 µm and a width of 2 µm.

For a general interdigitated design with n fingers of length l on both sides of a gap between conductors of width b, the length of the gap increases from b to $nl + b$. In the case of $l = b$, the length of the interdigitated gap is $(n + 1)l$.

The design with an interdigitated gap and two fingers, as shown in figure 3.6, was manufactured with a gap size of 2 µm as sample SLC8060G. The measurements show a weak coupling.

The resolution of our laser writer limited the width of the fingers, determining the maximum number we could write. Increasing the longer slot length would reduce the effective length of the dipole, shifting the resonance frequency. A further increase of the gap capacitance was therefore not possible with this method.

A promising way to further increase this capacitance consists of filling the gap with a dielectric. We did this by depositing SiN on the surface of existing samples. These samples could, however, not be measured due to the aforementioned technical difficulties.

Shape	Gap	f_{x1}	f_{x2}	f_{y1}	f_{y2}
C	g00	0.65		0.30	0.75
	gi2	0.75		0.45	0.70
	g02	0.55		0.35	0.75
	g04	0.75		0.60	-
	g10	0.60		0.75	-
S	g00	0.35	0.85	0.35	-
	gi2	0.70	-	0.55	-
	g02	0.70	-	0.60	-
	g04	0.70	-	0.60	-
	g10	0.60	-	0.85	-
L	g00	0.40	0.70	0.40	0.70
	gi2	0.45	0.75	0.50	-
	g02	0.60	0.90	0.60	-
	g04	0.85	-	0.60	-
	g10	0.70	-	0.60	-

Table 3.4: Frequencies (in THz) of the lower and higher frequency transmission minimum in x and y polarization for different gap sizes and gap designs, sorted by decreasing coupling (increasing gap distance, samples SLC8060, SLC8060G, SLC806002, SLC806004 and SLC806010). Dashed entries indicate peaks that would be expected from the model, but are absent in the measurement.

Interpretation

The absorption profile of the designs showed only small variations between 2 µm and 10 µm (see figures 3.9a to 3.10c). However, a closer look at the frequencies of the peaks (see table 3.4 reveals some interesting details.

The gap measurements show that the S structure is very sensitive against changes in the coupling. The other two structures are less sensitive and still show coupling for the two smaller gap widths. This could be caused by the different symmetry of the two structures. In the C structure, the geometric center is to the right of the vertical dipole, while it is in the center of this dipole for the S structure.

The data indicates that the resonances in the L structure are more sensitive to a change in the coupling in Y polarization. In this polarization, the shorter dipole resonates. Since the energy coupled into the dipole is proportional to the area of the antenna, the induced energy in the shorter dipole is lower. It

is not sufficient to excite the second dipole across the gap.

The capacitance C of a plate condensator is given by $C = \varepsilon \frac{A}{d}$. In our case, the surface A is given by the cross section of the gold conductors (width: 10 µm, height: 0.15 µm, cross section: 1.5 µm^2). The dielectric constant ε_r for GaAs is ≈ 12.[1] For the 2 µm gap this leads to: $C = 12 \cdot \varepsilon_0 \frac{1.5\,\mu\text{m}^2}{2\,\mu\text{m}} = \varepsilon_0 \cdot 0.9\,\mu\text{m} \approx 8 \times 10^{-18}\,\text{F} = 8\,\text{aF}$

From the measurements, we can conclude that this capacitance is sufficient to cause a weak coupling between the dipoles. As soon as the gap disappears, conductive coupling dominates the interaction and capacitive coupling is negligible. For the intermediate capacitances (corresponding to gaps larger than 2 µm) the split is below the resolution of our setup. The largest gap width of 10 µm corresponds to completely decoupled dipoles. In this case, the transmission minima occur at the resonance frequencies f_{0x} and f_{0y}.

3.4 Summary of Results

From the measured data we conclude that the model is applicable to the terahertz range without modifications. The differences between theory and experiment that we discovered are not unique to this range and will also occur at other frequencies.

We could include the dependence of the model's parameters on the physical length L_x in a simple linear model. More detailed measurements are needed to validate this approach.

The unexpected fact that f_{0y} is also influenced by L_x could be explained from basic oscillating circuit theory.

From the gap measurements we concluded that the shape of the structure influences how strong the position of the transmission minima depends on the strength of the coupling σ. The S shape showed the largest σ-dependence.

[1] We are only interested in an order of magnitude estimate, and therefore assume that the conductors are completely surrounded by GaAs. For a better estimate we would have to calculate an effective ε_r to account for the field distribution in GaAs and air.

3.5 Plots

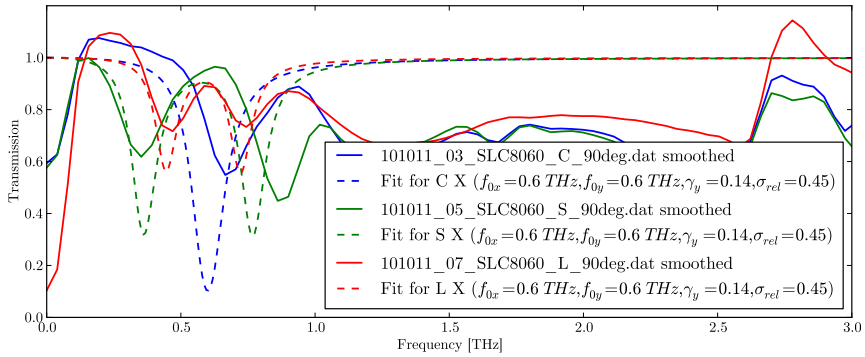

(a) SLC8060 $f_{0x} = 0.6\,\mathrm{THz}$, $f_{0y} = 0.6\,\mathrm{THz}$, $\sigma = 0.45$

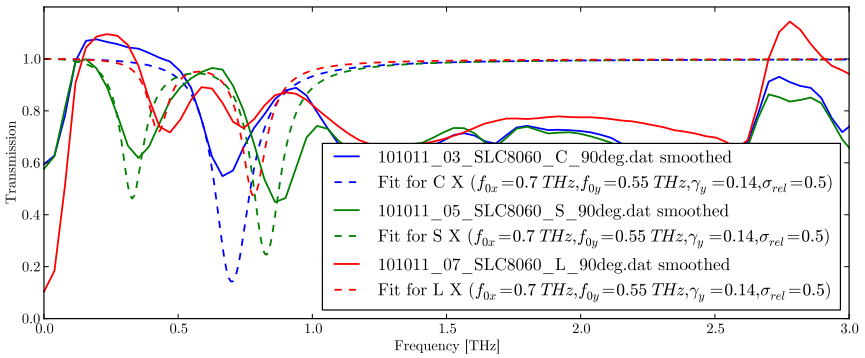

(b) SLC8060 $f_{0x} = 0.7\,\mathrm{THz}$, $f_{0y} = 0.55\,\mathrm{THz}$, $\sigma = 0.5$

Figure 3.7: Comparison of fits for different dipole resonance frequencies f_{0x} and f_{0y} (X polarization). The resonance frequency of the C structure (blue) corresponds to f_{0x} and is better approximated by the second fit.

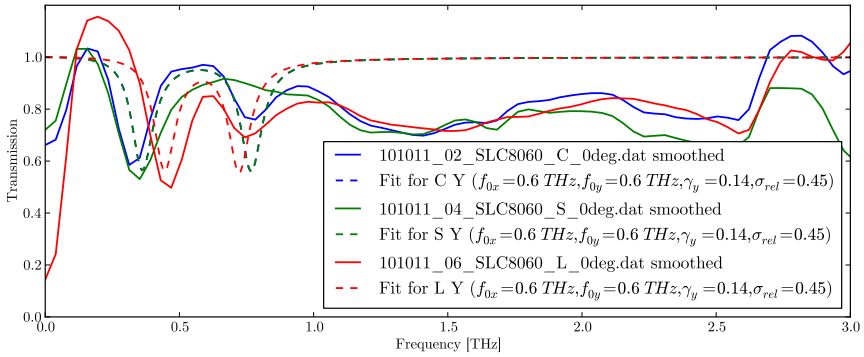

(a) SLC8060 $f_{0x} = 0.6\,\mathrm{THz}$, $f_{0y} = 0.6\,\mathrm{THz}$, $\sigma = 0.45$

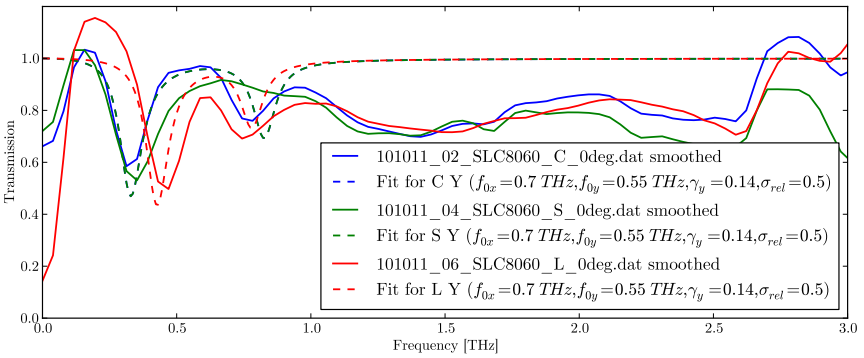

(b) SLC8060 $f_{0x} = 0.7\,\mathrm{THz}$, $f_{0y} = 0.55\,\mathrm{THz}$, $\sigma = 0.5$

Figure 3.8: Comparison of fits for different dipole resonance frequencies f_{0x} and f_{0y} (Y polarization). For the C and S shape, the first set of parameters overestimates the resonance frequency of the lower peak. Furthermore, $f_{0x} = f_{0y}$ leads to a symmetric peak shape in the above fit.

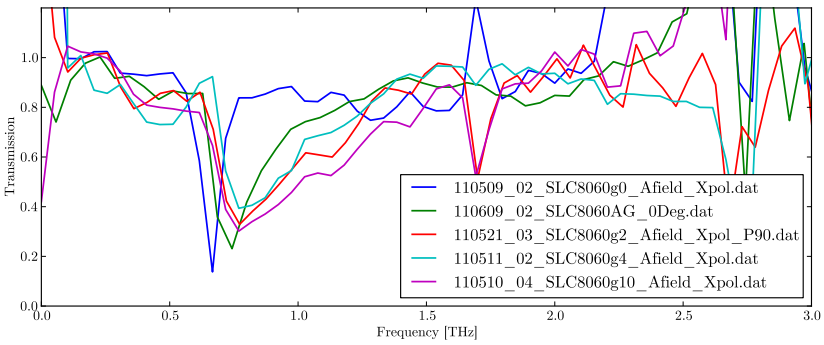

(a) C X

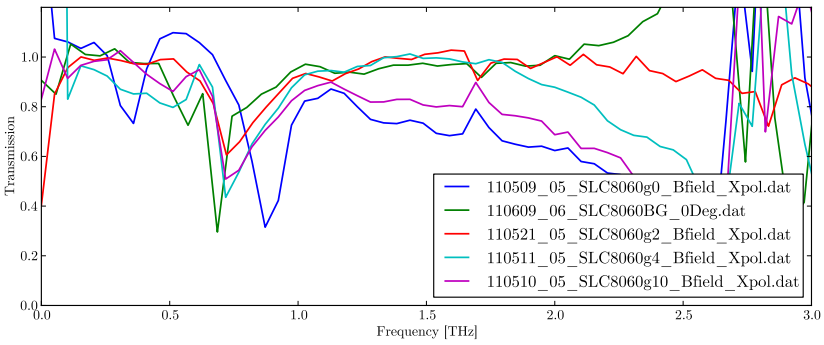

(b) S X

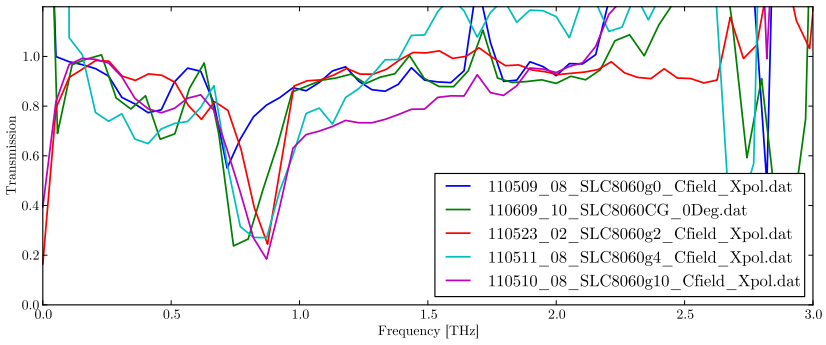

(c) L X

Figure 3.9: Variations of the SLC8060 structure with different gap widths (X polarization). Comparing the structures with increasing gap widths, we see that the lower peak of the S structure vanishes before that of the L structure.

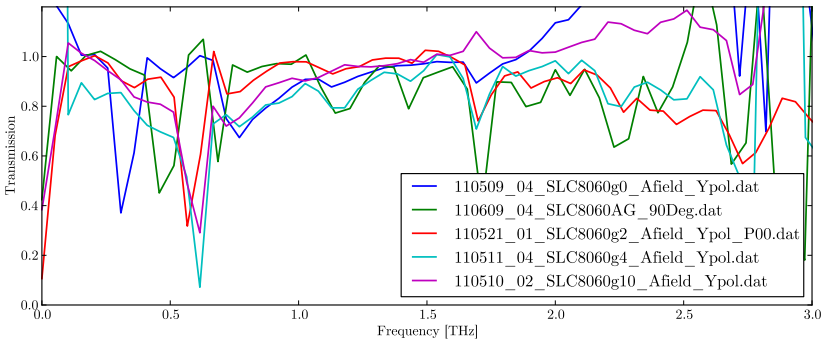

(a) C Y

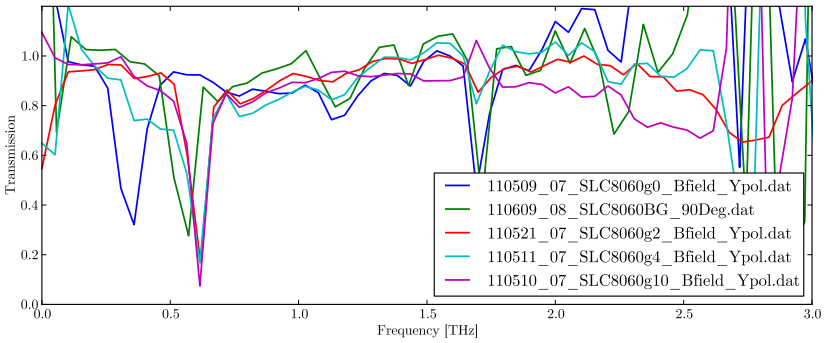

(b) S Y

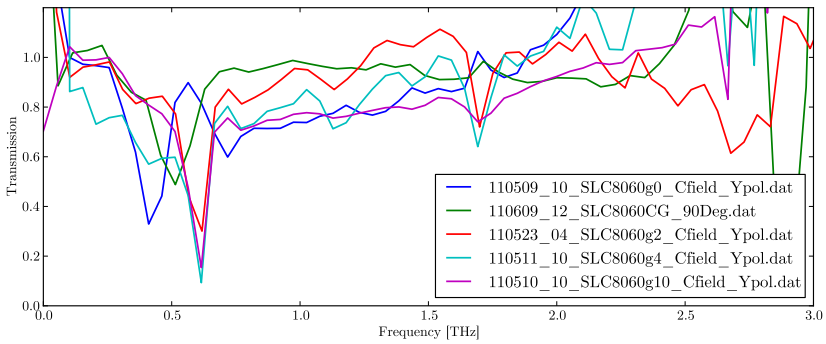

(c) L Y

Figure 3.10: Variations of the SLC8060 structure with different gap widths (Y polarization).

3.6 Software

In the course of this thesis, several utilities were written to facilitate data analysis. They span 54 MATLAB files, containing approximately 2300 lines of code (excluding nearly 500 lines of comments).

Furthermore, a tool to plot the measured data and compare measurements with fits was developed in Python. Together with several utilities that helped create the plots in this thesis, the Python software is contained in 16 files (2000 lines of code and 550 lines of comments).

Data was acquired with an existing LabVIEW program that controlled the motorized stages of the delay line and read out the measurement results from the Lock-In amplifier.

Since this amount of software cannot be adequately presented here, we include only a selected few core components in appendix B.

Python GUI Application

We developed a GUI application to compare measurements with each other as well as with theoretic fits. The tool uses wxPython to create a graphical user interface, matplotlib for plotting and numpy and scipy for numerical calculations.

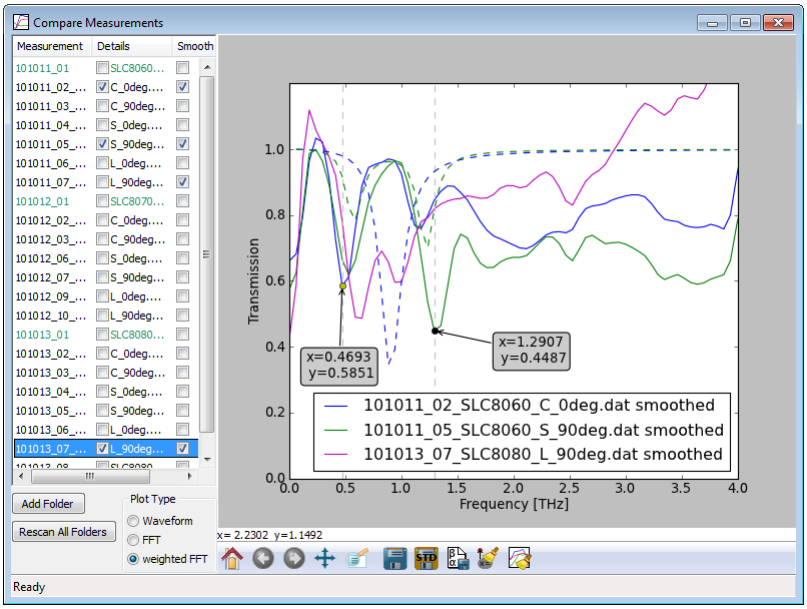

Figure 3.11: Main window of "compareMeasurements", showing three curves of measured data, two fits (dashed lines) and two annotations. The legend entries for the fits were removed to create a clearer picture.

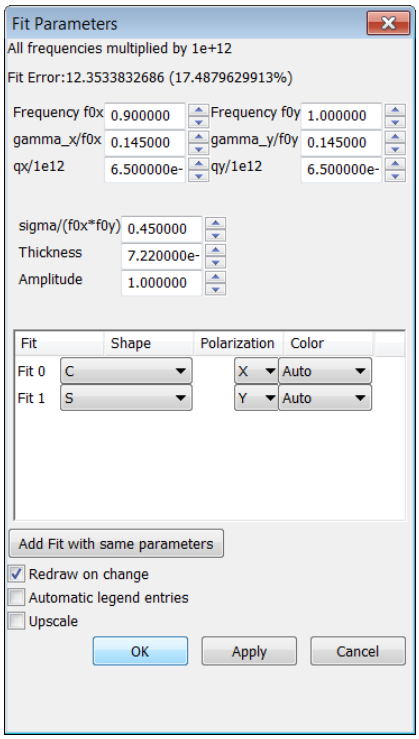

Figure 3.12: Dialog for editing a fit in "compareMeasurements". Multiple fits (two in this screenshot) can share the same set of model variables. This screenshot was taken in Windows 7 using enlarged fonts (150%).

Chapter 4

Conclusion

Traditional numerical approaches like FDTD are a reliable way to simulate metamaterials and their electromagnetic responses, illuminating the question of *how* they work. They can, however, only offer limited clues as to *why* the metamaterial's behavior arises. Our model tries to close this gap.

4.1 Strengths and Weaknesses of the Coupled Dipole Model

The oscillating dipole model is an important extension to the toolkit of the metamaterial researcher and allows new insights into the metamaterial's behavior. We were able to show that the coupled dipole approach is applicable in the terahertz range. By an in-depth study of simple structures, we demonstrated its qualities for prediction and interpretation of transmission measurements.

Since the model is analytical, it can link changes in the transmission signal to changes in the fundamental parameters of the oscillators. Compared to traditional numerical algorithms, this offers a better understanding of the expected behavior. Because it approximates a whole wire by a single oscillator, only a very small system of equations has to be solved. It is therefore orders of magnitude faster than FDTD simulations: the equations are solved in seconds instead of hours.

However, the model assumes that the dipoles do not influence each other apart from a direct coupling. We discovered a deviation from this assumption by varying the length of dipoles, proving that its assumptions are not sufficient. The model neglects many properties of electromagnetic radiation.

While the model works well for simple cases, we also showed that it failed to predict the behavior of more complex ones. The aforementioned deviation may be one reason why large structures, in which additional interactions play a bigger role, cannot be simulated. Other reasons are phase effects, which arise when the the assumption that the structure is smaller than the wavelength is violated.

Furthermore, large structures are composed of more dipoles. Hence, they have an increased number of eigenmodes, some of which have no resulting dipole moment and cannot radiate in the far field. Since our model is based on local dipole interactions, it cannot take the global dipole moment of the structure's resonances into account. Therefore, it systematically overestimates the number of resonances.

The short computation time would make the model a good candidate for combining it with a genetic algorithm to design novel metamaterials. Our hopes for developing new types of meta-atoms were shattered by the cruel hand of reality, due to the aforementioned difficulties modeling large structures.

Extensions

The original model only allowed perpendicular coupling, severely restricting the choice of available shapes. We extended it by introducing longitudinal coupling and transfered it to a hexagonal grid, allowing a wider range of shapes. The long dipoles, which caused troubles on a rectangular grid, do not occur on a hexagonal one.

4.2 Behavior of Grid Based Metamaterials

We proved that the nature of the coupling between dipoles in a grid based metamaterial is almost exclusively conductive. Dipoles separated by a gap larger than 4 µm are decoupled. A weak capacitive coupling can only be observed for small gaps or by artificially increasing the gap capacitance. We therefore concluded that capacitive coupling plays an, albeit limited, role.

From the comparison with our analytical model, we were able to determine the scaling behavior of the different parameters. While some parameters scaled as expected, others showed counterintuitive effects. We showed that these effects can be explained using basic electromagnetic theories.

4.3 Further Work

There are several interesting extensions to our model which could not be pursued in the course of this thesis.

A promising approach to the problem of large structures lies in replacing the dipole equations of our model with more complex ones. A suitable candidate would be magneto-hydrodynamic equations. This could increase the descriptive power of our model with only a modest increase in complexity.

Increasing the complexity of the model, however, offers diminishing returns. The model is only useful as long as it stays faster and simpler than the numerical alternatives. As soon as run-times are comparable, the more mature algorithms are at an advantage.

Bibliography

Bastard, G. (2012). Quantum physics in the solid state. Guest lecture.

Beech, M. (2012). The metamaterial revolution. In *The Physics of Invisibility*, pages 131–187. Springer New York.

Bockelmann, U. and Bastard, G. (1990). Phonon scattering and energy relaxation in two-, one-, and zero-dimensional electron gases. *Phys. Rev. B*, 42:8947–8951.

Bondeson, A., Rylander, T., and Ingelström, P. (2005). *Computational electromagnetics*. Texts in applied mathematics. Springer.

Born, M. and Wolf, E. (1999). *Principles of Optics: Electromagnetic Theory of Propagation, Interference and Diffraction of Light*. Cambridge University Press, 7th (expanded) edition.

Bossard, J. A., Yun, S., Werner, D. H., and Mayer, T. S. (2009). Synthesizing low loss negative index metamaterial stacks for the mid-infrared using genetic algorithms. *Opt. Express*, 17(17):14771–14779.

Cai, W., Chettiar, U. K., Kildishev, A. V., and Shalaev, V. M. (2007). Optical cloaking with metamaterials. *Nature Photonics*, 1:224,227.

Capolino, F. (2009). *Theory and Phenomena of Metamaterials*. Metamaterials handbook. CRC Press/Taylor & Francis.

Carr, G. L., Martin, M. C., McKinney, W. R., Jordan, K., Neil, G. R., and Williams, G. P. (2002). High-power terahertz radiation from relativistic electrons. *Nature*, 420:153 – 156.

Chen, H., Chan, C. T., and Sheng, P. (2010). Transformation optics and metamaterials. *Nature Materials*, 9:387 – 396.

Chen, P. Y., Chen, C. H., Wang, H., Tsai, J. H., and Ni, W. X. (2008). Synthesis design of artificial magnetic metamaterials using a genetic algorithm. *Opt. Express*, 16(17):12806 – 12818.

Choi, M., Lee, S. H., Kim, Y., Kang, S. B., Shin, J., Kwak, M. H., Kang, K.-Y., Lee, Y.-H., Park, N., and Min, B. (2011). A terahertz metamaterial with unnaturally high refractive index. *Nature*, 470:369 – 373.

Collin, R., Antennas, I., and Society, P. (1991). *Field theory of guided waves*. The IEEE/OUP Series on Electromagnetic Wave Theory (Formerly IEEE Only), Series Editor Series. IEEE Press.

Darmo, J. (2010). COMSOL calculations. Priv. comm.

Davidson, D. (2005). *Computational Electromagnetics for RF and Microwave Engineering*. Cambridge University Press. The recent second edition was published in 2010.

Dietze, D. (2010). Custom FDTD solver. Priv. comm.

Ergin, T., Stenger, N., Brenner, P., Pendry, J. B., and Wegener, M. (2010). Three-dimensional invisibility cloak at optical wavelengths. *Science*, 328(5976):337 – 339.

Faist, J., Capasso, F., Sivco, D. L., Sirtori, C., Hutchinson, A. L., and Cho, A. Y. (1994). Quantum cascade laser. *Science*, 264(5158):553 – 556.

Ferreira, R. and Bastard, G. (1989). Evaluation of some scattering times for electrons in unbiased and biased single- and multiple-quantum-well structures. *Phys. Rev. B*, 40:1074 – 1086.

Feth, N., König, M., Husnik, M., Stannigel, K., Niegemann, J., Busch, K., Wegener, M., and Linden, S. (2010). Electromagnetic interaction of split-ring resonators: The role of separation and relative orientation. *Opt. Express*, 18(7):6545 – 6554.

Gabrielli, L. H., Cardenas, J., Poitras, C. B., and Lipson, M. (2009). Silicon nanostructure cloak operating at optical frequencies. *Nature Photonics*, 3:461 – 463.

Gao, M., Shi, Z.-c., Fan, R.-h., Qian, L., Zhang, Z.-d., and Guo, J.-y. (2012). High-frequency negative permittivity from Fe/Al2O3 composites with high metal contents. *Journal of the American Ceramic Society*, 95(1):67 – 70.

Gay-Balmaz, P. and Martin, O. J. F. (2002). Electromagnetic resonances in individual and coupled split-ring resonators. *Journal of Applied Physics*, 92(5):2929 – 2936.

Gingrich, M. and Werner, D. (2005). Synthesis of low/zero index of refraction metamaterials from frequency selective surfaces using genetic algorithms. *Electronics Letters*, 41(23):1266 – 1267.

ITU, I. T. U. (2008). Radio regulations, volume 1, article 2. An online version is available at `http://life.itu.int/radioclub/rr/art02.htm`. Visited on January 12th 2012.

Jackson, J. D. (1998). *Classical Electrodynamics*. Wiley, 3rd edition.

Jeong, Y., Kazakevich, G., Park, S., Lee, K., Lee, B., Cha, Y.-H., Ahn, P., and Mun, J. (2009). High power table-top thz free electron laser and its application. In *Infrared, Millimeter, and Terahertz Waves, 2009. IRMMW-THz 2009. 34th International Conference on*, pages 1 – 2.

Kock, W. E. (1946). Metal-lens antennas. *Proceedings of the IRE*, 34(11):828 – 836.

Kock, W. E. (1948). Metallic delay lenses. *Bell System Technical Journal*, 27:58 – 82. Available on-line at `http://www.alcatel-lucent.com/bstj/vol27-1948/articles/bstj27-1-58.pdf`. The complete archive of the journal is freely accessible at `http://www.alcatel-lucent.com/bstj/`.

Lee, Y.-S. (2008). *Principles of Terahertz Science and Technology*. Springer.

Leisawitz, D. T., Danchi, W. C., DiPirro, M. J., Feinberg, L. D., Y., G. D., Hagopian, M., Langer, W. D., Mather, J. C., Moseley Jr., S. H., Shao, M., Silverberg, R. F., Staguhn, J. G., Swain, M. R., Yorke, H. W., and Zhang, X. (2000). Terahertz technology. *Proceedings of SPIE*, 4013(3):36 – 46.

Leonhardt, U. (2003). Notes on waves with negative phase velocity. *Selected Topics in Quantum Electronics, IEEE Journal of*, 9(1):102 – 105.

Leonhardt, U. (2006). Optical conformal mapping. *Science*, 312(5781):1777 – 1780.

Leonhardt, U. (2011). Geometry, light and a wee bit of magic. CoQus Colloquium lecture.

Li, J., Nam, K. B., Nakarmi, M. L., Lin, J. Y., Jiang, H. X., Carrier, P., and Wei, S.-H. (2003). Band structure and fundamental optical transitions in wurtzite AlN. *Applied Physics Letters*, 83(25):5163 – 5165.

Marqués, R., Martín, F., and Sorolla, M. (2011). *Metamaterials with Negative Parameters: Theory, Design and Microwave Applications*. Wiley Series in Microwave and Optical Engineering. John Wiley & Sons.

Michalewicz, Z. (1996). *Genetic algorithms + data structures*. Artificial intelligence. Springer.

Nicolson, A. M. and Ross, G. F. (1970). Measurement of the intrinsic properties of materials by time-domain techniques. *Instrumentation and Measurement, IEEE Transactions on*, 19(4):377 – 382.

Pendry, J., Holden, A., Robbins, D., and Stewart, W. (1999). Magnetism from conductors and enhanced nonlinear phenomena. *Microwave Theory and Techniques, IEEE Transactions on*, 47(11):2075 – 2084.

Pendry, J. B. (2000). Negative refraction makes a perfect lens. *Phys. Rev. Lett.*, 85:3966 – 3969.

Pendry, J. B., Holden, A. J., Robbins, D. J., and Stewart, W. J. (1998). Low frequency plasmons in thin-wire structures. *Journal of Physics: Condensed Matter*, 10(22):4785.

Pendry, J. B., Holden, A. J., Stewart, W. J., and Youngs, I. (1996). Extremely low frequency plasmons in metallic mesostructures. *Phys. Rev. Lett.*, 76:4773 – 4776.

Pendry, J. B., Schurig, D., and Smith, D. R. (2006). Controlling electromagnetic fields. *Science*, 312(5781):1780 – 1782.

Petschulat, J., Chipouline, A., Tünnermann, A., Pertsch, T., Menzel, C., Rockstuhl, C., Paul, T., and Lederer, F. (2010). Simple and versatile analytical approach for planar metamaterials. *Phys. Rev. B*, 82(7):075102.

Planck, M. (1901). Ueber das Gesetz der Energieverteilung im Normalspectrum. *Annalen der Physik*, 309:553 – 563. Available online at `http://www.physik.uni-augsburg.de/annalen/history/historic-papers/1901_309_553-563.pdf`. Visited on January 12th 2012.

Press, W. (1992). *Numerical recipes in C: the art of scientific computing*. Cambridge University Press, 2nd edition.

Rothman, L., Gordon, I., Barbe, A., Benner, D., Bernath, P., Birk, M., Boudon, V., Brown, L., Campargue, A., Champion, J.-P., Chance, K., Coudert, L., Dana, V., Devi, V., Fally, S., Flaud, J.-M., Gamache, R., Goldman, A., Jacquemart, D., Kleiner, I., Lacome, N., Lafferty, W., Mandin, J.-Y., Massie, S., Mikhailenko, S., Miller, C., Moazzen-Ahmadi, N., Naumenko, O., Nikitin, A., Orphal, J., Perevalov, V., Perrin, A., Predoi-Cross, A., Rinsland, C., Rotger, M., Šimečková, M., Smith, M., Sung, K., Tashkun, S., Tennyson, J., Toth, R., Vandaele, A., and Auwera, J. V. (2009). The HITRAN 2008 molecular spectroscopic database. *Journal of Quantitative Spectroscopy and Radiative Transfer*, 110(9 – 10):533 – 572. HITRAN data is available at `http://hitran.iao.ru/gasmixture` and `http://www.spectralcalc.com/atmospheric_paths/paths.php`.

Sakai, K. (2005). *Terahertz optoelectronics*. Topics in applied physics. Springer.

Schurig, D., Mock, J. J., Justice, B. J., Cummer, S. A., Pendry, J. B., Starr, A. F., and Smith, D. R. (2006). Metamaterial electromagnetic cloak at microwave frequencies. *Science*, 314(5801):977 – 980.

Shelby, R. A., Smith, D. R., and Schultz, S. (2001). Experimental verification of a negative index of refraction. *Science*, 292(5514):77 – 79.

Sherwin, M. (2002). Applied physics: Terahertz power. *Nature*, 420:131 – 133.

Siegel, P. (2002). Terahertz technology. *Microwave Theory and Techniques, IEEE Transactions on*, 50(3):910 – 928.

Singh, R., Rockstuhl, C., and Zhang, W. (2010). Strong influence of packing density in terahertz metamaterials. *Applied Physics Letters*, 97(24):241108.

Smith, D. R., Padilla, W. J., Vier, D. C., Nemat-Nasser, S. C., and Schultz, S. (2000). Composite medium with simultaneously negative permeability and permittivity. *Phys. Rev. Lett.*, 84(18):4184 – 4187.

Smith, D. R., Schultz, S., Markoš, P., and Soukoulis, C. M. (2002). Determination of effective permittivity and permeability of metamaterials from reflection and transmission coefficients. *Phys. Rev. B*, 65:195104.

Streetman, B. G. and Banerjee, S. (2000). *Solid state electronic devices*. Solid state physical electronics series. Prentice Hall, 4th edition.

Sze, S. M. (1981). *Physics of Semiconductor Devices*. Wiley-Interscience, 2nd edition.

Taflove, A. and Hagness, S. (2000). *Computational electrodynamics: the finite-difference time-domain method*. Artech House antennas and propagation library. Artech House, 2nd edition. The recent third edition was published in 2005.

Veselago, V. G. (1968). The electrodynamics of substances with simultaneously negative values of ϵ and μ. *Soviet Physics Uspekhi*, 10(4):509.

Weile, D. and Michielssen, E. (1997). Genetic algorithm optimization applied to electromagnetics: a review. *Antennas and Propagation, IEEE Transactions on*, 45(3):343 – 353.

Weir, W. (1974). Automatic measurement of complex dielectric constant and permeability at microwave frequencies. *Proceedings of the IEEE*, 62(1):33 – 36.

Weisstein, E. W. (2004). Fourier transform. From MathWorld – A Wolfram Web Resource. `http://mathworld.wolfram.com/FourierTransform.html` Visited on December 12th 2011.

Yee, K. (1966). Numerical solution of initial boundary value problems involving maxwell's equations in isotropic media. *Antennas and Propagation, IEEE Transactions on*, 14(3):302 – 307.

Ziolkowski, R. W. (2003). Pulsed and cw gaussian beam interactions with double negative metamaterial slabs. *Opt. Express*, 11(7):662 – 681.

Ziolkowski, R. W. (2005). Antennas and propagation in the presence of metamaterials and other complex media: Computational electromagnetic advances and challenges. *IEICE Transactions*, 88-B(6):2230 – 2238. Available online at: `http://www2.engr.arizona.edu/~ziolkows/research/papers/Metamaterial_Research/Antennas/Ziolkowski_IEICE_June_2005.pdf`.

Appendix A

Additional Equations

A.1 Fourier Transform of Differential Equations

Mathematical Definition

In mathematics, the Fourier transform and its inverse are usually defined as [Weisstein, 2004]

$$F(f) = \int_{-\infty}^{\infty} f(t) e^{-i2\pi ft} dt, \tag{A.1.1}$$

$$f(t) = \int_{-\infty}^{\infty} F(f) e^{i2\pi ft} df. \tag{A.1.2}$$

It maps a derivative in real space $\left(\frac{\partial x}{\partial t} = \dot{x}\right)$ to a multiplication in frequency space. Because of the integration over e^x, differential operators become linear. This is described by the relations [Weisstein, 2004, eqs.(34)–(44)]

$$F\left[f(t)'\right] = 2\pi i f F(f(t)), \tag{A.1.3}$$

$$F\left[f(t)''\right] = (2\pi i f)^2 F(f(t)) = -(2\pi f)^2 F(f(t)), \tag{A.1.4}$$

$$F\left[f(t)^{(n)}\right] = (2\pi i f)^n F(f(t)). \tag{A.1.5}$$

Applying this to the equation of motion (2.2.7)

$$\ddot{x}_1 + \omega_{01}^2 x_1 + \gamma_1 \dot{x}_1 = \frac{q_1}{m_1} E_1, \tag{A.1.6}$$

leads to

$$-(2\pi f)^2 x_1 + \omega_{01}^2 x_1 + (2\pi i f)\gamma_1 x_1 = \frac{q_1}{m_1} E_1, \tag{A.1.7}$$

$$\left[\omega_{01}^2 - (2\pi f)^2 + (2\pi i f)\gamma_1\right] x_1 = \frac{q_1}{m_1} E_1. \tag{A.1.8}$$

Another common definition of the Fourier Transform uses the angular frequency $\omega = 2\pi f$

$$F(\omega) = \int_{-\infty}^{\infty} f(t) e^{-i\omega t} dt, \tag{A.1.9}$$

$$f(t) = \frac{1}{2\pi} \int_{-\infty}^{\infty} F(\omega) e^{i\omega t} d\omega. \tag{A.1.10}$$

Alternative Definition

Petschulat et al. seem to use yet another variant (note the sign in the exponent)

$$F(\omega) = \int_{-\infty}^{\infty} f(t) e^{i\omega t} dt, \tag{A.1.11}$$

$$f(t) = \frac{1}{2\pi} \int_{-\infty}^{\infty} F(\omega) e^{-i\omega t} d\omega. \tag{A.1.12}$$

If this alternative definition of the Fourier transform is used, the relations shown earlier have different signs

$$F\left[f(t)'\right] = -i\omega F(f(t)), \tag{A.1.13}$$

$$F\left[f(t)''\right] = (-\omega i f)^2 F(f(t)) = -\omega^2 F(f(t)), \tag{A.1.14}$$

$$F\left[f(t)^{(n)}\right] = (-i\omega)^n F(f(t)). \tag{A.1.15}$$

This also leads to a sign change in the equation of motion

$$\left[\omega_{01}^2 - (2\pi f)^2 - (2\pi i f)\gamma_1\right] x_1 = \frac{q_1}{m_1} E_1, \tag{A.1.16}$$

$$\left[\omega_{01}^2 - \omega^2 + \omega\gamma_1\right] x_1 = \frac{q_1}{m_1} E_1, \tag{A.1.17}$$

which is equivalent to [Petschulat et al., 2010, eq.(5)].

This choice of signs is conventionally used to describe harmonic oscillators – such as the equation of motion in the Lorentz model (1.5.4).

Comparing the two equations of motion (A.1.8) and (A.1.17) shows that the usual mathematical definition leads to unphysical behavior, namely an increase in transmission above 1. We therefore need to use the second variant.

A.2 Electric Permittivity

The electric permittivity ε_r is the proportionality factor introduced to link the electric displacement $\vec{D}$ and the electrical field $\vec{E}$[1]

$$\vec{D} = \varepsilon_r \vec{E}. \tag{A.2.1}$$

[1]This section follows the explanations given in [Jackson, 1998, ch.4.3, p.153–154, eq.(4.34)–(4.38)]. Jackson uses χ_e instead of χ and ϵ instead of ε_r.

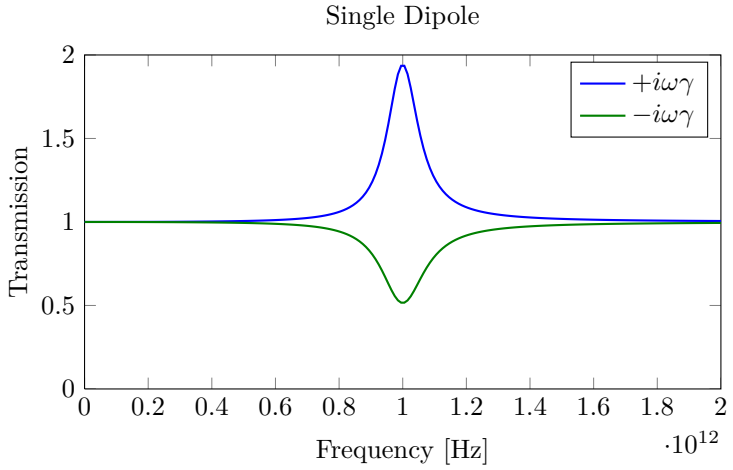

Figure A.1: Different variations of the Fourier transform result in different signs of the dampening term $i\omega\gamma$. The positive sign is an unphysical result.

The displacement is defined as

$$\vec{D} = \varepsilon_0 \vec{E} + \vec{P}. \tag{A.2.2}$$

The polarization $\vec{P}$ is assumed to be isotropic and a linear relation to $\vec{E}$ is postulated, introducing the permittivity

$$\vec{P} = \varepsilon_0 \chi \vec{E}. \tag{A.2.3}$$

Combining these assumptions leads to

$$\varepsilon_r = \varepsilon_0 \left(1 + \chi\right). \tag{A.2.4}$$

A.3 Tailor Expansion of the Dipole Interaction

The force F_{dipole} between these two dipoles can be approximated by a Taylor series around the equilibrium distance r_0

$$\begin{aligned} \frac{1}{r^2}\bigg|_{r=r_0} &= \sum_{n=0}^{\infty} \frac{f^{(n)}(r_0)}{n!} \left(r - r_0\right)^n \\ &= \frac{1}{r_0^2} + \frac{-2/r_0^3}{1} \left(r - r_0\right) + \frac{6/r_0^4}{2} \left(r - r_0\right)^2 + \cdots . \end{aligned} \tag{A.3.1}$$

For a first order approximation, we only collect the terms up to $O(r)$

$$\frac{1}{r^2}\bigg|_{r=r_0} \approx \frac{1}{r_0^2} - \frac{2r}{r_0^3} + \frac{2r_0}{r_0^3} - \frac{6rr_0}{r_0^4} + \frac{3r_0^2}{r_0^4} = \frac{6}{r_0^2} - \frac{8r}{r_0^3}. \tag{A.3.2}$$

With this expansion, we obtain

$$F_d\,(r - r_0) \approx \frac{q_1 q_2}{4\pi\varepsilon_0\varepsilon_r}\left[\frac{6}{r_0^2} - \frac{8r}{r_0^3}\right]. \tag{A.3.3}$$

The first term in the square brackets is independent of r. It only causes a constant offset that can be omitted, since it is irrelevant for the dynamics of the system. We therefore get

$$F_d\,(r - r_0) \approx -\frac{q_1 q_2}{4\pi\varepsilon_0\varepsilon_r}\frac{8}{r_0^3}r = -\sigma r = -\sigma(x_1 - x_2). \tag{A.3.4}$$

A.4 Coupling Matrices for Petschulat Shapes

In this section, we will demonstrate the steps of the algorithm that was outlined in section 2.5. To validate our approach we take two of the shapes from [Petschulat et al., 2010] and show that our algorithm yields the same results.

Example - S-shape

As an example, let us look at the vector $(0, 1, 0, 0, 1, 0, 1, 0, 0)$ (see figure 2.6). The resulting equations are

$$\frac{1}{m}\begin{pmatrix} 0 \\ q_xE_x \\ 0 \\ 0 \\ q_yE_y \\ 0 \\ q_xE_x \\ 0 \\ 0 \end{pmatrix} = \begin{pmatrix} 0 & 0 & 0 & 0 & 0 & 0 & 0 & 0 & 0 \\ 0 & A_x & 0 & 0 & \sigma & 0 & 0 & 0 & 0 \\ 0 & 0 & 0 & 0 & 0 & 0 & 0 & 0 & 0 \\ 0 & 0 & 0 & 0 & 0 & 0 & 0 & 0 & 0 \\ 0 & \sigma & 0 & 0 & A_y & 0 & \sigma & 0 & 0 \\ 0 & 0 & 0 & 0 & 0 & 0 & 0 & 0 & 0 \\ 0 & 0 & 0 & 0 & \sigma & 0 & A_x & 0 & 0 \\ 0 & 0 & 0 & 0 & 0 & 0 & 0 & 0 & 0 \\ 0 & 0 & 0 & 0 & 0 & 0 & 0 & 0 & 0 \end{pmatrix} \begin{pmatrix} x_1 \\ x_2 \\ x_3 \\ y_1 \\ y_2 \\ y_3 \\ x_4 \\ x_5 \\ x_6 \end{pmatrix}. \tag{A.4.1}$$

Removing empty rows and columns leads to the equivalent system

$$\frac{1}{m}\begin{pmatrix} q_xE_x \\ q_yE_y \\ q_xE_x \end{pmatrix} = \begin{pmatrix} A_x & \sigma & 0 \\ \sigma & A_y & \sigma \\ 0 & \sigma & A_x \end{pmatrix} \begin{pmatrix} x_2 \\ y_2 \\ x_4 \end{pmatrix}. \tag{A.4.2}$$

The inverse of M is

$$\frac{1}{A_xA_y - 2\sigma^2}\begin{pmatrix} A_y - {\sigma^2}/{A_x} & -\sigma & {\sigma^2}/{A_x} \\ -\sigma & A_x & -\sigma \\ {\sigma^2}/{A_x} & -\sigma & A_y - {\sigma^2}/{A_x} \end{pmatrix}, \tag{A.4.3}$$

leading to the solutions

$$x_2 = x_4 = \frac{1}{m}\frac{A_yq_xE_x - \sigma q_yE_y}{A_xA_y - 2\sigma^2}, \qquad y_2 = \frac{1}{m}\frac{A_xq_yE_y - 2\sigma q_xE_x}{A_xA_y - 2\sigma^2}. \tag{A.4.4}$$

This leads to

$$\chi = \frac{\eta}{m\varepsilon_0}\frac{1}{A_xA_y - 2\sigma^2}\begin{pmatrix} 2A_yq_x^2 & 2\sigma q_xq_y \\ 2\sigma q_xq_y & A_xq_y^2 \end{pmatrix}, \tag{A.4.5}$$

which is the same result as [Petschulat et al., 2010, eq. (11)].

Example - C-shape

The C Shape is defined by $(1,0,0,1,0,0,1,0,0)$, resulting in the system of equations

$$\frac{1}{m}\begin{pmatrix} q_xE_x \\ 0 \\ 0 \\ q_yE_y \\ 0 \\ 0 \\ q_xE_x \\ 0 \\ 0 \end{pmatrix} = \begin{pmatrix} A_x & 0 & 0 & \sigma & 0 & 0 & 0 & 0 & 0 \\ 0 & 0 & 0 & 0 & 0 & 0 & 0 & 0 & 0 \\ 0 & 0 & 0 & 0 & 0 & 0 & 0 & 0 & 0 \\ \sigma & 0 & 0 & A_y & 0 & 0 & -\sigma & 0 & 0 \\ 0 & 0 & 0 & 0 & 0 & 0 & 0 & 0 & 0 \\ 0 & 0 & 0 & 0 & 0 & 0 & 0 & 0 & 0 \\ 0 & 0 & 0 & -\sigma & 0 & 0 & A_x & 0 & 0 \\ 0 & 0 & 0 & 0 & 0 & 0 & 0 & 0 & 0 \\ 0 & 0 & 0 & 0 & 0 & 0 & 0 & 0 & 0 \end{pmatrix}\begin{pmatrix} x_1 \\ x_2 \\ x_3 \\ y_1 \\ y_2 \\ y_3 \\ x_4 \\ x_5 \\ x_6 \end{pmatrix}. \tag{A.4.6}$$

Removing empty rows and columns leads to the equivalent system

$$\frac{1}{m}\begin{pmatrix} q_xE_x \\ q_yE_y \\ q_xE_x \end{pmatrix} = \begin{pmatrix} A_x & \sigma & 0 \\ \sigma & A_y & -\sigma \\ 0 & -\sigma & A_x \end{pmatrix}\begin{pmatrix} x_1 \\ y_1 \\ x_4 \end{pmatrix}. \tag{A.4.7}$$

The inverse of M is

$$\frac{1}{A_xA_y - 2\sigma^2}\begin{pmatrix} A_y - {\sigma^2}/{A_x} & -\sigma & -{\sigma^2}/{A_x} \\ -\sigma & A_x & \sigma \\ -{\sigma^2}/{A_x} & \sigma & A_y - {\sigma^2}/{A_x} \end{pmatrix}, \tag{A.4.8}$$

leading to the solutions

$$x_1 = \frac{q_xE_x}{mA_x} - \frac{1}{m}\frac{\sigma q_yE_y}{A_xA_y - 2\sigma^2}, \qquad y_1 = \frac{1}{m}\frac{A_xq_yE_y}{A_xA_y - 2\sigma^2}, \tag{A.4.9}$$

$$x_4 = \frac{q_xE_x}{mA_x} + \frac{1}{m}\frac{\sigma q_yE_y}{A_xA_y - 2\sigma^2}. \tag{A.4.10}$$

This leads to

$$\chi = \frac{\eta}{m\varepsilon_0}\begin{pmatrix} {2q_x^2}/{A_x} & 0 \\ 0 & {A_xq_y^2}/{A_xA_y - 2\sigma^2} \end{pmatrix}, \tag{A.4.11}$$

which is equivalent to [Petschulat et al., 2010, eq. (7)].

A.5 Longitudinally Coupled Dipoles

Single Dipole

$$M = (A_x)\,, \qquad X = \frac{E_x}{A_x}, \qquad \chi = \frac{1}{A_x}. \tag{A.5.1}$$

This results in the eigenfrequency

$$\omega_{1/2} = \frac{i\gamma}{2} \pm \sqrt{-\frac{\gamma^2}{4} + \omega_0^2}. \tag{A.5.2}$$

Two Dipoles

$$M = \begin{pmatrix} A_x & \tau \\ \tau & A_x \end{pmatrix}, \qquad X = \frac{E_x}{\tau + A_x}\begin{pmatrix} 1 \\ 1 \end{pmatrix}, \tag{A.5.3}$$

$$\det(M) = A_x^2 - \tau^2, \qquad \chi = \frac{2}{A_x + \tau}. \tag{A.5.4}$$

Solving the equation $\det(M - \lambda\mathbb{1}) = (A_x - \lambda)^2 - \tau^2 = 0$, one obtains the eigenfrequencies of the dipoles

$$\omega_{1-4} = \frac{i\gamma}{2} \pm \sqrt{-\frac{\gamma^2}{4} + \omega_0^2 \pm \tau}. \tag{A.5.5}$$

Looking only at the positive frequencies for the lossless case ($\gamma = 0$), one obtains

$$\omega_1 = \sqrt{\omega_0^2 + \tau}, \tag{A.5.6}$$

$$\omega_3 = \sqrt{\omega_0^2 - \tau}. \tag{A.5.7}$$

Three Dipoles

$$M = \begin{pmatrix} A_x & \tau & 0 \\ \tau & A_x & \tau \\ 0 & \tau & A_x \end{pmatrix}, \qquad X = \frac{E_x}{A_x^2 - 2\tau^2}, \begin{pmatrix} A_x - \tau \\ A_x - 2\tau \\ A_x - \tau \end{pmatrix}, \tag{A.5.8}$$

$$\det(M) = A_x^3 - 2A_x\tau^2, \qquad \chi = \frac{3A_x - 4\tau}{A_x^2 - 2\tau^2}. \tag{A.5.9}$$

the eigenfrequencies are obtained by solving $\det(M - \lambda\mathbb{1}) = 0$, resulting in

$$\omega_{1-4} = \frac{i\gamma}{2} \pm \sqrt{\frac{-\gamma^2}{4} + \omega_0^2 \pm \sqrt{2}\tau}, \tag{A.5.10}$$

$$\omega_{5/6} = \frac{i\gamma}{2} \pm \sqrt{\frac{-\gamma^2}{4} + \omega_0^2}. \tag{A.5.11}$$

For positive frequencies in the lossless, case using $\tau = \frac{3\omega_0^2}{4}$ leads to

$$\omega_1 = \sqrt{\omega_0^2 + \sqrt{2}\tau} = \frac{\sqrt{4+\sqrt{18}}}{2}\omega_0, \tag{A.5.12}$$

$$\omega_3 = \sqrt{\omega_0^2 - \sqrt{2}\tau} = \frac{\sqrt{4-\sqrt{18}}}{2}\omega_0 \quad \in \mathbb{C}, \tag{A.5.13}$$

$$\omega_5 = \omega_0. \tag{A.5.14}$$

Modifying the coupling matrix to allow coupling over long distances leads to

$$M = \begin{pmatrix} A_x & \tau & \tau \\ \tau & A_x & \tau \\ \tau & \tau & A_x \end{pmatrix}, \qquad X = \frac{E_x}{A_x + 2\tau}\begin{pmatrix} 1 \\ 1 \\ 1 \end{pmatrix}, \tag{A.5.15}$$

$$\det(M) = A_x^3 - 3A_x\tau^2 + 2\tau^3, \qquad \chi = \frac{1}{A_x + 2\tau}. \tag{A.5.16}$$

In this case the eigenfrequencies are

$$\omega_{1/2} = \frac{i\gamma}{2} \pm \sqrt{\frac{-\gamma^2}{4} + \omega_0^2 + 2\tau}, \tag{A.5.17}$$

$$\omega_{3-6} = \frac{i\gamma}{2} \pm \sqrt{\frac{-\gamma^2}{4} + \omega_0^2 - \tau}. \tag{A.5.18}$$

Again, we look at the positive frequencies in the lossless case and use the value for τ that we obtained from the equations of two dipoles ($\tau = \frac{3\omega_0^2}{4}$, see section 2.4). This leads to

$$\omega_1 = \sqrt{\omega_0^2 + 2\tau} = \frac{\sqrt{10}\omega_0}{2}, \tag{A.5.19}$$

$$\omega_3 = \omega_5 = \sqrt{\omega_0^2 - \tau} = \frac{\omega_0}{2}. \tag{A.5.20}$$

A.6 Permittivity of Basic Hexagonal Shapes

In this section, we derive the analytical equations for hexagonal shapes. This can be used to predict the response of metamaterials.

Equation of Motion

The basic elements are described by linear equations obtained by Fourier transformation of the equation of motion. With the same procedure that was used in section 2.2 we get a system of coupled differential equations. We will reuse the coupling parameter σ. Since the dipoles are no longer perpendicular, we expect a different value for $\sigma_{hexagonal} \neq \sigma_{rectangular}$.

As an example we examine the Fourier transformation of

$$\ddot{x}_1 + \gamma_x \dot{x}_1 + \omega_{0x}^2 x_1 + \sigma\xi_2 + \sigma\zeta_3 = \frac{q_x}{m} E_x, \tag{A.6.1}$$

$$\ddot{\xi}_2 + \gamma_\xi \dot{\xi}_2 + \omega_{0\xi}^2 \xi_2 + \sigma x_1 + \sigma\zeta_3 = \frac{q_\xi}{m} E_\xi, \tag{A.6.2}$$

$$\ddot{\zeta}_3 + \gamma_\zeta \dot{\zeta}_3 + \omega_{0\zeta}^2 \zeta_3 + \sigma x_1 + \sigma\xi_2 = \frac{q_\zeta}{m} E_\zeta, \tag{A.6.3}$$

which yields

$$\left(\omega_{0x}^2 - \omega^2 + i\gamma_x\omega\right) x_1 + \sigma\xi_2 + \sigma\zeta_3 = \frac{q_x}{m} E_x, \tag{A.6.4}$$

$$\left(\omega_{0\xi}^2 - \omega^2 + i\gamma_\xi\omega\right) \xi_2 + \sigma x_1 + \sigma\zeta_3 = \frac{q_\xi}{m} E_\xi, \tag{A.6.5}$$

$$\left(\omega_{0\zeta}^2 - \omega^2 + i\gamma_\zeta\omega\right) \zeta_3 + \sigma x_1 + \sigma\xi_2 = \frac{q_\zeta}{m} E_\zeta. \tag{A.6.6}$$

To further simplify these equations we introduce

$$A_x = \left(\omega_{0x}^2 - \omega^2 + i\gamma\right), \tag{A.6.7}$$

$$A_\xi = \left(\omega_{0\xi}^2 - \omega^2 + i\gamma\right), \tag{A.6.8}$$

$$A_\zeta = \left(\omega_{0\zeta}^2 - \omega^2 + i\gamma\right) \tag{A.6.9}$$

and write the equations in matrix form

$$\begin{pmatrix} A_x & \sigma & \sigma \\ \sigma & A_\xi & \sigma \\ \sigma & \sigma & A_\zeta \end{pmatrix} \begin{pmatrix} x_1 \\ \xi_2 \\ \zeta_3 \end{pmatrix} = \frac{1}{m} \begin{pmatrix} q_x E_x \\ q_\xi E_\xi \\ q_\zeta E_\zeta \end{pmatrix}. \tag{A.6.10}$$

Single Dipole

The single dipole is the most basic case; using the notation introduced above, it can be described by the equation

$$A_x x = \frac{q}{m} E_x, \tag{A.6.11}$$

leading to the solution

$$\chi = \frac{1}{A_x}. \tag{A.6.12}$$

Two Dipoles

Two dipoles coupled as shown in figure 2.11 can be described by the following equations (again in matrix form)

$$\begin{pmatrix} A_x & \sigma \\ \sigma & A_\xi \end{pmatrix} \begin{pmatrix} x_1 \\ \xi_2 \end{pmatrix} = \frac{1}{m} \begin{pmatrix} q_x E_x \\ q_\xi E_\xi \end{pmatrix}. \tag{A.6.13}$$

For simplicity, we omit the factor $\frac{q_i}{m}$ for the rest of this section. We obtain the solution

$$\begin{pmatrix} x_1 \\ \xi_2 \end{pmatrix} = \frac{1}{A_x A_\xi - \sigma^2} \begin{pmatrix} A_\xi E_x - \sigma E_\xi \\ A_x E_\xi - \sigma E_x \end{pmatrix}. \tag{A.6.14}$$

We examine the two cases $E_y = 0$ and $E_x = 0$. The definition of $\xi = (x/2, \sqrt{3}y/2)^T$ in (2.7.1) leads to $E_\xi = 1/2 E_x$ and $E_\xi = \sqrt{3}/2 E_y$, respectively. After introducing $a_2 = A_x A_\xi - \sigma^2$, we obtain

$$\begin{pmatrix} x_1 \\ \xi_2 \end{pmatrix} = \frac{1}{a_2} \begin{pmatrix} A_\xi - \frac{1}{2}\sigma \\ \frac{1}{2}A_x - \sigma \end{pmatrix} E_x, \tag{A.6.15}$$

$$\begin{pmatrix} x_1 \\ \xi_2 \end{pmatrix} = \frac{1}{a_2} \begin{pmatrix} -\frac{\sqrt{3}}{2}\sigma \\ \frac{\sqrt{3}}{2}A_x \end{pmatrix} E_y. \tag{A.6.16}$$

We substitute the vectors ξ and ζ and reintroduce q_x and q_ξ

$$\chi_{xx} = \frac{q_x^2}{a_2}\left[\left(A_\xi - \frac{\sigma}{2}\right) + \left(\frac{A_x}{4} - \frac{\sigma}{2}\right)\right] \tag{A.6.17}$$

$$= \frac{q_x^2}{a_2}\left(\frac{A_x}{4} + A_\xi - \sigma\right), \tag{A.6.18}$$

$$\chi_{xy} = \frac{q_x q_\xi}{a_2}\frac{\sqrt{3}}{2}\left(\frac{A_x}{2} - \sigma\right), \tag{A.6.19}$$

$$\chi_{yx} = \frac{q_x q_\xi}{a_2}\frac{\sqrt{3}}{2}\left(\frac{A_\xi}{2} - \sigma\right), \tag{A.6.20}$$

$$\chi_{yy} = \frac{q_\xi^2}{a_2}\frac{3}{4}A_x. \tag{A.6.21}$$

Assuming $A_x = A_\xi = A$ and $q_x = q_\xi = q$ leads to

$$\chi_{xx} = \frac{q^2}{A^2 - \sigma^2}\left(\frac{5}{4}A - \sigma\right), \tag{A.6.22}$$

$$\chi_{xy} = \chi_{yx} = \frac{q^2}{A^2 - \sigma^2}\frac{\sqrt{3}}{2}\left(\frac{A}{2} - \sigma\right), \tag{A.6.23}$$

$$\chi_{yy} = \frac{q^2}{A^2 - \sigma^2}\frac{3}{4}A. \tag{A.6.24}$$

We get the eigenvectors

$$\begin{pmatrix} -1 \\ 1 \end{pmatrix}, \begin{pmatrix} 1 \\ 1 \end{pmatrix}, \tag{A.6.25}$$

representing the cophasal and antiphasal modes of oscillation (see figure A.2). The associated eigenvalues are

$$\begin{pmatrix} A - \sigma \\ 0 \end{pmatrix}, \begin{pmatrix} 0 \\ A + \sigma \end{pmatrix}. \tag{A.6.26}$$

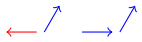

Figure A.2: The eigenmodes of two dipoles on a hexagonal grid. The arrows show the direction of carrier movement, while the color indicate the sign relative to the base vectors. Red stands for an oscillation, which is anti-parallel to the base vector.

Remembering that $A = \omega^2 - \omega_0^2 - i\gamma\omega$ and solving for ω yields the eigenfrequencies

$$\omega_{1/2} = \omega_{3/4} = \frac{i\gamma}{2} \pm \sqrt{-\frac{\gamma^2}{4} + \omega_0^2 + \sigma}, \tag{A.6.27}$$

$$\tag{A.6.28}$$

Three Dipoles

Three dipoles are described by the equations

$$\begin{pmatrix} A_x & \sigma & \sigma \\ \sigma & A_\xi & -\sigma \\ \sigma & -\sigma & A_\zeta \end{pmatrix} \begin{pmatrix} x_1 \\ \xi_2 \\ \zeta_3 \end{pmatrix} = \begin{pmatrix} E_x \\ E_\xi \\ E_\zeta \end{pmatrix}, \tag{A.6.29}$$

leading to the solution

$$\begin{pmatrix} x_1 \\ \xi_2 \\ \zeta_3 \end{pmatrix} = \frac{1}{a_3} \begin{pmatrix} \left(A_\xi A_\zeta - \sigma^2\right) E_x - \left(A_\zeta\sigma + \sigma^2\right) E_\xi - \left(A_\xi\sigma + \sigma^2\right) E_\zeta \\ -\left(A_\zeta\sigma + \sigma^2\right) E_x + \left(A_x A_\zeta - \sigma^2\right) E_\xi + \left(A_x\sigma + \sigma^2\right) E_\zeta \\ -\left(A_\xi\sigma + \sigma^2\right) E_x + \left(A_x\sigma + \sigma^2\right) E_\xi + \left(A_x A_\xi - \sigma^2\right) E_\zeta \end{pmatrix}, \tag{A.6.30}$$

with $a_3 = A_x A_\xi A_\zeta - A_x\sigma^2 - A_\xi\sigma^2 - A_\zeta\sigma^2 - 2\sigma^3$.

Assuming $A = A_x = A_\xi = A_\zeta$, the solution (A.6.30) simplifies to

$$\begin{pmatrix} x_1 \\ \xi_2 \\ \zeta_3 \end{pmatrix} = \frac{1}{a_3'} \begin{pmatrix} \left(A^2 - \sigma^2\right) E_x - \left(A\sigma + \sigma^2\right) E_\xi - \left(A\sigma + \sigma^2\right) E_\zeta \\ -\left(A\sigma + \sigma^2\right) E_x + \left(A^2 - \sigma^2\right) E_\xi + \left(A\sigma + \sigma^2\right) E_\zeta \\ -\left(A\sigma + \sigma^2\right) E_x + \left(A\sigma + \sigma^2\right) E_\xi + \left(A^2 - \sigma^2\right) E_\zeta \end{pmatrix}, \tag{A.6.31}$$

with $a_3' = A^3 - 3A\sigma^2 - 2\sigma^3$.

We substitute $E_\xi = \left(1/2 E_x, \sqrt{3}/2 E_y\right)^T$ and $E_\zeta = \left(1/2 E_x, -\sqrt{3}/2 E_y\right)^T$

$$\begin{pmatrix} x_1 \\ \xi_2 \\ \zeta_3 \end{pmatrix} = \frac{A^2 - A\sigma - 2\sigma^2}{A^3 - 3A\sigma^2 - 2\sigma^3} \begin{pmatrix} E_x \\ \frac{1}{2}E_x + \frac{\sqrt{3}}{2}E_y \\ \frac{1}{2}E_x - \frac{\sqrt{3}}{2}E_y \end{pmatrix}. \tag{A.6.32}$$

The final step is to substitute $\xi = \left(1/2 x, \sqrt{3}/2 y\right)^T$ and $\zeta = \left(1/2 x, -\sqrt{3}/2 y\right)^T$

$$x = \frac{3}{2}\frac{A^2 - A\sigma - 2\sigma^2}{A^3 - 3A\sigma^2 - 2\sigma^3} E_x, \tag{A.6.33}$$

$$y = \frac{3}{2}\frac{A^2 - A\sigma - 2\sigma^2}{A^3 - 3A\sigma^2 - 2\sigma^3} E_y. \tag{A.6.34}$$

Figure A.3: The eigenmodes of three hexagonal dipoles aligned in a star structure. The first one (left) has no resulting dipole moment. It can, therefore, not radiate in the far field. Such a mode is called "dark".

From the coupling matrix, we calculate the eigenvectors

$$\begin{pmatrix} -1 \\ 1 \\ 1 \end{pmatrix}, \begin{pmatrix} 1 \\ 1 \\ 0 \end{pmatrix}, \begin{pmatrix} 1 \\ 0 \\ 1 \end{pmatrix}, \tag{A.6.35}$$

eigenvalues

$$\begin{pmatrix} A-2\sigma \\ 0 \\ 0 \end{pmatrix}, \begin{pmatrix} 0 \\ A+\sigma \\ 0 \end{pmatrix}, \begin{pmatrix} 0 \\ 0 \\ A+\sigma \end{pmatrix}. \tag{A.6.36}$$

They represent three different modes of oscillation: from the center to the outside, from left to top right, from left to bottom right (see figure A.3).

Solving for ω yields the eigenfrequencies

$$\omega_{1/2} = \omega_{3/4} = \frac{i\gamma}{2} \pm \sqrt{-\frac{\gamma^2}{4} + \omega_0^2 + \sigma}, \tag{A.6.37}$$

$$\omega_{5/6} = \frac{i\gamma}{2} \pm \sqrt{-\frac{\gamma^2}{4} + \omega_0^2 - 2\sigma}, \tag{A.6.38}$$

where $\omega_{1/2}$ belongs to the first, $\omega_{3/4}$ to the second and $\omega_{5/6}$ to the third eigenmode.

Hexagonal Ring

We solve the equation

$$\begin{pmatrix} A_\xi & -\sigma & \sigma & 0 & 0 & 0 \\ -\sigma & A_\zeta & 0 & 0 & \sigma & 0 \\ \sigma & 0 & A_x & \sigma & 0 & 0 \\ 0 & 0 & \sigma & A_\zeta & 0 & -\sigma \\ 0 & \sigma & 0 & 0 & A_x & \sigma \\ 0 & 0 & 0 & -\sigma & \sigma & A_\xi \end{pmatrix} \begin{pmatrix} \xi_1 \\ \zeta_2 \\ x_3 \\ \zeta_4 \\ x_5 \\ \xi_6 \end{pmatrix} = \frac{1}{m} \begin{pmatrix} q_\xi E_\xi \\ q_\zeta E_\zeta \\ q_x E_x \\ q_\zeta E_\zeta \\ q_x E_x \\ q_\xi E_\xi \end{pmatrix}. \tag{A.6.39}$$

Again, we omit the factor $\frac{q_i}{m}$. With $a_6 = A_x A_\zeta A_\xi - A_\zeta\sigma^2 - 2\sigma^3 - A_x\sigma^2 - \sigma^2 A_\xi$, we obtain the solution

$$\begin{pmatrix}\xi_1\\ \zeta_2\\ x_3\\ \zeta_4\\ x_5\\ \xi_6\end{pmatrix} = \frac{1}{a_6}\begin{pmatrix} A_x\sigma E_\zeta + A_x A_\zeta E_\xi + \sigma^2 E_\zeta - \sigma^2 E_\xi - \sigma^2 E_x - A_\zeta\sigma E_x \\ A_x A_\xi E_\zeta + A_x\sigma E_\xi - A_\xi\sigma E_x - \sigma^2 E_x - \sigma^2 E_\zeta + \sigma^2 E_\xi \\ -\left(A_\xi\sigma E_\zeta + \sigma^2 E_\xi + \sigma^2 E_\zeta + A_\zeta\sigma E_\xi + A_\zeta A_\xi E_x + \sigma^2 E_x\right) \\ A_x A_\xi E_\zeta + A_x\sigma E_\xi - A_\xi\sigma E_x - \sigma^2 E_x - \sigma^2 E_\zeta + \sigma^2 E_\xi \\ -\left(A_\xi\sigma E_\zeta + \sigma^2 E_\xi + \sigma^2 E_\zeta + A_\zeta\sigma E_\xi - A_\zeta A_\xi E_x + \sigma^2 E_x\right) \\ A_x\sigma E_\zeta + A_x A_\zeta E_\xi + \sigma^2 E_\zeta - \sigma^2 E_\xi - \sigma^2 E_x - A_\zeta\sigma E_x \end{pmatrix}. \tag{A.6.40}$$

It is easy to see that $x_3 = x_5$, $\xi_1 = \xi_6$ and $\zeta_2 = \zeta_4$; we therefore write

$$\begin{pmatrix}x\\ \xi\\ \zeta\end{pmatrix} = \frac{2}{a_6}\begin{pmatrix} -\left[\left(A_\zeta A_\xi + \sigma^2\right)E_x + \left(A_\zeta\sigma + \sigma^2\right)E_\xi + \left(A_\xi\sigma + \sigma^2\right)E_\zeta\right] \\ -\left(A_\zeta\sigma + \sigma^2\right)E_x + \left(A_x A_\zeta - \sigma^2\right)E_\xi + \left(A_x\sigma + \sigma^2\right)E_\zeta \\ -\left(A_\xi\sigma + \sigma^2\right)E_x + \left(A_x\sigma + \sigma^2\right)E_\xi + \left(A_x A_\xi - \sigma^2\right)E_\zeta \end{pmatrix}. \tag{A.6.41}$$

We assume $A_x = A_\xi = A_\zeta = A$, and with a_6 simplified to $A^3 - 3A\sigma^2 - 2\sigma^3 = a_6'$, we obtain

$$\begin{pmatrix}x\\ \xi\\ \zeta\end{pmatrix} = \frac{2}{a_6'}\begin{pmatrix} -\left[\left(A^2 + \sigma^2\right)E_x + \left(A\sigma + \sigma^2\right)E_\xi + \left(A\sigma + \sigma^2\right)E_\zeta\right] \\ -\left(A\sigma + \sigma^2\right)E_x + \left(A^2 - \sigma^2\right)E_\xi + \left(A\sigma + \sigma^2\right)E_\zeta \\ -\left(A\sigma + \sigma^2\right)E_x + \left(A\sigma + \sigma^2\right)E_\xi + \left(A^2 - \sigma^2\right)E_\zeta \end{pmatrix}. \tag{A.6.42}$$

The next step is to substitute $E_\xi = \left({}^{E_x}/_2, {}^{\sqrt{3}E_y}/_2\right)^T$ and $E_\zeta = \left({}^{E_x}/_2, -{}^{\sqrt{3}E_y}/_2\right)^T$

$$\begin{pmatrix}x\\ \xi\\ \zeta\end{pmatrix} = \frac{2}{A^3 - 3A\sigma^2 - 2\sigma^3}\begin{pmatrix} \left(-A^2 - A\sigma - 2\sigma^2\right)E_x \\ \left(A^2 - A\sigma - 2\sigma^2\right)\left(\frac{1}{2}E_x + \frac{\sqrt{3}}{2}E_y\right) \\ \left(A^2 - A\sigma - 2\sigma^2\right)\left(\frac{1}{2}E_x - \frac{\sqrt{3}}{2}E_y\right) \end{pmatrix} \tag{A.6.43}$$

and to resubstitute $\xi = \left({}^1/_2 x, {}^{\sqrt{3}}/_2 y\right)^T$ and $\zeta = \left({}^1/_2 x, -{}^{\sqrt{3}}/_2 y\right)^T$

$$x = \frac{1}{A^3 - 3A\sigma^2 - 2\sigma^3}\left(-A^2 - 3A\sigma - \frac{5}{2}\sigma^2\right)E_x, \tag{A.6.44}$$

$$y = \frac{3}{A^3 - 3A\sigma^2 - 2\sigma^3}\left(A^2 - A\sigma - 2\sigma^2\right)E_y, \tag{A.6.45}$$

which leads to

$$\chi_{xx} = \frac{1}{A^3 - 3A\sigma^2 - 2\sigma^3}\left(-A^2 - 3A\sigma - \frac{5}{2}\sigma^2\right), \tag{A.6.46}$$

$$\chi_{xy} = \chi_{yx} = 0, \tag{A.6.47}$$

$$\chi_{yy} = \frac{3}{A^3 - 3A\sigma^2 - 2\sigma^3}\left(A^2 - A\sigma - 2\sigma^2\right). \tag{A.6.48}$$

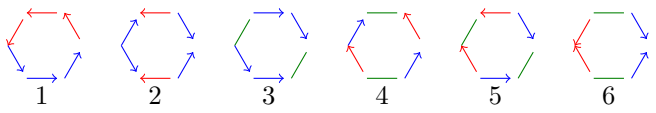

Figure A.4: The eigenmodes of the hexagonal ring. The first eigenmode has no electric dipole moment. The current flow, however, represents a magnetic mode. The second, fifth and sixth mode have no resulting dipole moment and are dark in the far field. The third and fourth mode are the only ones that possess an electrical dipole moment. They represent the same kind of carrier movement, an oscillation along the sides of the ring.

The eigenvectors are:

$$\begin{pmatrix} -1 \\ 1 \\ -1 \\ -1 \\ 1 \\ 1 \end{pmatrix}, \begin{pmatrix} 1 \\ 1 \\ -1 \\ 1 \\ -1 \\ 1 \end{pmatrix}, \begin{pmatrix} 0 \\ 1 \\ 1 \\ 1 \\ 1 \\ 0 \end{pmatrix}, \begin{pmatrix} 1 \\ -1 \\ 0 \\ -1 \\ 0 \\ 1 \end{pmatrix}, \begin{pmatrix} 0 \\ -1 \\ -1 \\ 1 \\ 1 \\ 0 \end{pmatrix}, \begin{pmatrix} -1 \\ -1 \\ 0 \\ 1 \\ 0 \\ 1 \end{pmatrix}. \tag{A.6.49}$$

It is more instructive to visualize them, instead of trying to describe their properties. This was done in figure A.4.

The eigenfunctions

$$\begin{pmatrix} A+2\sigma \\ 0 \\ 0 \\ 0 \\ 0 \\ 0 \end{pmatrix}, \begin{pmatrix} 0 \\ A-2\sigma \\ 0 \\ 0 \\ 0 \\ 0 \end{pmatrix}, \begin{pmatrix} 0 \\ 0 \\ A+\sigma \\ 0 \\ 0 \\ 0 \end{pmatrix}, \begin{pmatrix} 0 \\ 0 \\ 0 \\ A+\sigma \\ 0 \\ 0 \end{pmatrix}, \begin{pmatrix} 0 \\ 0 \\ 0 \\ 0 \\ A-\sigma \\ 0 \end{pmatrix}, \begin{pmatrix} 0 \\ 0 \\ 0 \\ 0 \\ 0 \\ A-\sigma \end{pmatrix}, \tag{A.6.50}$$

led to the eigenfrequencies

$$\omega_{1-4} = \frac{i\gamma}{2} \pm \sqrt{-\frac{\gamma^2}{4} + \omega_0^2 - \sigma}, \tag{A.6.51}$$

$$\omega_{5-8} = \frac{i\gamma}{2} \pm \sqrt{-\frac{\gamma^2}{4} + \omega_0^2 + \sigma}, \tag{A.6.52}$$

$$\omega_{9/10} = \frac{i\gamma}{2} \pm \sqrt{-\frac{\gamma^2}{4} + \omega_0^2 + 2\sigma}, \tag{A.6.53}$$

$$\omega_{11/12} = \frac{i\gamma}{2} \pm \sqrt{-\frac{\gamma^2}{4} + \omega_0^2 - 2\sigma}. \tag{A.6.54}$$

Appendix B

Selected Code Fragments

Some of the lines of code in this section are too long to fit on the page. These lines contain additional line breaks that are not part of the code and marked with ↵ (a carriage return symbol).

B.1 Calculating Transmission

Rectangular Grid Enumeration

This is the simplified MATLAB code that was used to calculate the transmission of an arbitrary grid placement. The original version also allowed the use of symbolic computation.

The output of `xyDipoleEquations`, stored in partX and partY, is the nearest neighbor coupling matrix, as explained in section 2.5.

The function `epsilonForGridPlacement` calculates ε_r of a given placement vector. The placement vector, containing m rows and n columns, has length $l = mn$. If a position in the $m \times n$ grid is occupied, the corresponding position in the placement vector contains a 1; otherwise, it contains a 0. We used a linear vector instead of a two-dimensional array so that we could use the placement vector as the genome of a genetic algorithm. We therefore had to apply some arithmetic conversions to access the nearest neighbors.

The function creates an $(m \times n) \times (m \times n) = l \times l$ coupling matrix. At every occupied position, the nearest neighbor coupling matrix (source) is copied into it (couplings). After copying all the couplings into the matrix, the rows and columns representing unoccupied edges are removed.

The simplified system of equations is then solved using the `\` operator (`MRDIVIDE`) and summed up.

```
function [partX partY] = xyDipoleEquations(cols, Cx, Cy, Csigma, Ctau_x, Ctau_y)
  %Generate the equations that describe the nearest neighbor coupling for
  % dipoles in x and y direction.
  % The resulting matrix is very similar to an adjacency matrix.
  %
  % PARAMETERS:
  % cols is the number of columns in the matrix. The row above the current one
  %  is at -2*cols.
  partX = zeros(cols,3*cols);
  partY = zeros(cols,4*cols);
  end;
  for row = 1:cols
    xcol = cols+row;
    ycol = 2*cols+row;
    partX(row, xcol) = Cx; %center
    partX(row, xcol-cols) = -Csigma; %-m; yDipole above left;
    partX(row, xcol+cols) = Csigma;  %+m; yDipole below left;
    partY(row, ycol) = Cy; %center
    %-2*m; yDipole above = 2 grid rows above
    partY(row, ycol-2*cols) = Ctau_y;
    %+2*m; yDipole below = 2 grid rows below
    partY(row, ycol+2*cols) = Ctau_y;
    partY(row, ycol-cols) = Csigma;  %-m; xDipole above right
    partY(row, ycol+cols) = -Csigma; %-m; xDipole below right
    if(row > 1) %exclude first col
      partX(row, xcol-1) = Ctau_x; %xDipole left
      %-m-1; xDipole above left
      partY(row, ycol-cols-1) = -Csigma;
      %+m-1; xDipole below left
      partY(row, ycol+cols-1) = Csigma;
    end;
    if(row<cols) %exclude last col
      partX(row, xcol+1) = Ctau_x; %xDipole right
      %-m+1 yDipole above right
      partX(row, xcol-cols+1) = Csigma;
      %+m+1 yDipole below right
      partX(row, xcol+cols+1) = -Csigma;
    end;
  end;
end
```

```
function eps = epsilonForGridPlacement(placement, cols, isXPolarized, freq)
  % Calculate epsilon from a placement vector.
  % cols is the number of columns
  % isXPolarized determines polarization (X=true, Y=false)
  % params contains the model variables:
  % [f0x gamma_x q_x f0y gamma_y q_y sigma thickness];

  rows = floor(length(placement)/cols);
  if cols*rows ~= length(placement)
    display('Parameters cols and rows do not match length of placement vector.');
    return;
  end;
  %initialize Variables
  couplings = zeros(cols*rows);
  eField = zeros(cols*rows,1);
  Ex = 0;
  Ey = 0;
  if isXPolarized == 1 %calculate chi_{xx}
    Ex = 1*params(3)^2;
  else %calculate chi_{yy}
    Ey = 1*params(6)^2;
  end;
  Ax = params(1)^2 - freq^2 -1i*params(2)*freq;
  Ay = params(4)^2 - freq^2 -1i*params(5)*freq;
  tau_x = -(0.75*params(1))^2;
  tau_y = -(0.75*params(4))^2;
  %%create coefficient matrix
  [partX partY] = xyDipoleEquations(cols, Ax, Ay, params(7), tau_x, tau_y);
  %outerColStartVal: position where in the outer Matrix m  the first entry
  % of the inner Matrix part[X|Y] should be stored,  i.e. the column offset
  % of the outer matrix to the inner matrix.
  outerColStartVal = 1;

  for row = 1:rows
    %check if X or Y Dipole
    if mod(row, 2) == 1 %odd, dipole in X direction
      sourceData = partX;
      outerColStartVal = outerColStartVal + 2*cols;
      eField((row-1)*cols+1:row*cols) = Ex;
    else %even, dipole in Y direction
      sourceData = partY;
      eField((row-1)*cols+1:row*cols) = Ey;
    end;
    [innerRows innerCols] = size(sourceData);
    innerColStartVal = 1;
    %special case for first two rows
    if row == 1 || row==2
      %row1 is a x row, remove sigma coupling to y row above
      & (-m and -m+1)
      %row2 is a y row, remove tau coupling to y row above (-2*m)
      innerColStartVal = cols+1;
      outerColStartVal = 0;
    elseif row == 3
      %the first time we only jump by cols instead of 2*cols
      outerColStartVal = cols;
    end;
    %special cases for last two rows
```

```
58      %second to last row is an y dipole
59      if row == rows-1 && mod(row, 2) == 0
60        %remove/skip coupling to missing y dipole below
61        innerCols = 3*cols;
62        if row == 1 || row == 2
63          %we alread start 1 col to the right --> add column
64          innerCols = 4*cols;
65        end;
66      end;
67      if row == rows %last row
68        if mod(row, 2) == 1 %odd, dipole in X direction
69          innerCols = 2*cols;
70        else %even, dipole in Y direction
71          innerCols = 3*cols;
72        end;
73      end;
74
75      %copy equations from source to couplings.
76      for innerRow = 1: innerRows
77        outerRow = (row-1)*cols+innerRow;
78        if placement(outerRow) == 0
79          eField(outerRow) = 0;
80          continue; %skip row if dipole is not present.
81        end;
82        for innerCol = innerColStartVal:innerCols
83          outerCol = outerColStartVal+innerCol-innerColStartVal+1;
84          if placement(outerCol) == 0 %skip couplings to empty rows
85            continue;
86          end;
87          couplings(outerRow, outerCol) = sourceData(innerRow, innerCol);
88        end;
89      end;
90    end;
91    %% remove empty rows/cols from Matrix
92    deletedRows = 0;
93    for row = 1:rows*cols
94      if placement(row) == 0
95        couplings(:,row-deletedRows) = [];
96        couplings(row-deletedRows,:) = [];
97        eField(row-deletedRows) = [];
98        deletedRows = deletedRows + 1;
99      end;
100   end;
101   eps = 1 + sum(couplings\eField); %epsilon = 1 + chi
102 end
```

Hexagonal Grid Enumeration

For the hexagonal grid, we followed a slightly different approach. Instead of copying a predefined nearest neighbor coupling matrix at the appropriate places, we set the coupling coefficients manually, using a small helper function.

The index arithmetic used to access the nearest neighbors is visualized in figure 2.14.

```
function coupling = setCoupling(coupling, placement, i, j, value)
  % Set the coupling between "i" and "j" to "value".
  %Check if i and j are valid indices and if there are dipoles at these positions.
  if i < 1 || j < i || i > length(placement) || j > length(placement) || placement(i) == 0 || placement(j) == 0
    return;
  end;
  coupling(i,j) = value;
  coupling(j,i) = value;
```

```
function eps = hexGridEpsilon(placement, unitCellsPerRow, fieldDirectionX, freq, params)
  %hexGridEpsilon(5) - calculate epsilon for dipoles placed on a hexagonal grid.
  %  Epsilon is the relative dieelectric permittivity.
  %  Parameters:
  %  placement - a vector of bits that signify which grid positions are occupied.
  %  unitCellsPerRow - the number of unit cells per row. One unit cell consists
  %   of three dipoles.
  %  fieldDirectionX - true if the field is in x direction, otherwise a field
  %   in y direction is assumed.
  %  freq - the current frequency
  %  params - all other parameters
  %  params = [f0x gamma_x q_x f0y gamma_y q_y sigma thickness];

  %define function setC to set the coupling coefficients
  setC = @(coupling, i,j,val) setCoupling(coupling, placement, i,j, val);
  Ax = params(1)^2 - freq^2 -1i*params(2)*freq;
  Ay = params(4)^2 - freq^2 -1i*params(5)*freq;
  tau = 0.75*params(1);

  len = length(placement);
  rowLength = unitCellsPerRow * 3;
  coupling = zeros(len,len);
  eField = zeros(len,1);

  E1 = 0;
  E2 = 0;
  E3 = 0;
  if fieldDirectionX == 1 %calculate eps_{xx}
    E1 = 1*params(3)^2;
    E2 = 0.5*params(3)^2;
    E3 = -0.5*params(3)^2;
  else %calculate eps_{yy}
    E1 = 0
    E2 = sqrt(3)/2*params(6)^2;
    E3 = sqrt(3)/2*params(6)^2;
  end;

```

```
38  rows = len / (3*unitCellsPerRow);
39  index = 1;
40  row = 1;
41  col = 0;
42  sigma = params(7);
43  for index=1:len-2
44    col=col+1;
45    if(col > unitCellsPerRow) col=1; end;
46
47    %first one is "flat" -
48    if placement(index) ~= 0
49      eField(index) = E1;
50      coupling(index, index) = Ax;
51      coupling = setC(coupling, index, index+1, sigma);%right /
52      coupling = setC(coupling, index, index+2, -sigma);%right \
53      if mod(col, 2) == 1 %"low"
54        coupling = setC(coupling, index, index-1, -sigma);%left \
55        coupling = setC(coupling, index, index-rowLength-2, sigma); %left /
56      else %"high"
57        coupling = setC(coupling, index, index-rowLength-1, -sigma); %left \
58        coupling = setC(coupling, index, index-2, sigma);%left /
59      end;
60    end;
61
62    index = index + 1; %%next one is "up" /
63    if placement(index) ~= 0
64      eField(index) = E2;
65      coupling(index, index) = Ay;
66      coupling = setC(coupling, index, index-1, sigma);%lower left _
67      coupling = setC(coupling, index, index+1, tau);%lower left \
68      if mod(col, 2) == 1 %"low"
69        coupling = setC(coupling, index, index+2, sigma);%upper right _
70      else %"high"
71        coupling = setC(coupling, index, index-rowLength+2, sigma);%upper right _
72      end;
73      coupling = setC(coupling, index, index-rowLength+1, tau); %upper right \
74    end;
75
76    index = index + 1; %%next one is "down" \
77    if placement(index) ~= 0
78      eField(index) = E3;
79      coupling(index, index) = Ay;
80      coupling = setC(coupling, index, index-2, sigma);%upper left _
81      coupling = setC(coupling, index, index+1, tau);%upper left /
82      if mod(col, 2) == 1 %"low"
83        coupling = setC(coupling, index, index+rowLength+1, sigma); %lower right _
84      else %"high"
85        coupling = setC(coupling, index, index+1, sigma); %lower right _
86      end;
87      coupling = setC(coupling, index, index+rowLength-1, tau); %lower right /
88    end;
89  end;
90  deletedItems = 0;
91  for index = 1:len
92    if placement(index) == 0
93      coupling(:,index-deletedItems) = [];
94      coupling(index-deletedItems,:) = [];
```

```
95        eField(index-deletedItems) = [];
96        deletedItems = deletedItems + 1;
97      end;
98    end;
99    eps = 1 + sum(coupling\eField);
100 end
```

B.2 Fit Calculation

The calculation of fits for different parameters was first implemented in MATLAB. This implementation was used to verify the first couple of measurements. The parameters of the model function were determined by minimizing the sum of squared differences between the calculated fit and the measured data. The minimization was done using the MATLAB function `fminsearch` that implements the Nelder-Mead simplex algorithm.

It soon became apparent that a more flexible solution would be useful. The fit functions were therefore reimplemented in Python. One of the advantages of this programming language are the powerful features for list manipulation. Since the fits are lists (vectors of data points) this proved useful and allowed for compact notation inside the code.

Following the principles of object oriented programming, the fit functions were defined inside a class hierarchy. The textbook architecture would use an abstract interface and one class for each fit function implementing it. Each fit class would be registered at a central body that would dispatch the requests to the fit functions. Since we only required a small set of fit functions, we omitted the central registry and opted for a simpler solution.

All fit functions inherit from `FitFunction`. This class provides the method `curValue` that calculates the fitValue for the given data point. The fit functions were collected in the two classes (`PetschulatModelFitFunction` and `HexagonalFitFunction`). The latter class inherits all methods of the former and is used as the source of the fits. The type of fit function that is used is determined by calling `setShape`.

```
class TransmissionFitFunction:
  def __init__(self):
    self.coeffs = {}

  def curValue(self, frequency):
    """the current value of the fit"""
    epsilon = self.calculateEpsilon(frequency)
    return self._transmissionFromEpsilon(epsilon, frequency)

  def setCoefficients(self, coefficients):
    """set the coefficients of the fit.
    coefficients is a dict. Valid Keys:
    thickness - thickness of the material - results in phase factor
    """
    if 'thickness' in coefficients:
      self.coeffs['thickness'] = coefficients['thickness']

  def calculateEpsilon(self, frequency):
    pass

  def _transmissionFromEpsilon(self, epsilon, frequency):
    """calculate the transmission of a material

    frequency - the frequency in Hertz (omega=2*pi*f)
    epsilon - scalar value of the electric permittivity
    assumes mu=1! If this assumption is not valid the
     formulas used probably need to be changed - in this case review them
    See Principles of Optics, $1.6.3, (54)-(56),(60); p.65-66

    This function is limited to a surface surrounded by air and an angle
     of incidence of 90 degrees.
    """
    p1 = cmath.sqrt(epsilon)
    beta = 2*math.pi*frequency*self.coeffs['thickness']*p1;
    t_1_2 = 2.0/(1.0+p1);
    t_2_3 = 2.0*p1/(p1+1.0);
    r_1_2 = (1.0-p1)/(1.0+p1);
    r_2_3 = (p1-1.0)/(p1+1.0);
    t = t_1_2*t_2_3*cmath.exp(1j*beta) / (1.0 + r_1_2*r_2_3*cmath.exp(2j*beta));
    return numpy.abs(t)
```

```
class PetschulatModelFitFunction(TransmissionFitFunction):
  """A Fit for a "petschulat like" model.

  see Petschulat et.al, Phys Rev B 82, 075102 (2010) - Simple and
   versatile analytical approach for planar metamaterials (5), (6)
  """
  AVAILABLE_SHAPES = ['C', 'S', 'L']
  AVAILABLE_POLARIZATIONS = ['X', 'Y']

  def setCoefficients(self, coefficients):
    """set the parameters of the fit.
    Only sets the parameters that are given in coefficients, others are not ↵
        changed

    Coefficients (keys):
    f0x - resonance frequency in x direction
    gamma_x - dampening in x direction
    q_x - charge in x direction
    f0y - resonance frequency in y direction
    gamma_y - dampening in y direction
    q_y - charge in y direction
    sigma - coupling strength between x and y direction
    amplitude - eta/(m*epsilon_0) - only affects total amplitude.
    e_vector - the direction of the e vector as a 3x1 vector
    measurement_direction - direction in which the measurement is done
    """

    TransmissionFitFunction.setCoefficients(self, coefficients) #parent
    for key, value in coefficients.iteritems():
      self.coeffs[key] = value
  #end of setCoefficients

  def calculateChiC(self, a_x, a_y, q_x, q_y, amplitude, sigma):
    #Petschulat et.al, (7)c
    chi = numpy.array([[0, 0, 0], [0, 0, 0], [0, 0, 0]], dtype=numpy.complex)
    chi[0, 0] = (q_x**2 *amplitude *2) /a_x;
    chi[1, 1] = (q_y**2 *amplitude *a_x) /(a_x*a_y- 2*sigma**2);
    return chi

  def calculateChiS(self, a_x, a_y, q_x, q_y, amplitude, sigma):
    #Petschulat et.al, (11)
    chi = numpy.array([[0, 0, 0], [0, 0, 0], [0, 0, 0]], dtype=numpy.complex)
    chi[0, 0] = (q_x**2 *amplitude) *(2*a_y/ (a_x*a_y-2*sigma**2))
    chi[1, 1] = (q_y**2 *amplitude) *(a_x/ (a_x*a_y-2*sigma**2))
    chi[0, 1] = (q_x*q_y*amplitude) *(2*sigma/ (a_x*a_y-2*sigma**2))
    chi[1, 0] = chi[0, 1]
    return chi

  def calculateChiL(self, a_x, a_y, q_x, q_y, amplitude, sigma):
    #Petschulat et.al, (14)
    chi = numpy.array([[0, 0, 0], [0, 0, 0], [0, 0, 0]], dtype=numpy.complex)
    chi[0, 0] = (q_x**2 *amplitude) *(a_y/ (a_x*a_y-sigma**2))
    chi[1, 1] = (q_y**2 *amplitude) *(a_x/ (a_x*a_y-sigma**2))
    chi[0, 1] = (q_x*q_y *amplitude) *(sigma/ (a_x*a_y-sigma**2))
    chi[1, 0] = chi[0, 1];
    return chi

```

```
57  def calculateEpsilon(self, frequency):
58    eye = numpy.array([[1,0,0],[0,1,0],[0,0,1]])
59    f0x = self.coeffs['f0x']
60    f0y = self.coeffs['f0y']
61    gamma_x = self.coeffs['gamma_x']
62    gamma_y = self.coeffs['gamma_y']
63    a_x = f0x*f0x-frequency*frequency-1j*frequency*gamma_x;
64    a_y = f0y*f0y-frequency*frequency-1j*frequency*gamma_y;
65
66    chi = self.calculateChi(a_x, a_y, self.coeffs['q_x'], self.coeffs['q_y'],
67        self.coeffs['amplitude'], self.coeffs['sigma'])
68    epsilon = eye + chi
69
70    direction_of_e_vector = self._normalize(self.coeffs['e_vector'])
71    direction_of_measurement = self._normalize(self.coeffs['measure_vector'])
72    eps = numpy.dot(numpy.dot(direction_of_measurement, epsilon), ↵
          direction_of_e_vector)
73    return eps
74
75  def setShape(self, shape):
76    if type(shape) == str:
77      shape = self.AVAILABLE_SHAPES.index(shape)
78
79    self.shape = shape
80    if self.AVAILABLE_SHAPES[shape] == 'C':
81      self.calculateChi = self.calculateChiC
82    elif self.AVAILABLE_SHAPES[shape] == 'S':
83      self.calculateChi = self.calculateChiS
84    elif self.AVAILABLE_SHAPES[shape] == 'L':
85      self.calculateChi = self.calculateChiL
86
87  def _normalize(self, vector):
88    norm = math.sqrt(sum([a*a for a in vector]))
89    return [a/norm for a in vector]
```

```
class HexagonalFitFunction(PetschulatModelFitFunction):
  AVAILABLE_SHAPES  = PetschulatModelFitFunction.AVAILABLE_SHAPES + ['Single Dipole', 'Hex Two arms', 'Hex Star', 'Hex Ring']
  def calculateChiSingleDipole(self, a_x, a_y, q_x, q_y, amplitude, sigma):
    b = (a_x**2-sigma**2)
    chi = numpy.array([[0, 0, 0], [0, 0, 0], [0, 0, 0]], dtype=numpy.complex)
    chi[0, 0] = (q_x**2 * amplitude)/a_x
    chi[1, 1] = (q_y**2 * amplitude)/a_y
    return chi
  def calculateChiTwoArms(self, a_x, a_y, q_x, q_y, amplitude, sigma):
    b = (a_x**2-sigma**2)
    chi = numpy.array([[0, 0, 0], [0, 0, 0], [0, 0, 0]], dtype=numpy.complex)
    chi[0, 0] = (q_x**2 *amplitude) *((1.25*a_x-sigma)/ b)
    chi[1, 1] = (q_x**2 *amplitude) *((numpy.sqrt(3)/2.0)*((a_x/2.0)-sigma)/ b)
    chi[0, 1] = (q_x**2 *amplitude) *(0.75*a_x/ b) #(q^2/b) * 3/4 * A
    chi[1, 0] = chi[0, 1]
    return chi

  def calculateChiStar(self, a_x, a_y, q_x, q_y, amplitude, sigma):
    chi = numpy.array([[0, 0, 0], [0, 0, 0], [0, 0, 0]], dtype=numpy.complex)
    chi[0, 0] = 3.0*amplitude*(1.0*q_x**2*(0.5*a_x+sigma)) / (a_x**2 + a_x*sigma-2.0*sigma**2)
    chi[1, 1] = chi[0, 0]
    return chi

  def calculateChiHexRing(self, a_x, a_y, q_x, q_y, amplitude, sigma):
    chi = numpy.array([[0, 0, 0], [0, 0, 0], [0, 0, 0]], dtype=numpy.complex)
    chi[0, 0] = (3.0*q_x**2*(a_x-2.0*sigma)) / (a_x**2-a_x*sigma-2.0*sigma**2)
    chi[1, 1] = chi[0, 0]
    return chi

  def setShape(self, shape):
    #[...]
    if self.AVAILABLE_SHAPES[shape] == 'Single Dipole':
      self.calculateChi = self.calculateChiSingleDipole
    elif self.AVAILABLE_SHAPES[shape] == 'Hex Two arms':
      self.calculateChi = self.calculateChiTwoArms
    #[...]
    else:
      PetschulatModelFitFunction.setShape(self, shape)
  #end setShape
```

Appendix C

Further Measurements

C.1 Measured Data

Most structures were measured several times. Since those measurements provided very similar data, only selected examples were included in the main part of this thesis. In this section, we present a selected number of additional plots

Comparing measurements of the same structure done on different days, we get an idea about their reproducibility (see figure C.1). While peak positions did not change between measurements the depth and width of peaks did change significantly. We identified several reasons for this:

- Differences in the output power of the primary laser
- Changes in the alignment of our setup (due to temperature fluctuations and sample mounting)
- Variations in the humidity in the terahertz path (depending on the flow rate and duration of the purge and fluctuations in the water content of our dry air supply).

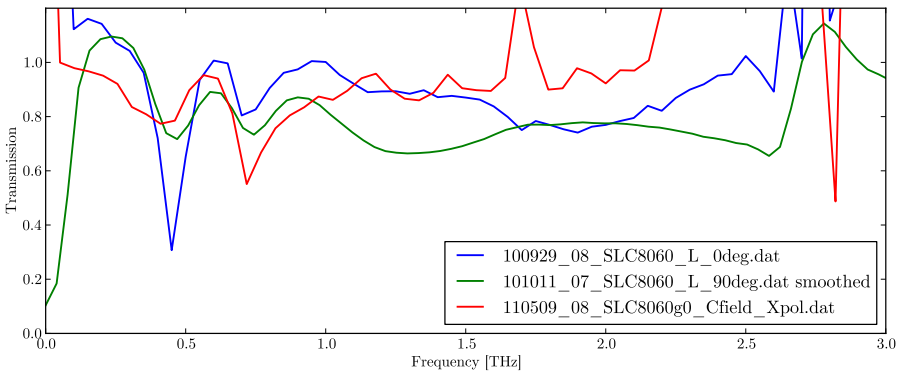

Figure C.1: Measurements of the same structures (8060 L, X Polarization) on three different days. While the depth of the resonances varies, the position shows almost no change.

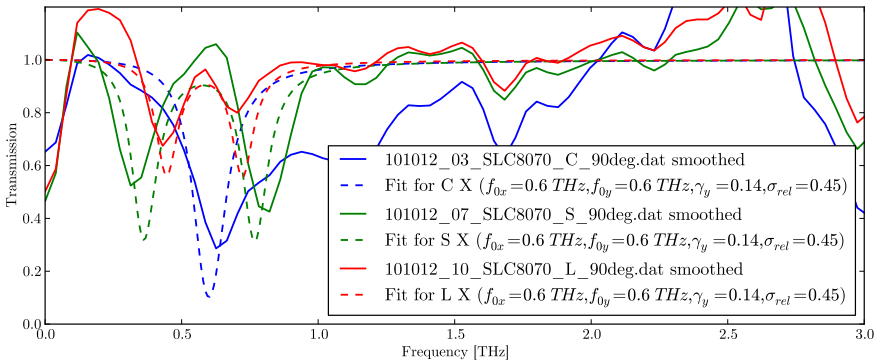

(a) $f_{0x} = 0.60$ THz, $\sigma = 0.45$

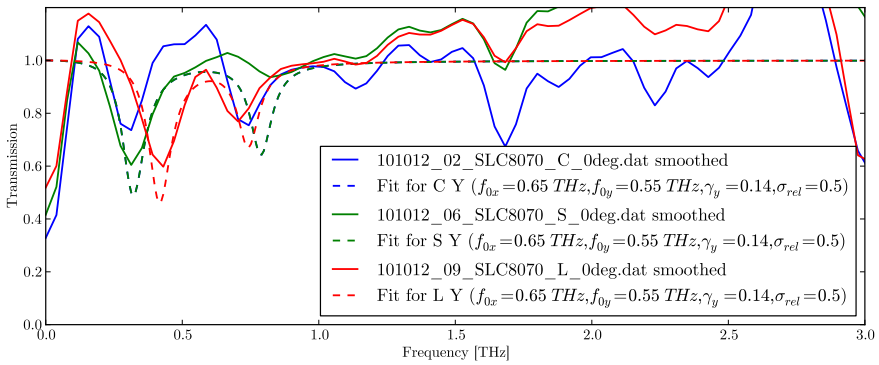

(b) $f_{0x} = 0.65$ THz, $\sigma = 0.5$

Figure C.2: Comparison of fits for two different x resonance frequencies (f_{0x}) for SLC8070 in X polarization. The higher frequency yields a slightly better fit, although the difference is less clear than that between figures 3.7a and 3.7b.

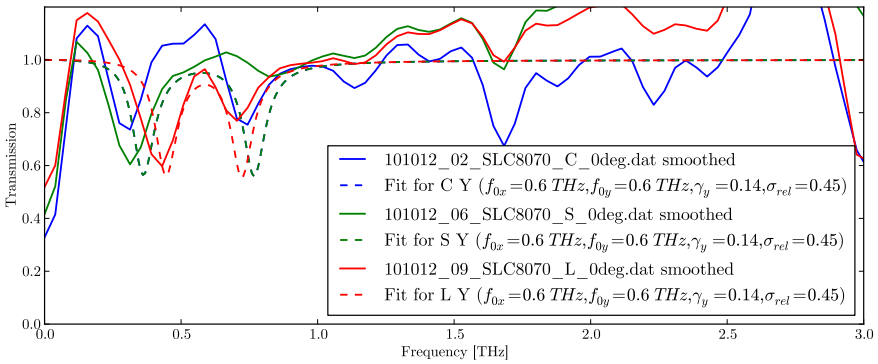

(a) $f_{0x} = 0.60$ THz, $\sigma = 0.45$

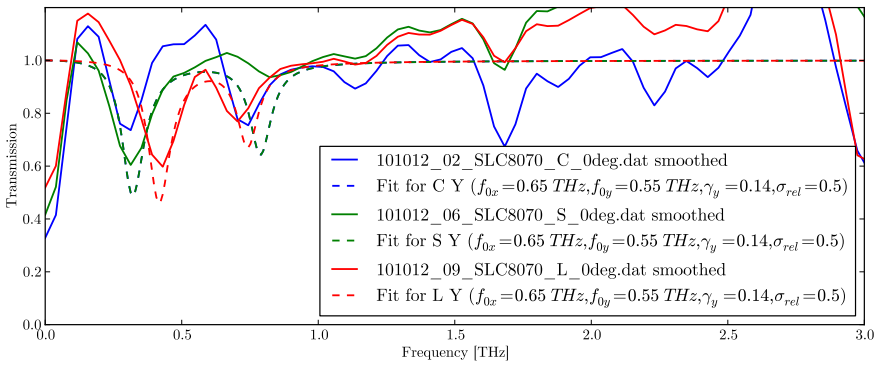

(b) $f_{0x} = 0.65$ THz, $\sigma = 0.5$

Figure C.3: Comparison of fits for two different x resonance frequencies (f_{0x}) for SLC8070 in Y polarization. The higher frequency yields a slightly better fit, although the difference is less clear than that between figures 3.8a and 3.8b.

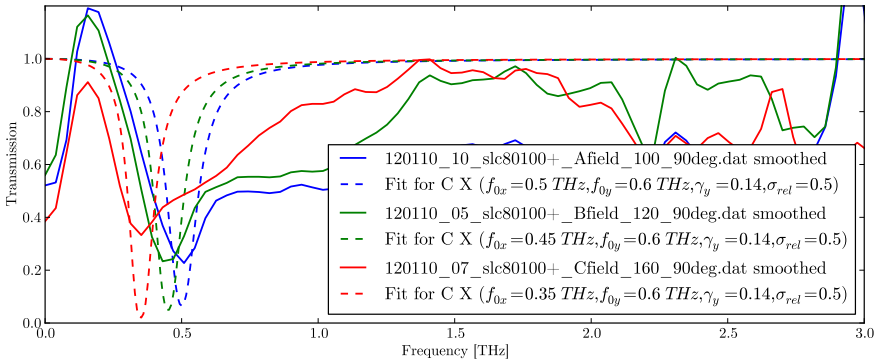

(a) X Polarization

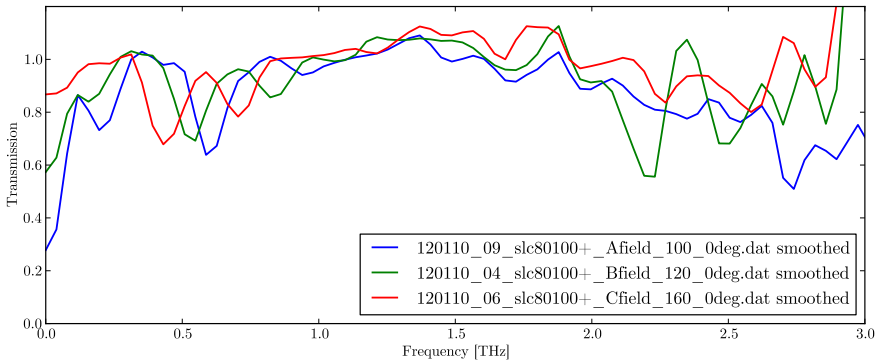

(b) Y polarization

Figure C.4: SLC80100+ C structures with lengths of 100 µm, 120 µm and 160 µm.

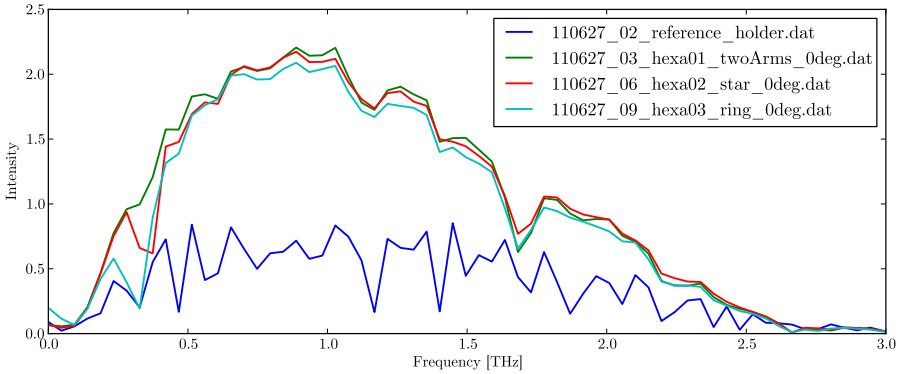

Figure C.5: Hexagonal structures. The transmission data of the reference is lower than that of the structures, indicating a problem during the measurement. We would usually retry this measurement, but the experimental setup is unavailable for the foreseeable future.

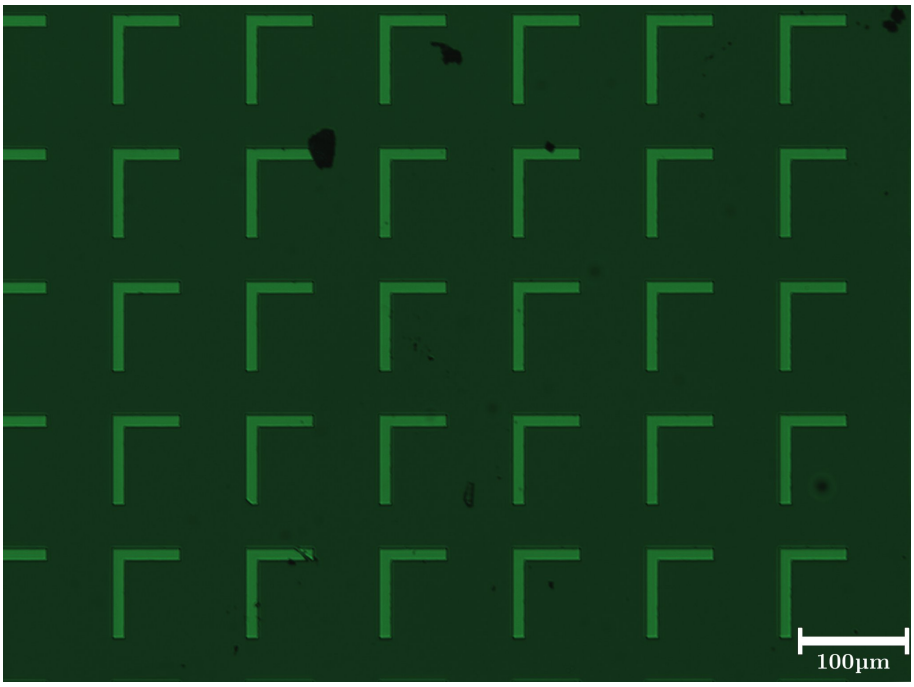

Figure C.6: CSL6080, L structure.

C.2 Images

In addition to the C structure shown in figure 3.2 we present microscope images of the other two structures (L and S). Note that the size of each structure is different. In order to provide an idea of their scale, we included a picture of one sample (SLC8080).

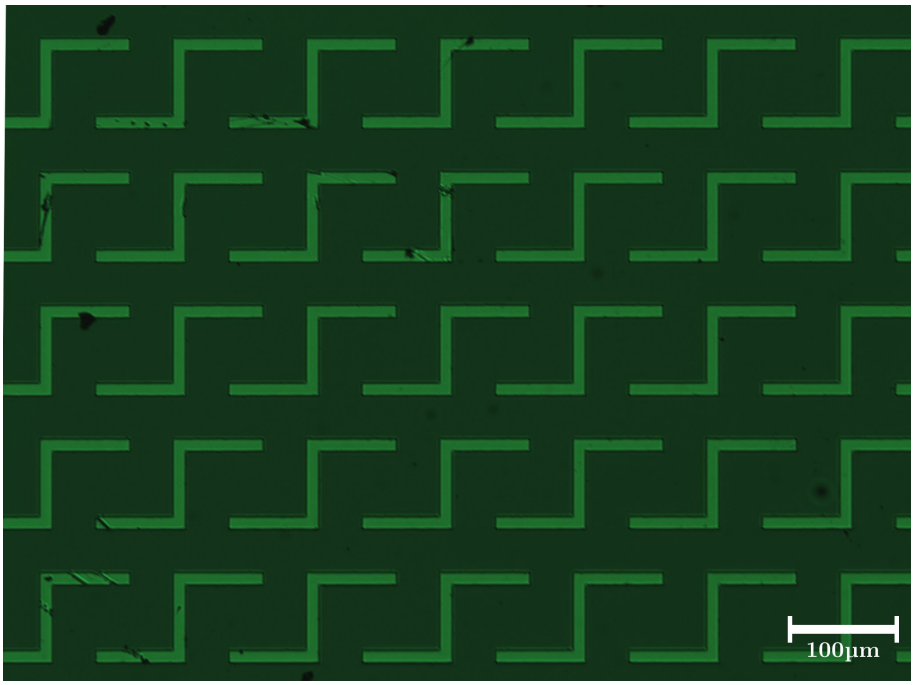

Figure C.7: CSL8080, S structure.

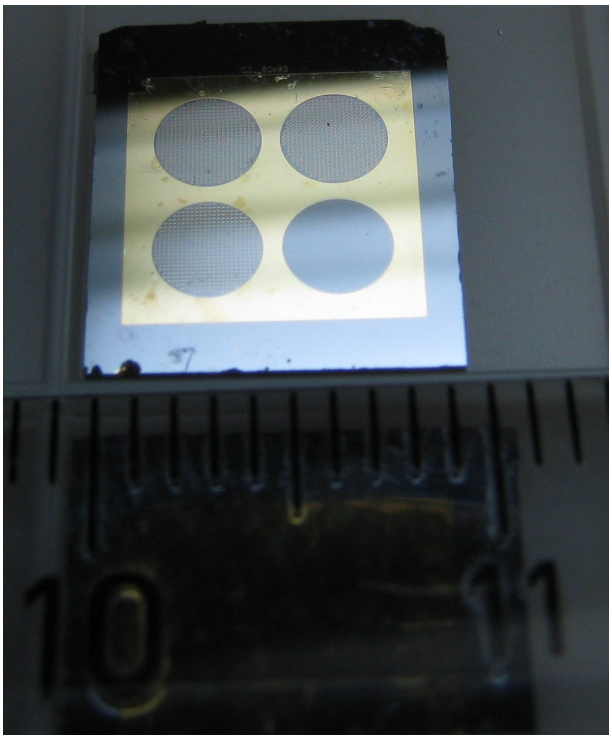

(a) Sample

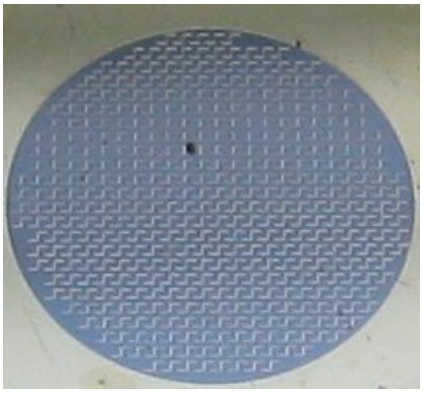

(b) Detail

Figure C.8: Sample CSL8080. All samples consist of four fields. Here, they contain C (top left), S (top right) and L (bottom left) structures as well as an empty reference field (bottom right) inside a patch of gold on a gallium arsenide substrate. The detail (below) shows the top right field, which contains S structures. The same structures are also shown in the microscope image in figure C.7.

Actum est, comites!